Inferring subglacial hydrology from investigations of supraglacial lake drainages and meltwater plumes at Store Glacier, West Greenland

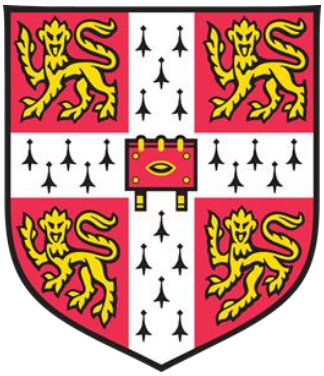

Isabel Hagen

Scott Polar Research Institute

University of Cambridge

This dissertation is submitted for the degree of

Master of Philosophy

July 2020

Abstract

The Greenland ice sheet has experienced a six-fold increase in ice loss during the last three decades, contributing significantly to global sea level rise. About 60% of the Greenland ice loss comes from dynamic ice loss from tidewater glaciers. Tidewater glaciers each have unique subglacial drainage systems and discharge meltwater into adjacent fjords differently. However, studies of the subglacial hydrology of individual tidewater glaciers have been limited, largely due to the difficulty in obtaining direct measurements. The input of water to the subglacial drainage systems come from drainage of supraglacial lakes, crevasses and moulins. The water travel downstream through subglacial channels, eventually reaching the terminus of the glacier, where the freshwater discharge form buoyant plumes that rise through the ambient ocean water, and eventually reach the surface. In this study, supraglacial lake volume and drainage were analysed with the dual-satellite FASTER algorithm, and meltwater plume areas were assessed through time-lapse photogrammetry in the Python toolbox PyTrx, in order to reconstruct the subglacial hydrology of the tidewater glacier Store Glacier in West Greenland during the 2018 summer melting season. The results of this study indicate a distributed and inefficient drainage system in June, with drainage leading to increased subglacial storage in cavities and disconnected channels. By early July, the drainage system on the glacier below 1000 m elevation had developed into an efficient system, experiencing fast hydraulic transmissivity, while elevations above 1000 m still experienced slow hydraulic transmissivity in a distributed drainage system. This research provides high-detail observations of the unique subglacial drainage system of a tidewater glacier. Understanding the subglacial hydrology of tidewater glaciers is key for making ice loss predictions about the next century.

Declaration

I declare that this dissertation is the result of my own work, except where specifically indicated in the Acknowledgements and text.

The length of this study does not exceed 20,000 words in length, excluding this Declaration, Acknowledgements, captions, figures, tables, References and Appendices.

Isabel Hagen

July 2020

Acknowledgements

I am beyond words grateful to my supervisor Dr. Poul Christoffersen at the Scott Polar Research institute (SPRI). He managed to supervise me remotely through the pandemic and throughout this year he has provided me with constant encouragement, confidence and critical insights.

I am also grateful to Dr. Tom Chudley (SPRI), for being able to pop over to his desk at SPRI for questions and, following the covid-19 outbreak and my relocation to Stockholm, Sweden; providing invaluable guidance on remote sensing in Google Earth Engine via e-mail.

A big thank you also to Dr. Penelope How at Edinburgh University, for allowing me to work with her excellent Python toolbox PyTrx and for all her help and support with my time-lapse data.

I would also like to thank Dr. Antonio Abellan at University of Leeds, for letting me work with his time-lapse images collected from cameras he installed at Store Glacier in 2017 with support from a Maria Skłowowska Curie Fellowship (grant no. 705215) and the RESPONDER project supported by the European Research Council under the European Union's Horizon 2020 research and innovation program (Grant 683043). I am also grateful to Dr. Sam Doyle at Aberystwyth University, for providing me with meteorological data, and Dr. Marion Bougamont, for her flow routing model of the Store Glacier subglacial discharge.

A huge thank you to my friends and fellow MPhils at SPRI, with a special thanks to Nick Homer and Joe Everest for constantly cheering me on.

Lastly, thank you to my family and friends for your endless support and for forcing me to take breaks once in a while. I could not have done this without you.

Table of Contents

List of Figures

List of Tables

1. Introduction

1.1 Justification for the Study

The Greenland ice sheet has experienced a six-fold increase in ice loss during the last three decades (Fettweis et al., 2017; Khan et al., 2015; Rignot et al., 2011), from 51 ± 17 Gt per year in 1980–1990 to 286 ± 20 Gt per year in 2010–2018 (Mouginot et al., 2019). The mass balance change is due to increased ablation through surface melt and runoff while snow accumulation has stayed rather constant, together with increased ice discharge. Ice is discharged through calving of tidewater glaciers in dynamic response to atmospheric and oceanic forcing (Mouginot et al., 2019; Rignot & Kanagaratnam, 2006; van den Broeke et al., 2016). Dynamic ice loss accounts for >60% of total ice loss (Mouginot et al., 2019).

During the summer melting season, supraglacial lakes and crevasses form on the Greenland ice sheet. The lakes eventually drain and the water percolates down to the glacier base, where it is connected to the subglacial drainage system. The subglacial drainage system of tidewater glaciers discharge meltwater into adjacent fjords. The freshwater form buoyant plumes which entrains ambient fjord water as they rise to the surface. Studies have shown that meltwater plumes promote calving by undercutting, through increased submarine melting and fjord circulation (Carroll et al., 2015; Cowton et al., 2015; Fried et al., 2015; Jackson et al., 2017, Jouvet et al., 2018; Slater et al., 2018).

Few studies have used observations of plumes as indicators of tidewater glaciers subglacial hydrology, a key uncertainty in predictions of sea level rise (Nienow et al., 2017). The subglacial hydrology of tidewater glaciers is part of complex processes such as fjord circulation, calving and submarine melting. However, most of the observations and modelling of subglacial hydrology have been done on land-terminating glaciers (Chandler et al., 2013; Flowers, 2015). Until recently, observations of the subglacial hydrology of tidewater glaciers have been limited (e.g. Howat et al., 2010; Joughin et al., 2008; Moon et al., 2014) due to the difficulty in obtaining direct measurements.

This study will use dual-satellite imagery and time-lapse imagery to observe supraglacial lake volumes and drainage, and the appearance and area of meltwater plumes connected to a West Greenland tidewater glacier, in order to infer the glacier's subglacial hydrology.

1.2 Aims and Objectives

The overarching aim of this thesis is to test the hypothesis that the nature of subglacial hydrological systems operating at tidewater glaciers can be inferred from quantitative assessments of supraglacial lake drainages and meltwater plumes forming at the calving termini.

The main objectives of this dissertation are:

(i) Quantify supraglacial lake volumes in order to establish a record of volume losses and discharge at Store Glacier during the melting season 2018.

(ii) Quantify the surface areas of plumes forming from subglacial discharge at the terminus of Store Glacier during the melting season 2018.

(iii) Combine (i) and (ii) in order to identify shared characteristics and infer the subglacial hydrological transmissivity of lakes forming at different elevation bands and increasing ice thickness and distance from the front.

1.3 Background

1.3.1 Subglacial drainage systems

Meltwater produced at glaciers and ice sheets is transported downstream either through runoff or through subglacial drainage systems. The subglacial drainage systems of glaciers and ice sheets are classified as either efficient, characterized by channelized systems, or inefficient, characterized by distributed systems, typically consistent of a network of basal cavities (Flowers, 2015). See figure 1 for the different elements of subglacial drainage systems. The evolution of subglacial drainage system efficiency is dynamic, on both short- and long-term timescales. Water is distributed to the supraglacial drainage systems during the summer melting season, through drainage of supraglacial lakes and crevasses and through moulins. Variations in the rate of meltwater input creates dynamic responses at the ice-bed, such as ice uplift and increased basal sliding (Doyle et al., 2013: Dow et al., 2015; Sugiyama et al., 2008), and modifying the efficiency of the system throughout the season (Bartholomew et al., 2010; Moon et al., 2014; Sundal et al., 2011).

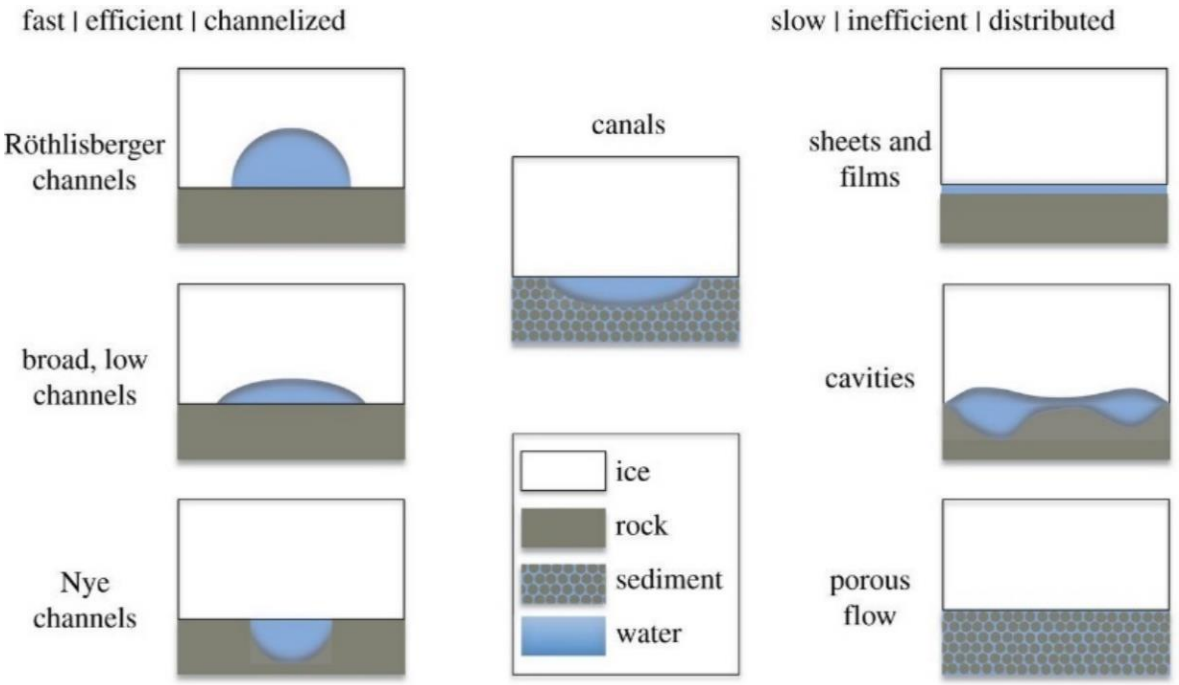

Figure 1. Elements of subglacial drainage systems, divided into efficient drainage and inefficient drainage, and canals, which can be classified as inefficient or efficient, depending on opening and closing processes. Figure from Flowers (2015).

The subglacial drainage system typically appears different at certain elevations of the ice sheet. At low elevations there are sufficient hydrological gradients needed for viscous heat dissipation, and efficient subglacial channels can form (Dow et al., 2015). Efficient drainage systems develop seasonally at elevations below 1000 m, and up to 40 km inland from the ice sheet margin (Chandler et al., 2013: Doyle et al., 2014; Tedstone et al., 2015). At high elevations the thick ice promotes subglacial channel closure by creep and the water entering the system typically reach distributed and inefficient linked cavities. When water drained from supraglacial lakes reach the cavities they expand, inducing high basal pressure and faster basal sliding (Dow et al., 2015; Meierbachtol et al., 2013). Water from supraglacial lakes can also modify the seasonal efficiency of the subglacial system (Andrews et al., 2018; Hoffman et al., 2011; Sundal et al., 2011) and open new surface-to-bed connections, increasing meltwater input to the system throughout the season (Catania & Neumann, 2010; Hoffman et al., 2018).

Tidewater glaciers discharge subglacial drainage into adjacent fjords (see figure 2). Each tidewater glacier has a unique subglacial drainage system and discharge meltwater to the fjord differently. Subglacial discharge experience strong seasonal variations due to variations in the drainage system, with peak discharge during the summer melting season (Matthews and Quinlan 1975; Motyka et al. 2003; Svendsen et al. 2002).

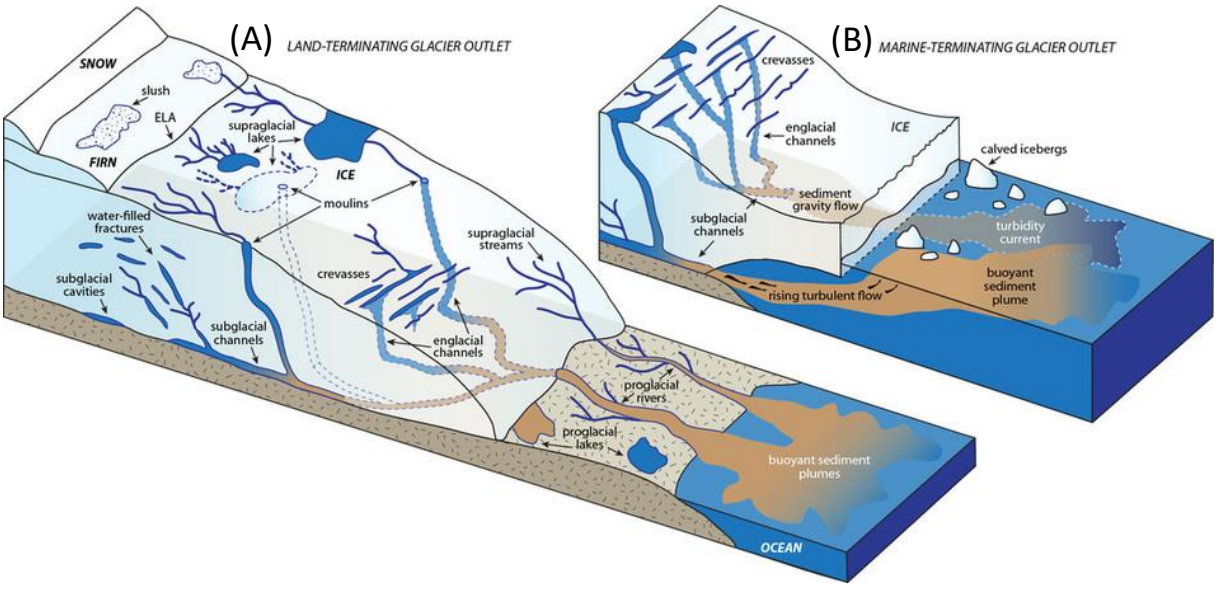

Figure 2. Elements of the Greenland ice sheet hydrologic system for (A) land-terminating glacier outlets and (B) marine-terminating glacier outlets. Figure from Cuffey & Paterson (2011), modified by Chu (2013).

Chu et al. (2009) completed a satellite observation of a 66,000 m^2 ice-sheet drainage basin and the appearance of sediment plumes in the adjacent Kangerlussuaq Fjord. The authors confirmed that the origin of the sediment plumes was meltwater from the ice sheet. Moreover, the authors determined that plumes appeared almost directly after the onset of surface melting, and concluded rapid coupling between the ice sheet and subglacial discharge. Analysis of plumes following supraglacial lake drainage events were less straight forward, with only 38% of lake drainage events triggering an increase in plume area (Chu et al., 2009).

Direct studies of the drainage system of Store Glacier in West Greenland were made by Doyle et al. (2018) who completed a borehole drilling along the central flow line to the base of outlet glacier Store Glacier, finding a high basal water pressure of >90% of the overburden ice pressure 30 km inland from the front, indicating a largely inefficient basal water system there. This was supported by a study by Young et al. (2019), who completed velocity measurements every 1 km along the central flow line of the same glacier in 2014-2015, and found surface velocities 30 km inland of the glacier to gradually increase throughout the melting season, indicating a relatively stable inefficient drainage system, while the lower part of the glacier, with surface elevations <1000 m, experienced seasonal variations in ice flow consistent with the development of efficient basal drainage in late summer. The study also concluded that channelized subglacial drainage systems developed closer to the front. These findings were supported by Cook et al. (2020) who modelled the subglacial hydrological system and found

an active subglacial drainage system with significant channelization up to 55 km inland from the terminus in summer, and an activated distributed sheet extending another 10 km inland.

1.3.2 Supraglacial lakes

During the summer melting season in Greenland, surface meltwater form supraglacial lakes and crevasses at the ice sheet surface (van den Broeke et al., 2016). Eventually the water drains down to the bed of the glacier. The drained freshwater becomes part of the subglacial drainage system, leading the water downstream, eventually reaching the front of the glacier (Bartholomaus et al., 2007; Bartholomew et al., 2010; Zwally et al., 2002). The lakes can drain slowly, over days to weeks, or rapidly, over hours to days (Hoffman et al., 2011; Joughin et al., 2013; Nienow et al., 2017). Rapidly draining lakes have been observed to stand for 28 to 45% of all supraglacial lakes in West Greenland (Cooley & Christoffersen, 2017; Fitzpatrick et al., 2014), and occur through hydraulic fracture.

Studies have shown that for a lake to drain rapidly, there needs to be a sufficient volume of water to drive a fracture to the bed (Stevens et al., 2015). The required lake volume for drainage is individual for each lake, dependent on ice thickness, ice temperature and fracture geometry. Lake volume is however not the primary driver of rapid drainage. Stevens et al. (2015) determined that rapid lake drainage is dependent on the presence of pre-existing fractures, basal motion, and the local stress-strain regime. Rapidly draining lakes are on average larger than slow draining lakes, and greater water volumes makes a lake more likely to force a fracture all the way to the bed, once the local stress regime forces initial fracture formation. No temporal or spatial differences have been noted between the formation of rapidly draining lakes and slowly draining lakes (Cooley & Christoffersen, 2017; Stevens et al., 2015).

Chudley et al. (2019) completed a field study of a supraglacial lake at Store Glacier in 2018. The authors found that high background tensile stresses were enough for surface-to-bed fractures. Based on the results, the authors suggested that lakes that are located in certain stress regimes can act as “trigger lakes”, where an intersection of the lake with an existing moulin can lead to rapid drainage. While other lakes, “response lakes”, require a precursory event in order to drain. Moreover, Christoffersen et al. (2018) found that drainage increase tensile stress in the proximity to other lakes, causing more hydrofractures and subsequently more lakes to drain through moulins. Moulins deliver most of the surface meltwater to the ice-sheet bed (Koziol., 2017), and have been observed to cause monthly to seasonal increase in ice velocity

(Bartholomew et al., 2010; Joughin et al., 2017; Koziol & Arnold, 2018; Zwally et al., 2002). See figure 3 for photographs of aspects of supraglacial lake drainage and moulins. Rapid lake drainage can also cause lower subglacial effective pressure and enhanced basal sliding over hours to days (Andrews et al., 2014; Banwell et al., 2016; Bartholomew et al., 2011), affecting the negative mass balance of the Greenland ice sheet. Moreover, meltwater reaching the subfreezing ice in the glacier can possibly affect the ice deformation rate (Lüthi et al., 2015; Phillips et al., 2010; Poinar et al., 2017). If water from a slowly draining lake overflow a stream to the bed it can cause basal uplift or sliding and thereby increase the tendency of rapid lake drainage in the vicinity (Stevens et al., 2015; Tedesco et al., 2013).

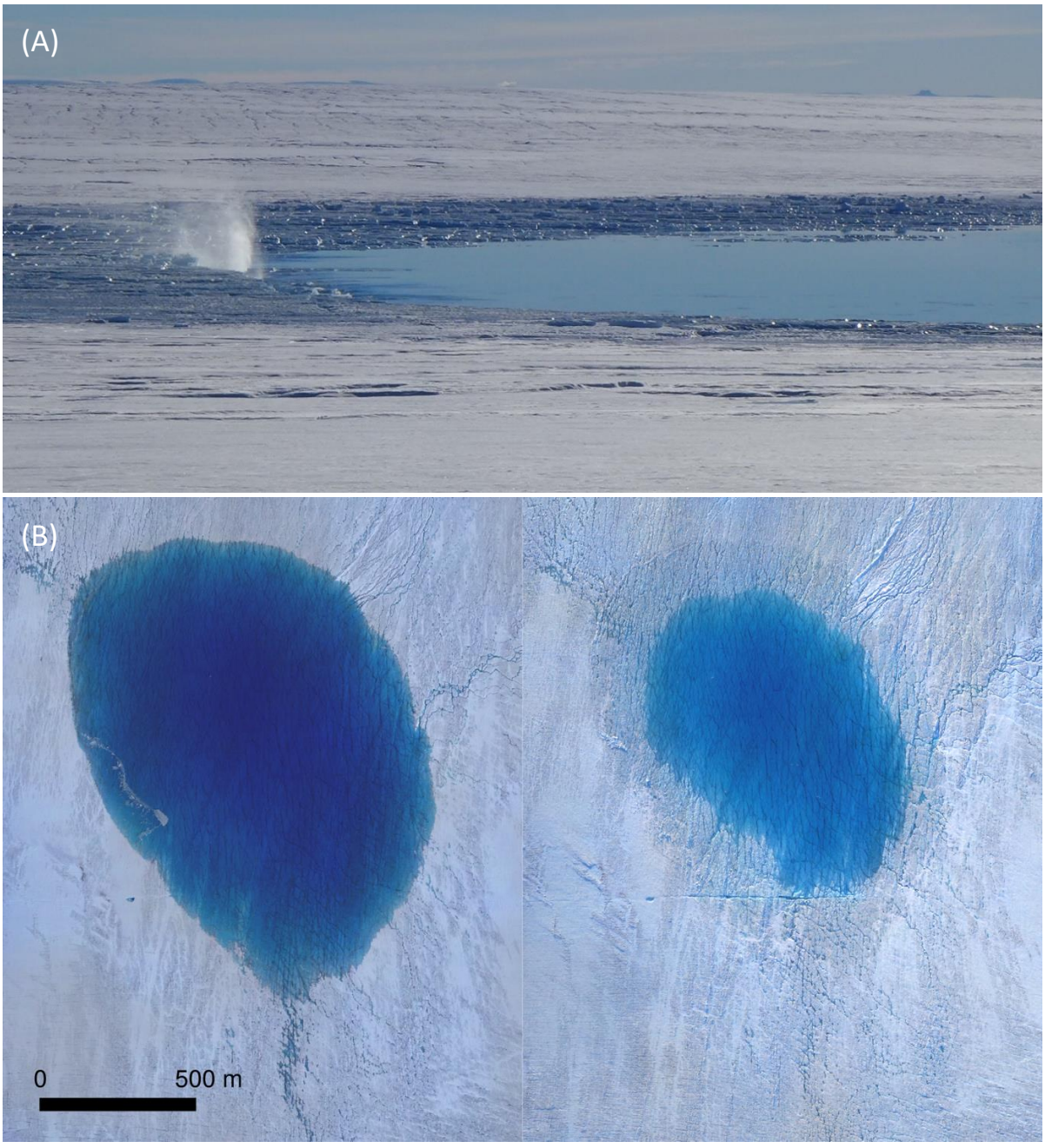


(C)

Figure 3. Photographs of aspects of supraglacial lake drainage and moulins. **(A)** Photograph of lake 42 draining on 7 July 2018 after a large fracture intersected the lake. Photograph from Poul Christoffersen. **(B)** Unmanned Aerial Vehicle (UAV, or "drone") imagery captured the drainage of lake 42 on 7 July in unprecedented detail. The image on the left was taken at ~13.00: five hours later, the lake started to drain, and by 02:00 (right), it had lost 5 million m^3 of water, or two-thirds of its volume. Imagery from Thomas Chudley. **(C)** Photograph of the fracture one day after lake 42 drained in 2018. Photograph from Poul Christoffersen. **(D)** Photograph of surface meltwater draining into a moulin on Store Glacier, West Greenland. Photograph from Robbie Shone (Amos, 2019).

There are clear short-term effects on ice dynamics from lake drainage. However, the long-term (seasonal to decadal) impacts on ice dynamics are still unclear (Nienow et al., 2017). This is due to the fact that the subglacial drainage system is dynamic in itself, meaning it can evolve to higher hydraulic efficiency, or water can pour into cavities or disconnected regions at the bed and cause slowdown in ice velocity during late summer or winter season (Bartholomew et al., 2010; de Fleurian et al., 2016; Hoffman et al., 2011; Sole et al., 2013). Ice velocity slowdown are first and foremost observed at the ice-marginal regions (e.g. Young et al., 2019). In the interior regions of the ice sheet, observations suggest that the increase in ice velocities during summer is impacted by the decrease in ice velocity later in the season (de Fleurian et al., 2016; Doyle et al., 2014). The uncertainties of long-term impacts on ice dynamics by lake drainage contribute to uncertainties in predicting future ice loss from the Greenland ice sheet. It is therefore of utmost importance to study the seasonal filling and drainage of lakes and gain a

deeper understanding of spatial distributions, as well as inter-annual variations, to in turn conclude on the lakes impact on subglacial drainage systems and ice dynamics (Arnold et al., 2014; Banwell et al., 2016; Koziol et al., 2017).

Supraglacial lake drainage has been observed with remote sensing techniques (e.g. Nienow et al., 2017). Lake evolution has been studied with the Landsat and ASTER satellites (Arnold et al., 2014; Banwell et al., 2014; Chen et al., 2017; Georgiou et al., 2009; Gledhill and Williamson, 2018; Legleiter et al., 2014; Macdonald et al., 2018; McMillan et al., 2007; Miles et al., 2017; Moussavi et al., 2016; Pope et al., 2016; Sneed and Hamilton, 2007). The spatial and temporal resolution of these studies are 15-30 m and ≥4 days, respectively. However, field-based studies of rapid lake drainage have found that draining caused by hydrofracture occur in less than a day (Das et al., 2008; Doyle et al., 2013; Krawczynski et al., 2009; Tedesco et al., 2013). Therefore, there is a clear need of higher temporal resolution. Alternative studies with sub-daily resolution have been made using MODIS imagery (Box & Ski., 2007; Fitzpatrick et al., 2014; Liang et al., 2012; Sundal et al., 2009; Williamson et al., 2017), at the expense of high spatial resolution (250-500m). Lakes smaller than 0.125 m^2 are therefore not included in these studies. To overcome the issues of spatial and temporal resolution, recent studies of supraglacial lakes have used dual-satellite imagery (Miles et al., 2017). Williamson et al. (2018a) used Sentinel-2A level 1C with a 10-meter spatial resolution and a 5-day revisit time at the Equator (and shorter at the poles), together with Landsat 8 Operational Land Imager, and were able to include lakes smaller than 0.125 m^2 whilst still getting a temporal resolution resembling MODIS imagery (2.9 days).

Lake evolution have been found to act differently at different elevations. Bartholomew et al. (2011) found that meltwater accumulated in lakes from mid-June at elevations between 1000 and 1200 meter, and from early July at elevations from 1200 meter to >1600 m. Liang et al. (2012) developed an algorithm for tracking supraglacial lakes and detected lake evolution in West Greenland over ten consecutive melt seasons. The authors found that during years of more melt, supraglacial lakes extended further inland, to higher elevations. The results suggest that with increased melt, areas that previously has not experienced lake formation and drainage are more prone to lake drainage and moulins (Shepherd et al., 2009; Sundal et al., 2009). The subglacial hydrologic system inland is often distributed with inefficient linked cavities, and if these expand with water from the surface, it could increase higher basal water pressure and faster basal sliding (Dow et al., 2015). A warming climate will lead to a growing extent of high-

elevation lakes, and could thereby threaten the stability of the ice sheet (Leeson et al., 2015), and possibly increase ice flow (Doyle et al., 2014).

Cooley & Christoffersen (2017) found an expansion of high-elevation lakes inland by a rate of 6 meters per year, and investigated whether high elevation lakes could drain rapidly. The authors found no significant statistical difference in the fraction of rapidly draining lakes at elevations below and above 1600m, together with no upper elevation limit on rapid lake drainage events. However, a clear distribution in size of rapidly draining lakes relative to elevations was observed, where more lakes that were below 1.5 km^2 in area were rapidly draining below 1000 m elevation, than at higher elevations. This is related to ice velocity variations that initiate fractures being more common at lower elevations, together with the fact the required water volume for rapid lake drainage is smaller at lower elevations (Bartholomew et al., 2011; Catania, Neumann, & Price, 2008; Joughin et al., 2013).

1.3.3 Meltwater plumes

The surface meltwater that is discharged sub-glacially from outlet glaciers into fjords form subsurface plumes (Motyka et al., 2003). The fresh meltwater is lighter than the surrounding warm saline fjord water, and the plumes rise turbulently until they reach neutral buoyancy. As the plumes rise, they entrain ambient fjord water, a process which has been proven to enhance undercutting and calving of outlet glaciers through submarine melting and fjord circulation (Carroll et al., 2015; Fried et al., 2015; Jenkins, 2011; Jouvet et al., 2018; Motyka et al., 2003; Slater et al., 2015; Xu et al., 2012).

At which depth meltwater plumes reach neutral buoyancy depends on the rate of discharge, the density gradient, and the fjord geometry (Bartholomaus et al., 2016; Carroll et al., 2016; Schild et al., 2016; Stevens et al., 2016). The meltwater plumes are therefore amplified by both increased runoff through atmospheric warming, and with ocean warming, linking ocean and atmospheric forces together (Christoffersen et al., 2012). When the buoyancy surpasses the water depth, a plume surface expression appears. In shallow fjords with grounding lines below 500 meters, meltwater plumes most often reach neutral buoyancy in the upper 100 m of the water column (Carrol et al., 2016). The surface expressions of plumes are identifiable through a combination of water colour, fjord water roughness, and the, often semicircular, area from which icebergs or melange has been cleared by divergent flow. The subglacial water often

brings sediments and iron from the glacier bed, colouring the plume in brown and red (Darlington, 2015).

While the density gradient fluctuates on a long-term timescale, the rate of discharge changes more often. Plume surface expressions over time have therefore been used to analyse discharge rate and subglacial drainage systems (e.g. Bartholomaus et al., 2016; Fried et al., 2015; Schild et al., 2016). Appearance and size of plumes along different parts of the glacier front can also be used as an indicator of the spatial variability in discharge. Where spatially distributed plumes are an indicator of well-distributed discharge across the glacier front, and on the contrary, spatially focused plumes indicate locally dominant subglacial channels (Moyer et al., 2017; Slater et al., 2015).

Time-lapse imagery has been used to a certain extent to identify surface plumes and make conclusions on subglacial meltwater transport. Slater et al. (2017) observed the subglacial runoff distribution of Kangiata Nunata Sermia glacier in 2009, through surface plume observations using time-lapse imagery. Their observations suggested spatially distributed channels under the grounding line of the glacier, supplying the fjord with meltwater. Schild et al. (2016) used time-lapse imagery from Rink Isbrae in West Greenland to identify surface plumes. The authors identified four plume locations across the front, where plumes appeared for 2 to 17 hours. The authors concluded that persistent pathways were present and that there was a short-term variability in discharge. The authors also compared plume appearance with lake drainage events, but found no temporal correspondence between drainage and plume occurrence, which led them to suggest that lake drainages were not the primary driver of plumes, possibly due to an inefficient drainage system.

Cook et al. (2020) coupled a subglacial hydrology model with a 1D plume model within the ice-flow model, Elmer/Ice (Gagliardini et al., 2013), to dynamically model the tidewater glacier Store Glacier's subglacial hydrology. The focus was to predict plume and calving activity at the front, and ice flow inland. The authors were able to characterise the efficiency of the basal drainage system, together with investigating how discharge affected melting at the glacier front as meltwater plumes appeared. The plume structure had distinct differences between the two observation years, 2012 and 2017, where the former year received strong, channel-fed plumes along the majority of the front except the very south part, and in the later year plumes were more spatially restricted, and appeared predominantly in two areas; on the northern side of the

front, and close to the deepest part of the front. The modelled plumes from both years can be seen in figure 4.

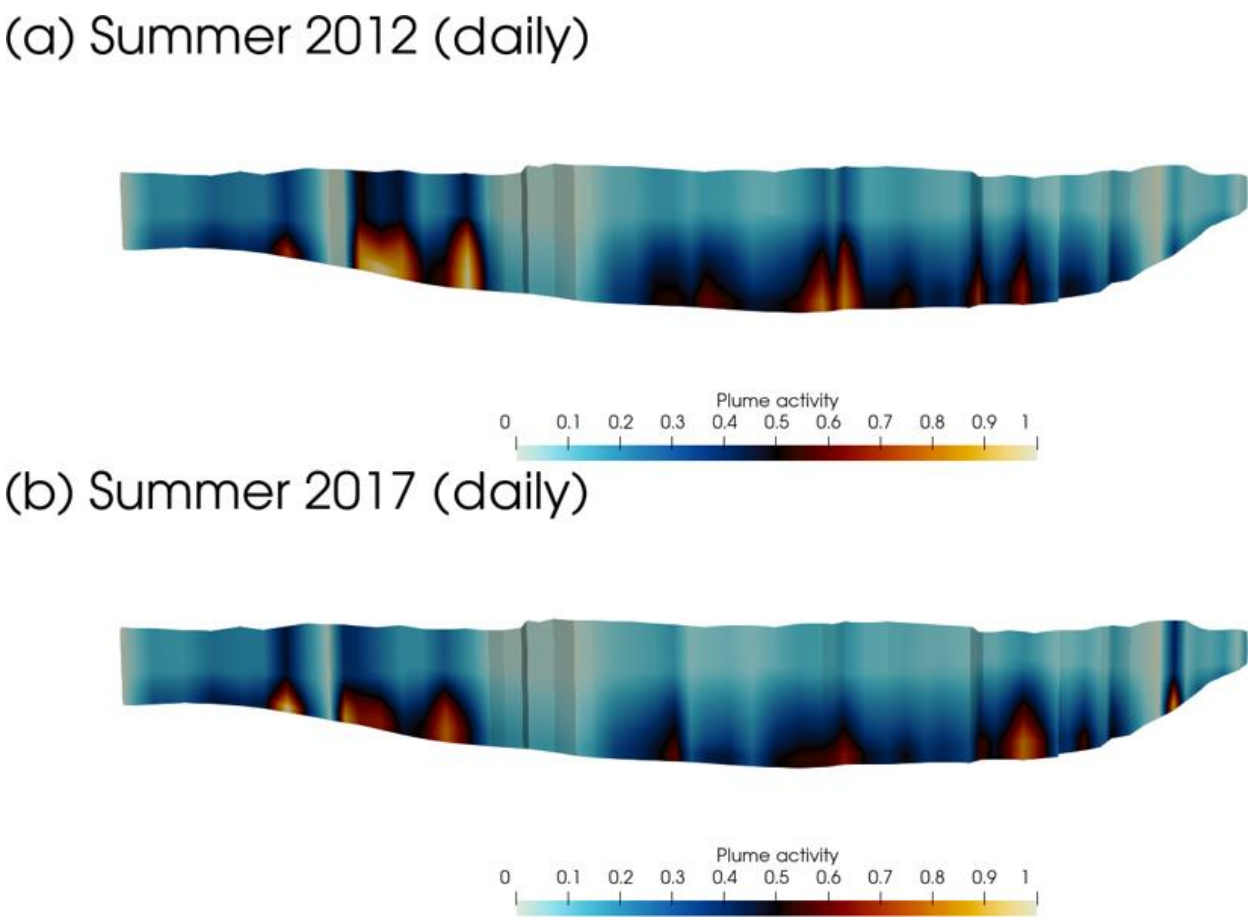

Figure 4. Heat map of simulated plume activity at the Store glacier calving front in **(a)** the summer of 2012 and **(b)** the summer of 2017. Areas with a value of 1 show the highest mean plume melt rates across the entire length of the model run; areas with a value of 0 show no plume activity at any point. Figure from Cook et al. (2020).

1.1.1 Photogrammetry

Photogrammetry is defined as the use of 2D imagery to obtain 3D information about objects or environments. The 3D information can be presented as a measurement, topography map or 3D model. The photographs are captured using satellites, unmanned aerial vehicles or 'drones', airplanes or ground-based platforms (Walford, 2017). The first topographic map was created in 1849, using terrestrial photographs (Granshaw, 2019). The discovery of the stereography effect in 1911 is generally seen as a major breakthrough in photogrammetry, where an instrument, the stereoautograph, was utilized to combine two 2D images to create an illusion of 3D depth (Hinks, 1922). With the invention of airplanes came the second major breakthrough, and aerial photography was introduced in the 1910's (Finsterwalder, 1954). This was an especially important discovery for glaciological research in environments often difficult to reach by foot

(Kääb, 2010). In glaciology research, photogrammetry has been practised to obtain measurements and topographic data since the early 1900's (Fox & Nuttall, 1997). With the launching of the first satellite in the 1970's, spatial coverage reached a new level. The introduction of digital processing in the 1980's offered new ways of data handling, and geographical information systems and digital elevation models were widely used among glaciologists and the rest of the geographical society (Fox & Nuttall, 1997; How et al., 2018; Reinhardt & Rentsch, 1986).

In photogrammetry, 2D photographs from two or multiple viewpoints are used to reconstruct a 3D model of an object or landform (Carrivick et al., 2016). The photographs form "lines of sight" between the camera and points on the observed object, and the lines are used to produce real-world coordinates of the points (Ciciarelli, 1991; Schenk, 2005). The technique is called triangulation, and require the location of the object, a number of ground control points, and six exterior orientation parameters. The parameters are the longitudinal, latitudinal and vertical coordinates of the camera station, and the yaw, pitch, and roll rotations of the camera (Carrivick et al., 2016; Easa, 2010) (see section 3.2.2 for more information).

In glaciology research, aerial and satellite imagery have been utilized to observe glaciological features such as crevasses and moraines (Jennings et al., 2015), and processes such as terminus retreat and surface velocity (Dowdeswell & Benham, 2003; Luckman et al., 2015; Vargo et al., 2017). Terrestrial photogrammetry using time-lapse imagery has been used to observe detailed vertical surface changes (Dietrich et al., 2007; James et al., 2014; Rosenau et al., 2013), velocity measurements by feature tracking (James et al., 2016; Whitehead et al., 2014), meltwater plume surface extents (Schild et al., 2016), and supraglacial lake drainages (Danielson & Sharp, 2013). Time-lapse photogrammetry has enabled observations of short-time processes, such as dynamic ice loss through undercutting and calving (Ahn & Box, 2010; Mallalieu et al., 2017; Pętlicki et al., 2015), and surging processes (Kristensen & Benn, 2012).

1.4 Study Area

The tidewater glacier Store Glacier (*Qarassap Sermia*) is located in Ikerasak Fjord (*Ikerasaup Sullua*), connected to the Ummannaq Fjord system on the west coast of Greenland (70.4° N, 50.55° W) (Todd & Christoffersen, 2014), see figure 5. Ranked 3rd in iceberg discharge among West Greenland glaciers, it has a calving rate of approximately 12 km^3 per year (Hofstede et al., 2018). The active calving front is 5 km wide.

The trunk of the glacier is flowing through a 1000 m deep trough with the front pinned on a sill (Rignot et al., 2015). The glacier has not experienced any observed retreat since 1985 and is therefore classified as a stable Greenland outlet glacier (Catania et al., 2018; Todd et al., 2018).

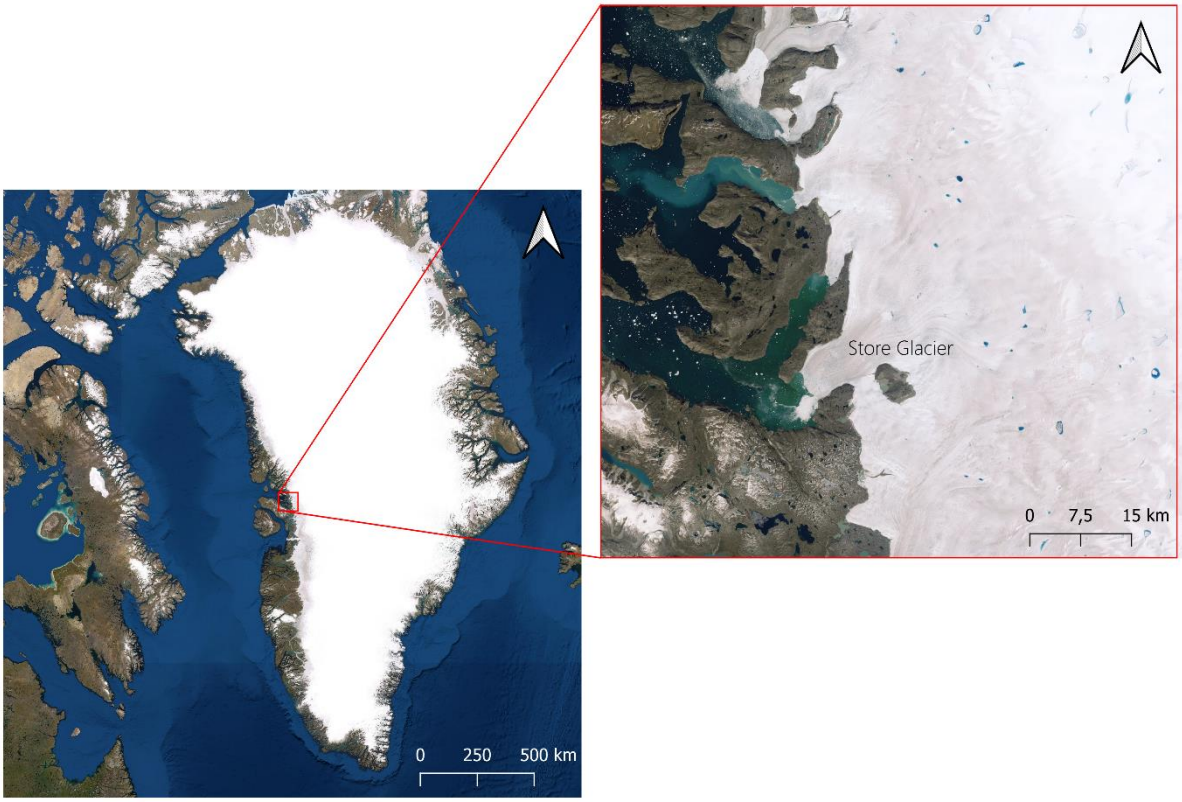

Figure 5. Two maps showing the location of Store Glacier in West Greenland. Base map from ESRI World Imagery dataset.

1.5 Thesis Structure

This thesis is structured into four chapters. Chapter 1 includes dual-satellite analysis of Store Glacier's supraglacial lake volume and drainage during the melting season of 2018. Chapter 2 presents meltwater plume extents at the glacier termini during the same time period, using time-lapse photogrammetry. In chapter 3, I present a summary of main findings from chapter 1 and 2, together with a more in-depth discussion on the connection between supraglacial lake drainage and meltwater plumes, and the subglacial hydrology. In addition, an evaluation of the limitations of this study and future research areas are outlined. In Chapter 4, key findings of this dissertation are presented.

2. Chapter 1: Supraglacial lake drainage

2.1 Introduction

The subglacial drainage system of tidewater glaciers receives water through drainage of crevasses and supraglacial lakes and through moulins during the summer melting season. Supraglacial lake drainage contributes significantly to the evolution of the subglacial drainage system, as well as create dynamic responses to the ice-bed such as ice uplift and increased basal sliding. Analysis of supraglacial lake drainage can therefore provide critical insight on the subglacial hydrology of tidewater glaciers.

Here, supraglacial lake volume and drainage at Store Glacier during the 2018 summer melting season are detected using dual-satellite analysis in the FASTER algorithm (Williamson et al., 2018a).

2.2 Methods

Supraglacial lake volumes were derived using the FASTER algorithm created by Williamson et al. (2018a), and modified by Thomas Chudley to fit my dataset. Williamson et al. (2018a) derived lake areas using a normalised difference water index (NDWI) approach, which showed the per pixel maximum NDWI during the whole input data range (1 May to 30 September). NDWI was defined by McFeeters (1996) as a remote sensing derived index to monitor changes related to water content in water bodies, using green and NIR wavelengths. Williamson et al. (2018a) applied techniques to calculate lake area, depth and volumes from their dual-satellite imagery to the FASTER (Fully Automated Supraglacial lake Tracking at Enhanced Resolution) algorithm, an adapted version of the FAST algorithm (Williamson et al., 2017) which was developed for MODIS imagery.

The FASTER algorithm was used in Google Earth Engine and involved creating an array mask to show the maximum extent of lakes within the Store Glacier drainage basin during the 2018 melt season, by superimposing the lake volumes from each satellite image. Within the mask, changes to lake volumes were tracked between each consecutive image pair, with any lakes that were obscured (even partially) by cloud marked as no data. The script can be found here: https://code.earthengine.google.com/cb4440539c3b5ab2aad7fb861d09082d. The result was cloud- and ice-marginal-free 10-meter resolution lake volume for each day either a Landsat 8 (L8) or Sentinel-2 (S-2) image was available. The average temporal resolution after removal of

outliers were 1.8 days for the whole data period, and during the 1 June to 31 August where most lakes were active: 2.3 days. For the days when both L8 and S-2 imagery were available, the higher spatial resolution Sentinel-2 image was used. I defined peak volume date as the date drainage started. The water volumes reaching the Greenland ice sheet's internal hydrological system from the small and large lakes during the drainage events were determined using the lake-volume measurements on the day of drainage.

A modelled flow routing (available at UK Polar Data Center, created by Bougamont, 2018) showing estimated discharge in $m^3\ s^{-1}$ was draped to the NDWI layer to make out which lakes were part of the Store Glacier drainage basin, see figure 6. 54 supraglacial lakes were identified during the melting season of 2018, see figure 7. Volumes for each lake were downloaded and compiled as CSV files, and the lakes were numbered.

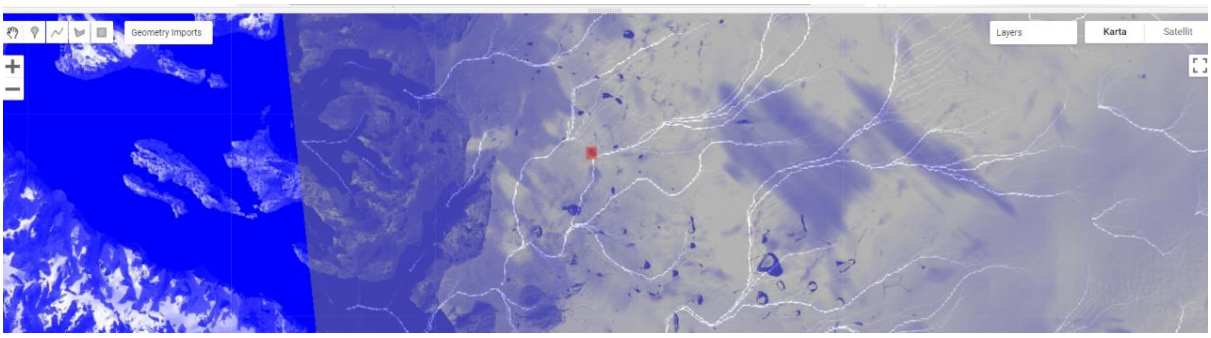

Figure 6. View of NDWI layer used to calculate lake volumes on Store Glacier during the melting season 2018. Overlaid with modelled flow routing layer to identify lakes part of the Store Glacier drainage basin.

Built-in QA bands of L8 and S-2 were used to identify clouds instead of a crude SWIR threshold. The S2 threshold is where its QA bands indicate clouds or cirrus, and L8's threshold uses > 2 ('medium' or above) likelihood of cloud or cirrus. Since the satellite images were not pre-filtered by scene-wide cloud cover, they produced more outliers than Williamson et al. (2018a), but also much denser data. The FASTER algorithm underestimated ground-based volume estimates, evident through a comparison of field-based measurements of Lake 028 (Chudley et al., 2019) which is called lake 42 in this dissertation, where the lake volume were more than twice as large in the ground-based measurements compared to the volume estimates from the dual-satellite analysis. This should be taken into consideration when analysing the results.

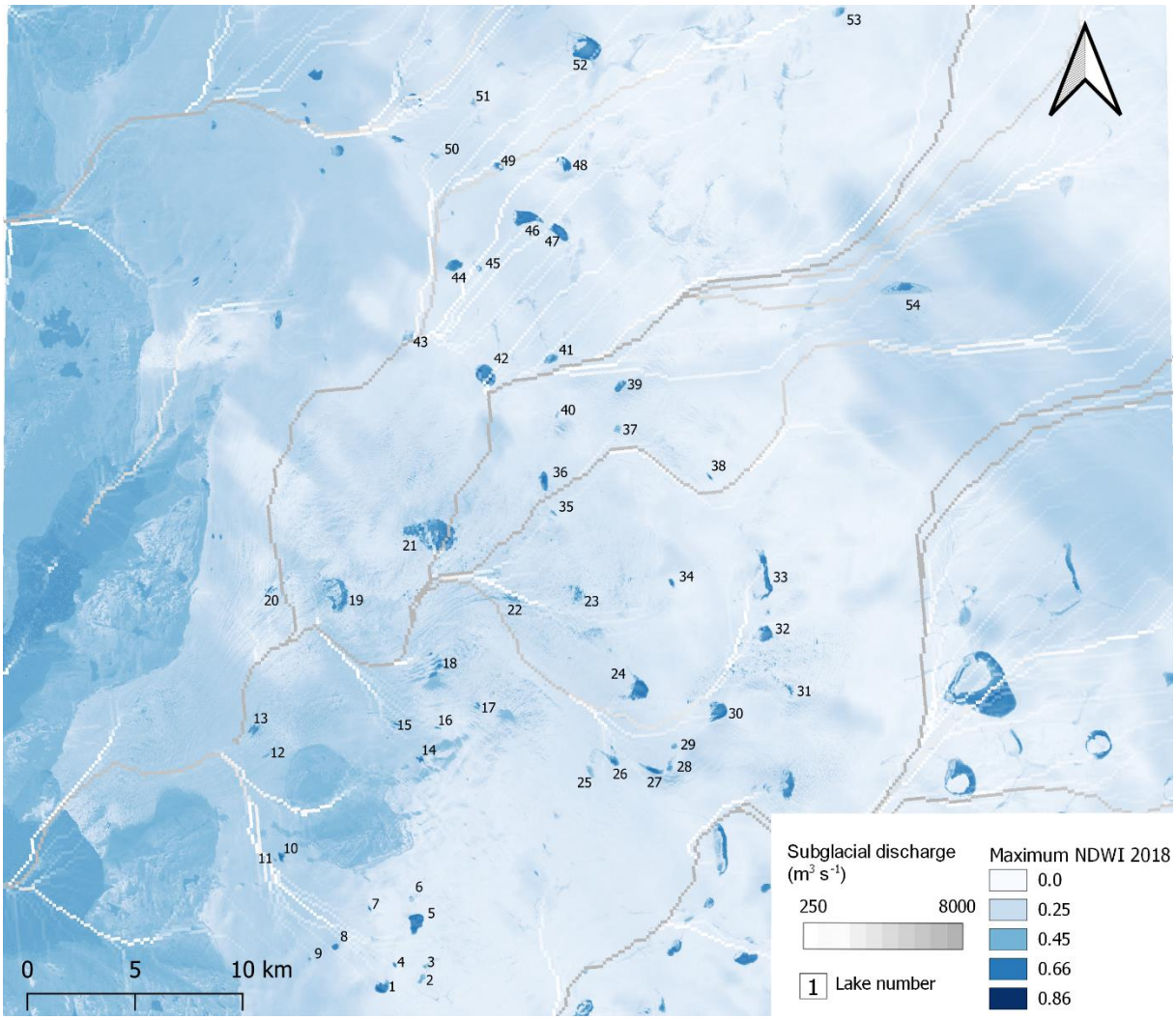

Figure 7. Map showing maximum NDWI on Store Glacier during the melt season 2018, modelled subglacial discharge showing contours of discharge following an input of water to the system, and numbered supraglacial lakes part of the Store Glacier drainage system during the melting season 2018.

Outliers from each lake were removed manually using the GEEDiT v1.012 - Tier 1 imagery tool (Lea, 2018) accessed from https://liverpoolgee.wordpress.com/. The tool enabled rapid flipping through S-2 and L8 data for the time period of the analysis, in order to spot cloud cover above specific lakes. Lake volumes were confirmed through quality checking the volumes of specific L8 and S-2 satellite images, in scripts provided by Thomas Chudley, see figure 8 for reference.

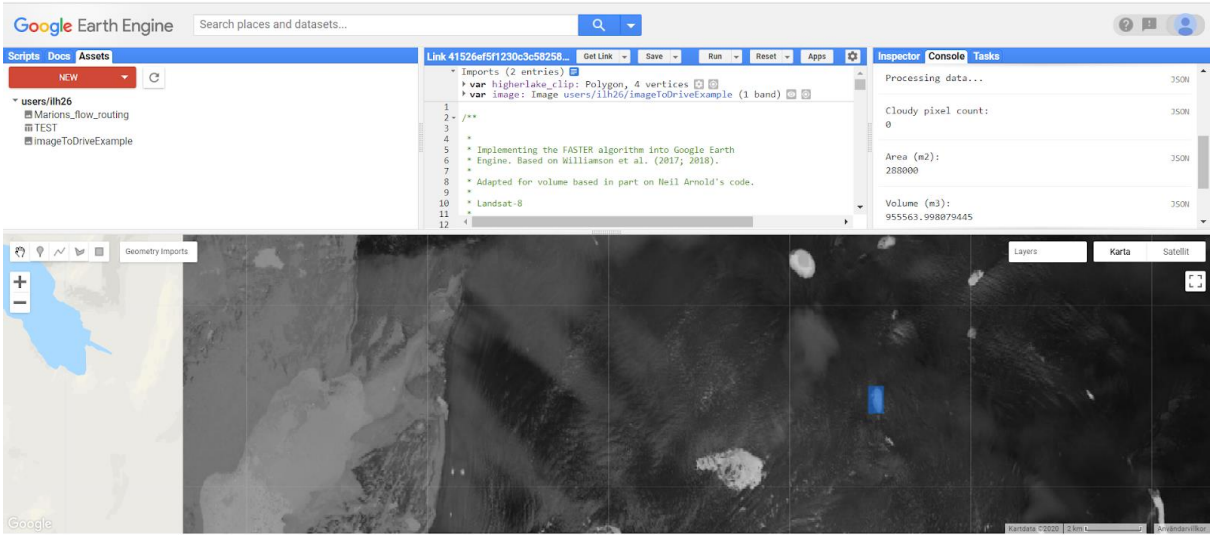

Figure 8. View of Google Earth Engine script for quality checking the volume of lake 36 for 30 July 2018 in a Landsat 8 image.

Graphs of each lake were created, and can be found in appendix A. After removing the outliers, the lakes all had volume measurements from different dates. >47 lakes had data from the same 32 dates, and these were summarized in a graph. A linear interpolation was performed in Python (see script in Appendix B), to produce estimated volume values for all lakes during each date with recorded values. The interpolated total lake volumes were compared with the 32-date volumes to determine if they followed the same trends.

To separate the lake drainages into elevation, nine DEM tiles covering all the Store Glacier lakes were downloaded from the Polar Geospatial Centre (Porter et al., 2018) and mosaicked in QGIS. The geoid EGM2008 1' was downloaded from Agisoft and subtracted from the DEM tiles, in order to get the geoid elevation instead of the ellipsoid. Contour lines for every 500 m elevation rise were created, see figure 9. The lakes were divided into elevation bands of <500 m, 500-1000 m and >1000 m, and graphs of the lakes in each elevation bands were created. The ten largest lakes were determined on and graphs of the total estimated volume and the individual lake volumes were created.

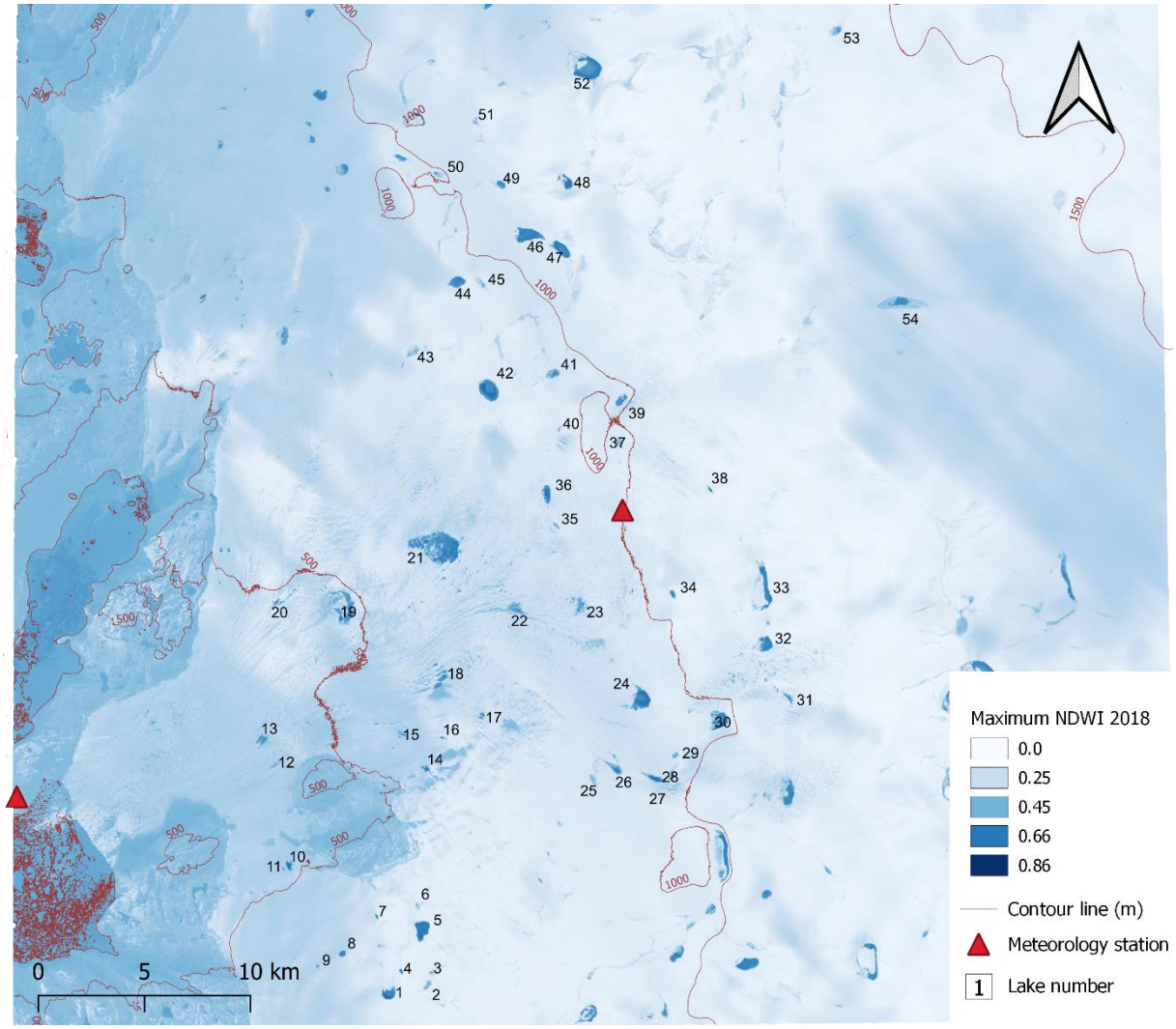

Figure 9. Map showing maximum NDWI on Store Glacier during the melt season 2018, contour lines of 500 metres, two meteorology stations, one close to the front and one 31km inland, and numbered supraglacial lakes part of the Store Glacier drainage system during the melting season 2018.

Meteorology data was attained from two stations, one close to the front of the glacier, R00, and one 31 km inland from the front, R031, both marked out in figure 9. Daily air temperature averages from R00 from the middle to the end of the 2018 melting season were plotted together with a time series of total plume area in figure 30. Daily air temperature averages from R031 were plotted together with a time series of estimated lake volume in figure 12.

2.3 Results

2.3.1 Estimated lake volume and drainage

With the dual-satellite analysis of Sentinel-2 and Landsat 8 imagery, the FASTER algorithm tracked 54 lakes during the summer melting season of 2018. The FASTER algorithm produced time series of each documented lake's volume changes over the season, these can be found in Appendix A. The lakes reached peak volume between 10 June and 16 August, whereas 29 lakes reached peak volume in June, 20 lakes in July, and 5 lakes in August. Total volumetric changes over the whole season were calculated by first performing a linear interpolation to account for dates of missing data due to cloud coverage, and then summing the values of all lakes. To test the validity of the interpolation, the total volume from the 32 dates where >47 lakes had data was calculated. The estimated pattern of lake volume evolution can be seen in figure 10. The pattern showed that lake tracking began in the end of May, with a somewhat steady increase in lake volume until the middle of July, followed by a gradual decrease in volume through the remainder of the season, with all lakes drained or frozen over by mid September. In order to calculate the total estimated lake drainage, the change in volume was divided by the time between each volume estimate. The estimated evolution of lake drainage can be seen in figure 10, and the date of peak volume for each plume can be seen in table 1. Through analysing individual satellite images, it was clear that the three lakes that appeared to drain in mid-August, lake 24, 52 and 53, in fact had frozen over.

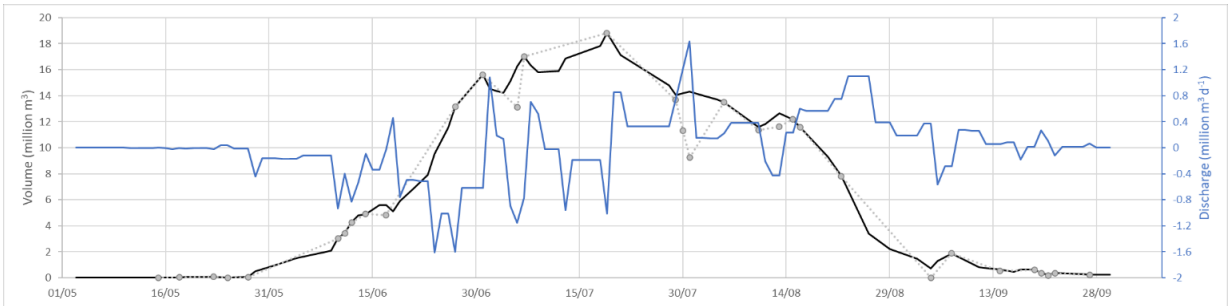

Figure 10. Time series graph of total lake discharge (blue line) and total lake volume (black line) across the whole study region during the 2018 melt season. No data values due to cloud coverage have been linearly interpolated. The total volume from 32 dates where >47 lakes had volume estimates is included (grey dashed line).

Table 1. Showing the date of peak volume, indicating the start of drainage for each respective lake.

Date of peak volume	Lakes
10 June	3, 6, 11, 12, 29
11 June	28
12 June	7,
13 June	2, 9, 22
14 June	14, 25, 40
16 June	10, 20
17 June	17
19 June	5, 19, 21, 23, 26, 27
23 June	37
26 June	35
27 June	1, 4, 8, 13, 15, 18, 38, 43
1 July	16, 30, 31, 34, 41, 45, 50
6 July	42, 49
7 July	44, 51
8 July	39
29 July	54
30 July	32, 33, 36, 46
5 August	47, 48
15 August	52
16 August	24, 53

2.3.2 Rapid lake drainage

Field-based studies have shown that rapidly draining lakes can drain within a few hours (Chudley et al., 2019; Das et al., 2008; Doyle et al., 2013; Krawczynski et al., 2009; Tedesco et al., 2013). To determine rapid drainage detection the ideal criteria would therefore be to observe if the lake drains within a day. However, satellite-based observations of lake volumes do not provide daily observations or, like MODIS, it comes at the expense of spatial resolution, and many lakes are therefore missed. The dual-satellite analysis in this dissertation provides a high spatial resolution, and an average temporal resolution of 1.8 days for the whole data period, and 2.3 days during the period where a majority of the lakes were active (1 June to 31 August). Most satellite-imagery based studies base their rapidly drainage lake detection on disappearance within 2-6 days, which can lead to observation bias. To reduce observation bias, Cooley & Christoffersen (2017) tested several different rapid drainage detection criteria from previous

studies (Fitzpatrick et al., 2014; Liang et al., 2012; Morriss et al., 2013; Selmes et al., 2011) and consequently adapted three new criteria for rapid drainage. The key conditions were:

(i) Lakes are required to drain between two sequential cloud-free images
(ii) Rapid lake drainage is identified either if the lake loses 90% of its maximum area, or the lake loses more than 1.5 km^2 of water while leaving less than 0.25 km^2 of water between two consecutive cloud-free observations.
(iii) Maximum allowed time between two cloud-free observations is 6 days (RD1new), 4 days (RD2new), and 2 days (RD3new), respectively

With the third criteria, there can be no cloud-free observations of lake presence during the 2, 4, or 6 day of the draining period, in order for a lake to be classified as rapidly draining. The new criteria therefore prevent lake drainages that last several days to be misclassified as rapid when sufficient daily cloud-free images are available. Cooley and Christoffersen (2017) found that with the new criteria, 36-45% of all lakes in their 63,000 km^2 study region in West Greenland drained rapidly. Moreover, they did not find a significant difference in rapid lake drainage frequency at different elevations.

Using the FASTER algorithm, Williamson et al. (2018a) had two criteria to identify a rapidly draining lake:

(i) It lost >80% of its maximum seasonal volume in <4 days (following Doyle et al., 2013; Fitzpatrick et al., 2014; Miles et al., 2017; Williamson et al., 2017, 2018b)
(ii) It did not then refill in the subsequent day of cloud-free image by >20% of the total water volume lost during the previous time period (following Miles et al., 2017)

Considering I did not receive lake area measurements from the FASTER algorithm, but did obtain individual volume measurements from all lakes, I used a combination of the two methods for identifying rapidly draining lakes:

(i) Lakes are required to drain between two sequential cloud-free images
(ii) It lost >80% of its maximum seasonal volume between the two sequential cloud-free images
(iii) Maximum allowed time between two cloud-free observations is 6 days (RD1new), 4 days (RD2new), and 2 days (RD3new), respectively

Using these criteria, rapid lake drainages accounted for 6.8%, 2.8%, and 0%, for RD1new, RD2new, and RD3new; 3, 1, and 0 lakes, respectively. The three lakes that drained rapidly in RD3new were lake 34, 40 and 53. However, at a closer look at the satellite images of lake 53 it was obvious that the lake did not drain rapidly, but froze over. Lake 53 was located at a distance of ~51 km from the front, and was the lake furthest from the front. Examples of a rapidly draining and a slow-draining lake can be seen in figure 11. The criteria were adjusted by changing the critical volume to >60% loss, and 13.6% (RD1new), 11.1% (RD2new) and 9.1% (RD3new), i.e. 6, 4 and 2 of the lakes were then identified as rapidly draining lakes.

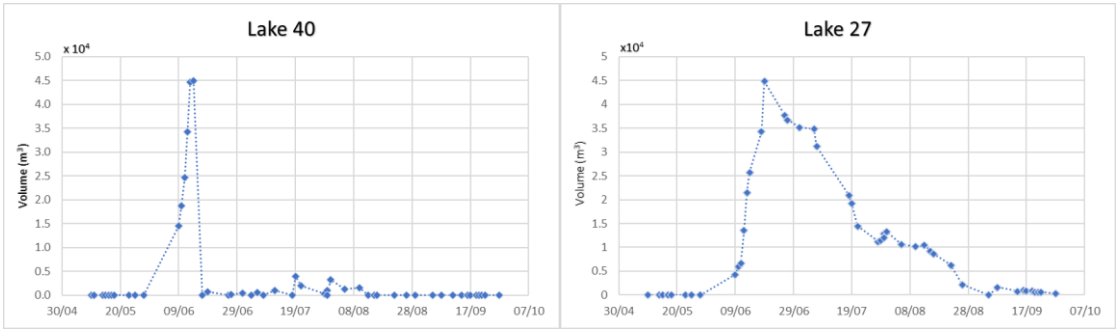

Figure 11. Time series graphs of lake volume for a rapidly draining lake (left), and a slow draining lake (right).

2.3.3 Lakes in elevation bands

The 54 lakes were divided into elevation bands of 500 meters, in order to determine variances in volume and drainage between different elevations. No lakes were observed above 1500 m elevation. Lakes at elevations <500 m were located ~9-16 km from the glacier front, while the lakes at elevations of 500-1000 m were located ~16-36 km from the glacier front. Lakes at elevations >1000 m were located ~30-51 km from the glacier front. A time series graph of the estimated total lake volume divided into elevation bands can be seen in figure 12, together with air temperature from a meteorology station 31 km inland of the glacier front. The position of the station is marked out in figure 9.

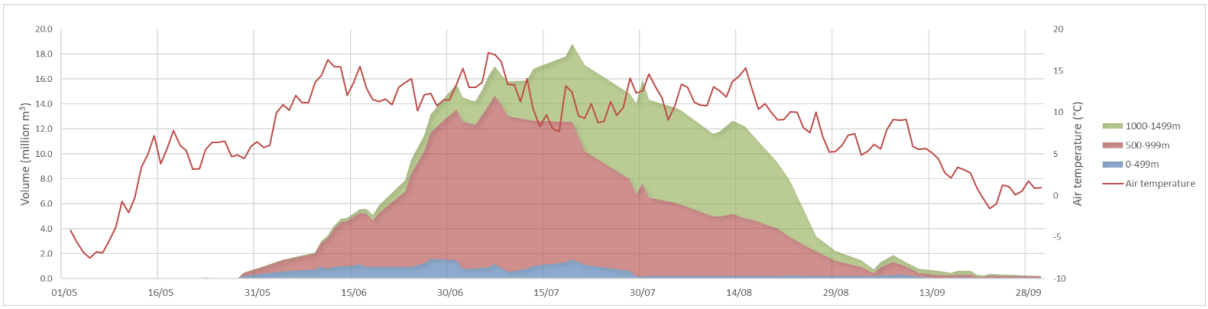

Figure 12. Time series graph of total estimated lake volume on Store Glacier during the melting season 2018, divided into elevation bands of 500 m (left hand y-axis), and air temperature (right hand y-axis) from a meteorology station 31km inland of the glacier front.

Lakes at lower elevation reached peak volume and began to drain earlier in the season, than lakes at higher elevations. Lakes <500 m elevation reached peak volume between 10 June and 19 July, median date 16 June. Lakes between 500-1000 m elevation reached peak volume between 10 June and 16 August, median date 27 June. And lakes >1000 m elevation reached peak volume between 27 June and 16 August, median date 30 July. Time series of lake volumes divided into elevation bands can be seen in figure 13, where the ten largest lakes, identified as the lakes reaching >1 million m^3 of water at some point during the melting season, are marked out with their respective numbers.

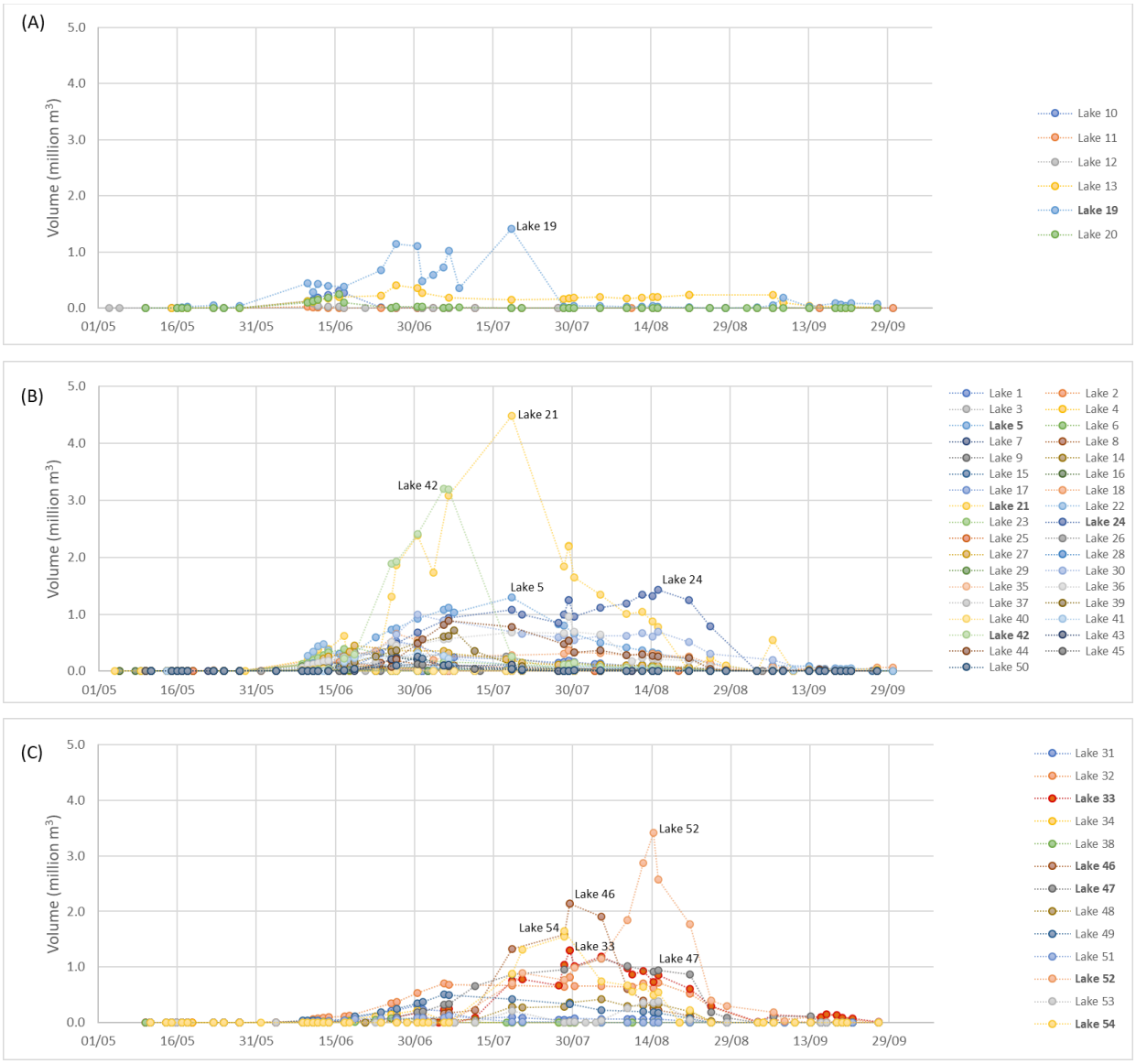

Figure 13. Time series graphs showing lake volume of all 54 of Store Glaciers supraglacial lakes during the melting season 2018 at **(A)** <500 m.a.s.l., **(B)** 500-1000 m.a.s.l., and **(C)** >1000 m.a.s.l. The ten largest lakes (peak volume >1.0 million m^3) are marked out with their respective number.

2.3.4 Ten largest lakes

The ten largest lakes are identified as the lakes that stored more than 1 million m^3 of water at some point during the melting season of 2018. The total volume of the ten largest lakes followed the same pattern as the total volume of all 54 lakes, as can be seen in figure 14. Five of the ten lakes stored more than 2 million m^3 of water at some point, and one lake, lake 21, stored more than 4 million m^3 of water at some point. The volume of each of the ten lakes can be seen in figure 15. The peak volume estimate, date of peak volume, date of the next cloud-free image after peak volume, total drainage between the two images, estimated drainage per day, and the elevation band of the ten largest lakes can be seen in table 2.

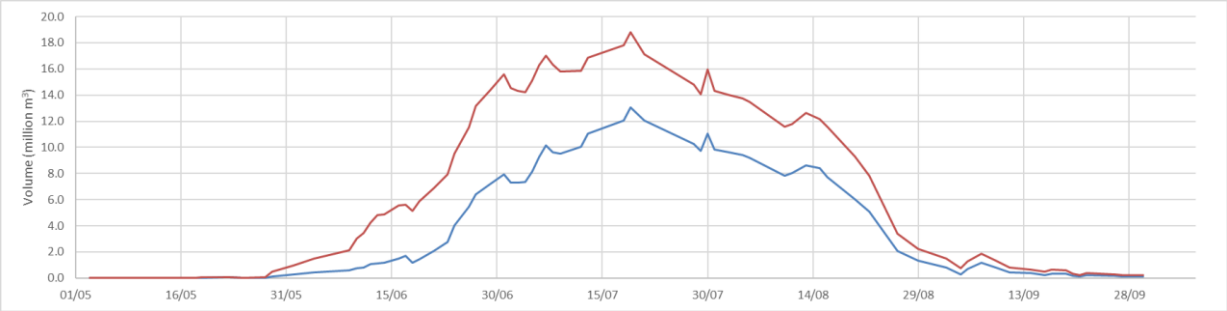

Figure 14. Time series graph showing the total volume of the 10 largest (>1 million m^3 of water) lakes (blue line) and the total volume of all lakes (red line) on Store Glacier during the 2018 melting season.

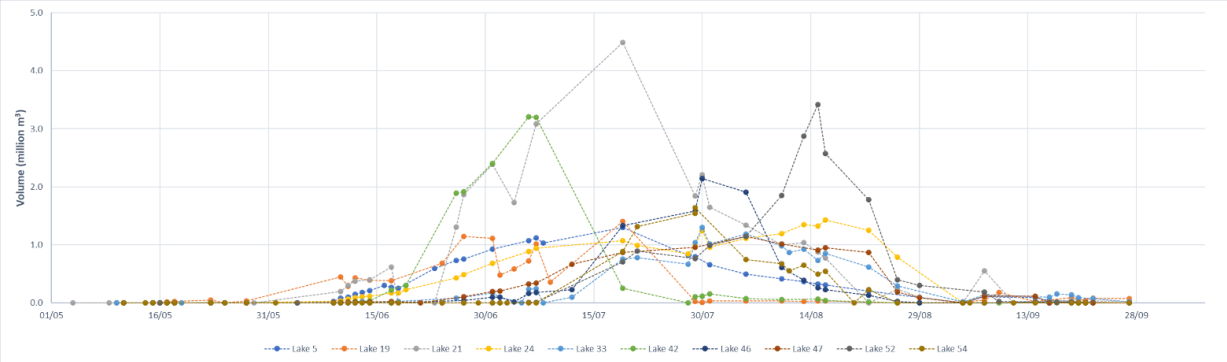

Figure 15. Time series graph showing lake volume change of each of the 10 largest (>1 million m^3) lakes on Store Glacier during the 2018 melting season.

Table 2. Showing the peak volume, date of peak volume, date of the next cloud-free image, total drainage (Q) between the two images, estimated drainage per day, and the elevation band of the ten largest lakes observed on Store Glacier in 2018.

Lake	Peak volume (m^3)	Date of peak volume	Date of next image	Q (m^3)	Q per day (m^3 d^{-1})	Elevation (m)
5	1,295,375	19/7	28/7	472,097	52,455	500-1000
19	1,408,139	19/7	29/7	1,381,709	138,171	<500
21	**4,485,666**	19/7	29/7	2,640,217	264,022	500-1000
24	1,431,408	16/8	22/8	181,551	30,259	500-1000
33	1,301,743	30/7	31/7	284,992	284,992	>1000
42	3,205,363	6/7	19/7	2,952,313	227,101	500-1000
46	2,143,116	30/7	5/8	234,911	39,152	>1000
47	1,148,512	5/8	10/8	130,102	26,021	>1000
52	3,415,062	15/8	16/8	843,084	843,084	>1000
54	1,642,156	29/7	5/8	898,182	128,312	>1000

For lake 42, ground based measurements from 2018 were available from Chudley et al. (2019). The authors noticed a drainage event beginning right after peak volume at 7 July 17:46; 7,295,612 m^3, and qualifying as a rapid drainage (defined as >50 m^3 s^{-1}) between 18:32 and 23:22 PM. During this time the lake drained 4,953,091 m^3, which equivalates to 68% of peak volume. Time series of the volume estimates before, during and after the major drainage event can be seen in figure 16. From the ground-based measurements it appeared that the FASTER algorithm underestimated the volume estimates of Lake 42 by >50%. Moreover, considering there were no cloud-free image from peak volume to right after drainage, the lake was not classified as a rapidly draining lake according to the criteria, even though a rapid drainage event did in fact occur. This shows that the dual-satellite record did not pick up certain rapid lake drainage events, due to low temporal resolution.

Figure 16. Time series graph showing the volume estimate of lake 42 before, during and after the large drainage event on 7 July 2018, based of ground-based measurements by Chudley et al. (2019).

2.4 Discussion

2.4.1 Estimated lake volume and drainage

Dual-satellite imagery from Sentinel-2 and Landsat 8 were used in the FASTER algorithm (developed by Williamson et al., 2018a and modified by Thomas Chudley) to produce volume estimates of supraglacial lakes on Store Glacier during the 2018 melting season. Several previous studies of supraglacial lake evolution have used either high temporal satellites like MODIS (Box and Ski., 2007; Fitzpatrick et al., 2014; Liang et al., 2012; Sundal et al., 2009; Williamson et al., 2017) or high spatial resolution satellites like Sentinel or ASTER (Arnold et al., 2014; Banwell et al., 2014; Chen et al., 2017; Georgiou et al., 2009; Gledhill and Williamson, 2018; Legleiter et al., 2014; Macdonald et al., 2018; McMillan et al., 2007; Miles et al., 2017; Moussavi et al., 2016; Pope et al., 2016; Sneed and Hamilton, 2007). However, with MODIS imagery lakes smaller than 0.125 m^2 are excluded, and with only Sentinel-2 or Landsat 8 the highest temporal resolution is 5 days. The dual-satellite method in this study enabled a combination of high temporal (1.8 days during the entire time period, and 2.3 days during the time period when most lakes were active; 1 June to 31 August) and high spatial (10-30 m) resolution. The method tracked the evolution of 54 lakes, with peak volumes ranging from 28,822 m^3 (lake 11) to 4,485,666 m^3 (lake 21). The mean peak volume was 640,268 m^3, the median peak volume was 310,217 m^3.

In 2018, the lakes at Store glacier started filling with water in the end of May, however the first lake drainage did not start until 10 June (see table 1). During the remainder of June, 32 of the lakes started draining, with six and eight of the lakes reaching peak volume and started draining the 19 and 27 June, respectively. 17 lakes started draining during July, with seven of the lakes reaching peak volume the 1 July. According to the FASTER algorithm, remaining five lakes started draining early to mid August. However, through analysis of individual satellite images, the three lakes that appeared to drain in mid August were instead found to freeze over.

Draining lakes can in some instances increase tensile stress in the surrounding area, and lead to other lakes draining in a cascading lake-drainage process (Christoffersen et al., 2018). Indications of hydrological links between lakes with similar draining patterns and in close proximity were found for lakes 2, 3, 6 and 7 which all started draining between 10-13 June, lakes 26 and 27 where drainage started 19 June, lake 1, 4 and 8 where drainage started 27 June, lakes 15 and 18 where drainage started 27 June, lake 30 and 31 where drainage started 1 July,

lake 32 and 33 where drainage started 30 July, and for lakes 47 and 48 where drainage started 5 August, see table 1 and figure 9 for reference.

2.4.2 Rapid lake drainage

The variables that determine rapid lake drainage are the local stress regime, the presence of pre-existing fractures, basal motion and a required water volume threshold, which is determined by ice thickness, ice temperature and fracture geometry (Stevens et al., 2015). The importance of identifying rapidly draining lakes from slow draining lakes are three-folds. Firstly, recent studies have shown that moulins opened by these events continue to allow great run-off volumes to reach the subglacial drainage system, also after the lake is drained (Banwell et al., 2016; Koziol et al., 2017). The moulins can in some instances stay open for the rest of the season (Koziol et al., 2017). Secondly, rapid drainage can cause short-term enhanced basal sliding (Andrews et al., 2014; Banwell et al., 2016; Bartholomew et al., 2011) and possibly affect the ice deformation rate (Lüthi et al., 2015; Phillips et al., 2010; Poinar et al., 2017). And thirdly, rapidly draining lakes increase tensile stress in the proximity to other lakes, and can in some instances lead to a cascading lake-drainage process (Christoffersen et al., 2018). Slow drainage is however also important to identify, as water from a slow draining lake can overflow a stream and cause basal uplift or sliding (Stevens et al., 2015; Tedesco et al., 2013).

Other studies have shown that rapid lake drainage occur on 28 to 45 % of all supraglacial lakes in West Greenland (Cooley & Christoffersen, 2017; Fitzpatrick et al., 2014). In this study, rapid lake drainage was identified using a combination of criteria developed by Cooley & Christoffersen (2017) and Williamson et al. (2018a). When rapid drainage is defined by a loss of >80% of peak volume and the maximum allowed time between two cloud-free observations is 6 days, 7% of the lakes were found to drain rapidly. The lakes that appeared to drained rapidly were lake 33, 40 and 53. However, as previously mentioned, lake 53 did not drain rapidly as satellite images made it clear the lake froze over. Removing lake 53 resulted in 4.7% of the lakes rapidly draining.

Nonetheless, by analysing the lake drainage of each of the 54 lakes, it is clear that some of the lakes have a much steeper drainage curve than others. Due to gaps in observations because of cloud-coverage, especially during the time period 19-28 July where only one cloud-free image from the dual-satellites was available and seeing as a number of lakes drained during this time, it is possible that some rapidly draining lakes are missed using these criteria. Moreover,

Chudley et al. (2019) completed field measurements of lake 42 at Store Glacier in the summer 2018 (called Lake 028 in their study) and found that on 7 July, the lake drained rapidly for five hours, losing 68% of its volume.

The rapid lake drainage of lake 42 was not picked up by the criteria in this study, due to the fact that the lake only drained partially, together with the fact that there wasn't sufficient cloud-free imagery between peak volume and drainage to identify it as a rapidly draining lake. The reduction in temporal resolution during certain periods of the season due to cloud-cover could therefore result in lakes being wrongly identified as slow-draining. This could be managed by using Sentinel-1 imagery, which can pick up lake detection through clouds and in darkness (Miles et al., 2017). However, Sentinel-1 have a lower temporal resolution than Sentinel-2 which is why it was ultimately not used in this study.

2.4.3 Lakes in elevation bands

The subglacial drainage system typically appears different at certain elevations of the ice sheet. At low elevations there are sufficient hydrological gradients needed for viscous heat dissipation, and efficient subglacial channels can form. At high elevations where the ice sheet is thicker and flatter, the thick ice promotes subglacial channel closure by creep and the water entering the system typically reach distributed and inefficient linked cavities. When water drained from supraglacial lakes reach the cavities they expand, inducing high basal pressure and faster basal sliding (Dow et al., 2015; Meierbachtol et al., 2013). Water from supraglacial lakes can also modify the seasonal efficiency of the subglacial system (Andrews et al., 2018; Hoffman et al., 2011; Sundal et al., 2011), and open new surface-to-bed connections, increasing meltwater input to the system throughout the season (Catania & Neumann, 2010; Hoffman et al., 2018).

Higher temperatures due to anthropogenic climate change will increase surface melt at the Greenland ice sheet, leading to an increase in supraglacial lake formation. Both models and satellite analysis prognose supraglacial lakes will continue to progress inland (Ignéczi et al., 2016; Leeson et al., 2015). In order to comprehend what will happen if supraglacial lakes keep forming further inland, it is important to understand how the subglacial drainage system behaves at different elevations. For example, if the subglacial drainage system at higher elevations seems to stay distributed and inefficient throughout the season, that could mean that an increase in supraglacial lake drainage in these areas leads to an increase in ice flow. Doyle

et al. (2014) found support for this analysis, where GPS records showed annual increases in ice flow at 1,840 m.a.s.l in Southwest Greenland.

At Store Glacier, high basal water pressure was found 30 km inland from the front, indicating a largely inefficient basal water system in the upper part of the glacier (Doyle et al., 2018). Young et al. (2019) completed velocity measurements of Store Glacier in 2014-2015, and found seasonal fluctuations indicating a channelized subglacial drainage system may develop closer to the front.

Time series of volumes of the 54 supraglacial lakes in this study were divided into elevation bands of 500 meters (see figure 9). The results showed that lakes at elevations of >1000 m generally reached peak volume and began drainage later in the season (median date 30 July), than lakes <500 m (median date 16 June), and lakes between 500-1000 m elevation (median date 27 June), see figure 13 for a comparison of all the lakes. Lakes at elevations <500 m were located ~9-16 km from the glacier front, while the lakes at elevations of 500-1000 m were located ~16-36 km from the glacier front. Lakes at elevations >1000 m were located ~30-51 km from the glacier front. All the lakes that drained before 27 June were situated below 1000 m in elevation (see table 1 and figure 9 for reference). This is consistent with earlier studies showing supraglacial lakes typically drain at progressively higher altitudes over the course of the melt season (Clason et al., 2015; Sundal et al., 2009).

The results indicate that lakes at higher elevations did not induce increased efficiency of the supraglacial drainage system early in the season, and the fact that they opened new surface-to-bed connections only later in the season, meant that the delivery of meltwater to the bed through these connections was only possible in the later part of the melting season. Later drainage of lakes at higher elevations therefore could extend the already existing divide between an efficient drainage system at lower elevations and an inefficient drainage system at higher elevations.

2.4.4 Ten largest lakes

Time series showing the estimated lake volume of the ten largest lakes, which all stored >1 million m^3 of water at some point of the melting season, followed the same path as the estimated total volume for all lakes, see figure 14. During total peak volume on 19 July, 70% of the total observed lake water volume was stored in the ten largest lakes; 13.1 million m^3 out of 18.8 million m^3 of water.

Lake drainages of the ten lakes were analysed based on elevation and drainage date. One lake at 500-1000 m elevation started draining already 6 July. Two lakes at 500-1000 m elevation and one lake <500 m elevation started draining 19 July. Three lakes >1000 m elevation started draining 29-30 July. One lake >1000 m elevation started draining 5 August. The two remaining lakes at 500-1000 m and >1000 m elevation, lake 24 and 52, appeared to drain in mid-August, but through analysing individual satellite images it was clear that they had frozen over. Lake 24 and 52 were located at a distance of ~43 km and ~27 km from the front, respectively. Lake 42 and 21 drained the most water; 2.95 million m^3 and 2.6 million m^3 respectively.

The elevation of the ten largest lakes was analysed. Five of the ten largest lakes were positioned >1000 m in elevation, while four lakes were positioned between 500-1000 m and only one lake <500 m. This supports the observation that lakes at lower elevations drain earlier in the season, before they can reach equal volumes to the higher elevation lakes. It is important to observe the elevation of large lakes, since rapid drainage at high elevations, where the subglacial system is typically inefficient with distributed cavities, can expand cavities and induce basal pressure and faster basal sliding (Dow et al., 2015) and threaten the stability of the ice sheet (Leeson et al., 2015). With this in mind, since five of the ten largest lakes in 2018 were positioned >1000 m in elevation, rapid drainage of the lakes could have implications for the basal pressure and stability.

Rapidly draining lakes have been observed to be on average greater than other lakes, and greater water volumes will more likely be able to force a fracture all the way to the bed (Stevens et al. 2015). However, other variables such as the local stress-strain regime, presence of pre-existing fractures and basal motion also play in, meaning great volume is not a clear indicator of a rapidly draining lake. However, Chudley et al. (2019) did observe a rapid drainage event on lake 42 in 2018, the third largest lake, with peak volume of 3,205,363 m^3.

2.5 Conclusions

Previous studies have shown that supraglacial lake drainage contributes substantially to the formation and evolution of the subglacial drainage system. The aim of this chapter was to quantify supraglacial lake volumes in order to establish a record of volume losses and discharge at Store Glacier, during the melting season of 2018.

Volume change and drainage of 54 supraglacial lakes on Store Glacier during the melting season 2018 were observed using dual-satellite imagery. The lakes differed in size, with peak volumes ranging from 28,822 m^3 (lake 11) to 4,485,666 m^3 (lake 21). Total peak volume of 18.8 million m^3 was reached 19 July, at that point 70% of the water came from the ten largest lakes. Low elevation lakes (<1000 m) reached peak volume on average earlier in the season than higher-elevation lakes (>1000 m). Approximately 5%, i.e. 2 of the lakes drained rapidly during the season, both situated at approximately 1000 m elevation. Lake drainage occurred between 10 June and 15 August, after that the lakes that appeared to drain had in fact frozen over. Five peaks in drainage were observed, the first one occurred 18 June, the second 2 July, the third 8 July, the fourth 20 July and the last and largest drainage event occurred 31 July.

3. Chapter 2: Meltwater plume extent

3.1 Introduction

Water leaving the subglacial drainage system at the terminus of tidewater glaciers form buoyant meltwater plumes. During periods of high discharge, the surface extents of plumes are visible through time-lapse cameras. Analysis of these meltwater plumes can help reconstruct the subglacial hydrology of tidewater glaciers.

Here, plume activity and surface areas are detected using time-lapse photogrammetry in the Python toolbox PyTrx (How et al., 2018).

3.2 Methods

3.2.1 Dataset

The dataset used for the plume analysis consisted of time-lapse images from the Store Glacier frontal margin. Nine terrestrial time-lapse cameras were positioned around the Store Glacier frontal margin in July 2017. The cameras were left year-round, capturing photos every five minutes in 2017, and hourly in 2018-2019. The cameras chosen for this project were the North1 (hereby known as the North camera) and South1 (hereby known as the South camera) cameras, see figure 17. The two cameras were chosen for their joint view of the entire glacier's terminus and adjacent fjord, to be able to fully capture the appearance of plumes.

Since the melting season had already begun when then cameras were installed in 2017, the melting season of 2018 were chosen, and images captured between 31 May and 30 September were utilized. The 31 May was the official start date of the melting season in Greenland 2018, and the end of the melting season in 2018 was late August. However, since there might be a time-lag between surface melt and subsequent plume appearance, an extra month of data was included. The images, originally in CR2-format, were converted to JPG format in File Viewer Plus 3 (https://fileviewerplus.com/). From the North camera 2329 photos were used, starting from 31 May 01:02 and ending 30 September 19:04, and from the South camera 2427 photos were used, starting from 31 May 00:46 and ending 30 September 10:43.

Figure 17. Photographs of the position of the South (left) and North (right) cameras. Photographs from Antonio Abellan.

To automatically calculate the plume area extent, the Python Toolbox PyTrx (How et al., 2018) was used. The code was available and downloaded directly from the GitHub repository (https://github.com/PennyHow/PyTrx). Anaconda 3 2020.02 (64-bit) was downloaded and through Anaconda the necessary packages OpenCV (v3 and above), GDAL (v2 and above), Pillow (v5 and above), together with datetime, glob, math, Matplotlib, NumPy, operator, os, pathlib, PyLab, SciPy, struct and sys were downloaded. Python 3.7.1 [MSC v.1912 64 bit (AMD64)] and iPython 7.13.0 were used in the environment Spyder 4.1.3. The TkAgg backend for Matplotlib was used.

The PyTrx workflow can be seen in figure 18, plume areas were calculated through the Area class object. The camera environment files (CamEnv), the camera calibration files (CamCalib), the ground control points (GCPs) and the digital elevation model (DEM) were all modified to fit with the time-lapse images captured at Store Glacier.

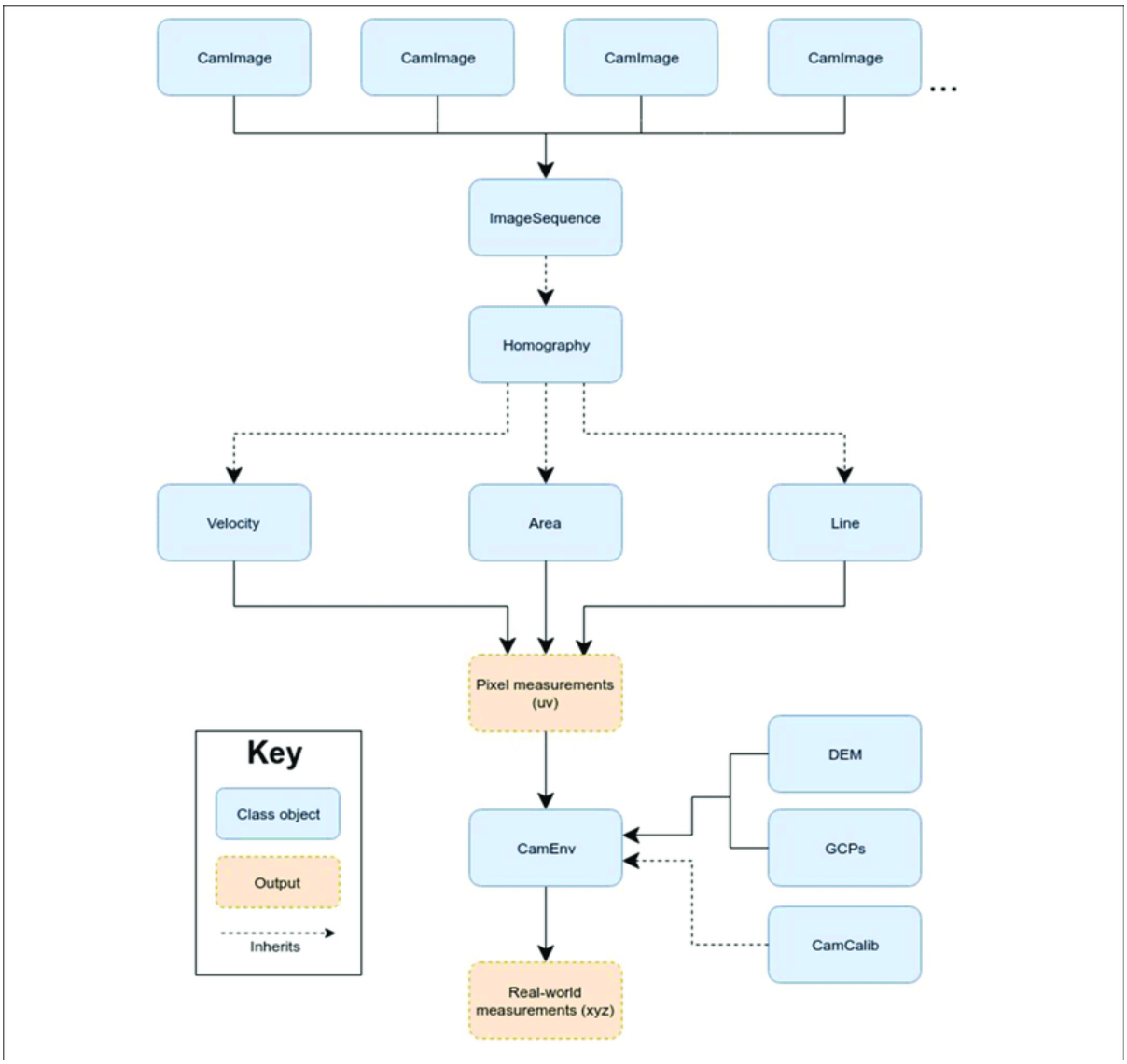

Figure 18. Showing the PyTrx workflow and how each of the class objects interact with one another. Figure from How (2018).

3.2.2 Camera calibration

The purpose of the camera calibration was to correct the images for distortion. The camera calibration was computed using a set of calibration images taken with the North and South time-lapse cameras. The calibration images were black and white chessboard images taken from all angles, and x and y coordinates were defined using the positioning and distance between the corners (Solem, 2012). All the chessboard images were added into the photogrammetry software Agisoft Metashape Professional, where a lens calibration was completed. The output provided focal length (in mm), principal point offsets, tangential distortion coefficients, radial distortion coefficients, affinity and skew, see figure 19. A more detailed explanation of using chessboard images for camera calibration is found in Penelope How's PhD thesis (2018).

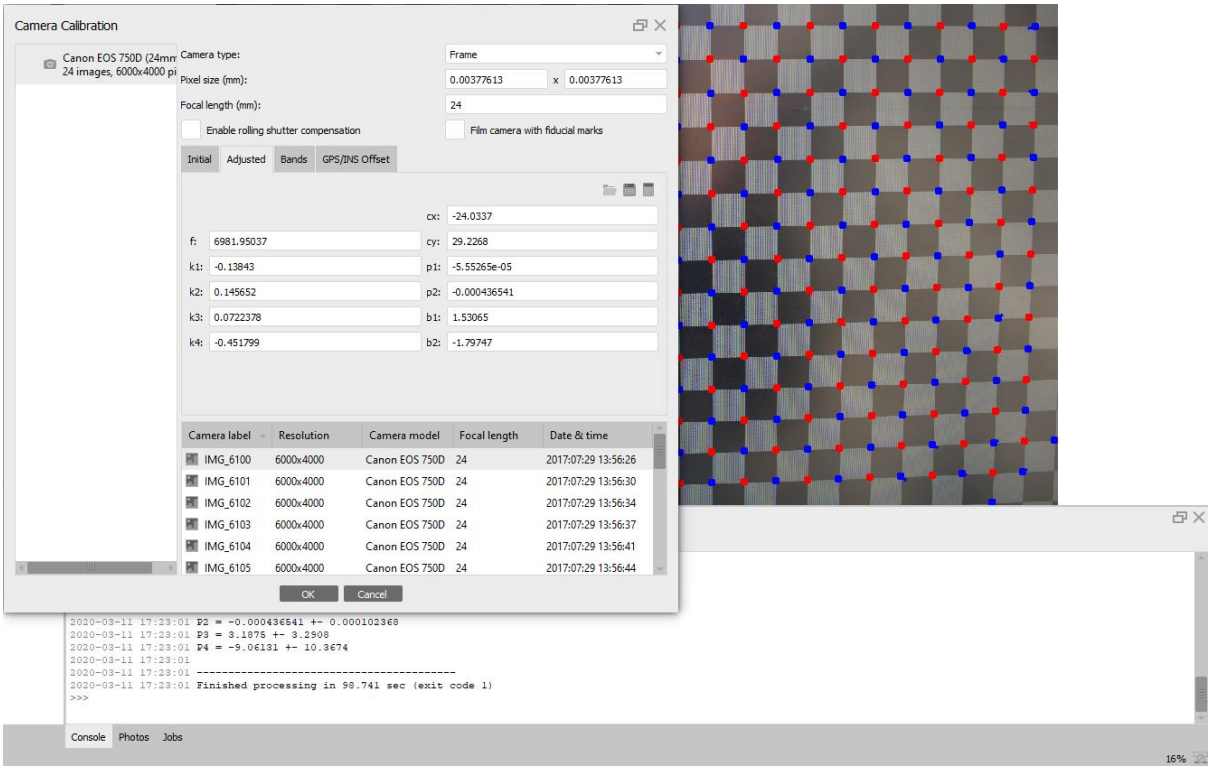

Figure 19. View of the South camera lens calibration in Agisoft Metashape using chessboard images, resulting in focal length in mm (f), principal point offsets (cx, cy), tangential distortion coefficients (p1, p2), radial distortion coefficients (k1-k4), affinity (b1) and skew (b2).

Camera calibration can be divided into extrinsic camera parameters (to locate the camera in three-dimensional space), and intrinsic camera parameters (to convert from a three-dimensional space to a two-dimensional plane). The extrinsic camera parameters consist of matrices of camera rotation and camera translation.

The intrinsic camera parameters consist of:

(i) Focal length values in pixels, where focal length in mm was provided by the Agisoft lens calibration and the focal length pixel values were received through calibration in PyTrx.

(ii) Principal point, which informs about the position of the image centre. Due to imperfections during camera manufacture, the principal point is not always equal to the physical centre of the image (Busch, 2014). The principal point offset is the difference between the principal point and the physical centre of the image (Hartley and Zisserman, 2004). The principal point offset was received from the Agisoft lens

calibration and the PyTrx camera optimisation routine was used to refine the camera parameters.

(iii) The camera pose, which is the position of the camera during image capture. It is defined by the yaw, pitch and roll rotations (also known as omega, phi and kappa) (James et al., 2016; Messerli and Grinsted, 2015). The yaw is the aspect of the camera and is measured as a rotation around the vertical axis. The pitch is the angle of the camera relative to the target surface and is measured as a rotation around the lateral axis. The roll is the rotation around the longitudinal axis. See figure 20. The yaw, pitch and roll measurements were received from Agisoft by adding an image from the North and South camera and using the estimated camera pose. However, the roll values given were not correct and therefore I kept them as zero.

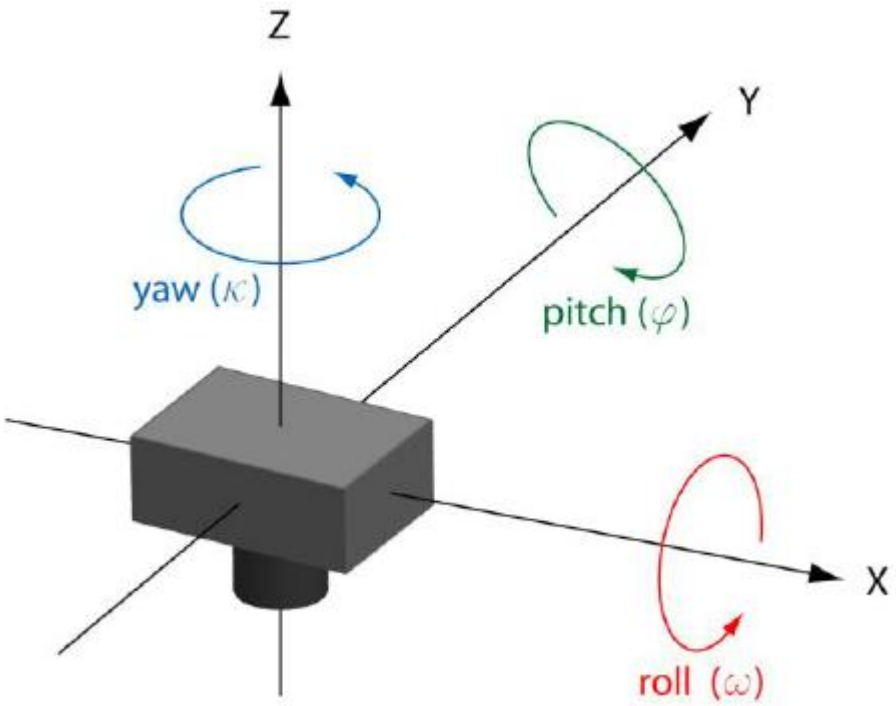

Figure 20. Showing the camera pose parameters pitch, yaw, and roll. Figure from Verhoeven et al., (2013).

(iv) Camera skew, which is the measure of the angle between the x and y pixel axes. This is often negligible and assumed to have little effect (Matlab, 2017; Mordvintsev & Abid, 2017), hence is was set to zero in this analysis.

(v) Distortion coefficients

a. Radial distortion

This distortion originates from the symmetry of the camera lens. Two radial distortion coefficients (k1 and k2) received from the Agisoft lens calibration were used to represent the radial distortion.

b. Tangential distortion

This distortion is caused by misalignment of the camera lens and the camera sensor, causing depth perception in images (Hartley and Zisserman, 2004). Two tangential distortion coefficients received from the Agisoft lens calibration were used to represent the tangential distortion.

3.2.3 Ground Control Points and Digital Elevation Model

The time-lapse camera tends to move during the time-period of image capture, due to wind, instabilities in the installation, ground movement, thermal expansion in the tripod and/or animal or human disturbance. It produces false motion to the measurements derived from the images, and needs to be corrected. The false motion is corrected with image registration, which aligns the images to an image sequence through feature-based registration (Solem, 2012). Through feature-based registration, images are aligned by tracking ground control points (GCPs) or static feature points. Movements of the points are then used to calculate false motion. The false motion is calculated in the two-dimensional image plane, and then transformed into three-dimensional camera rotations, through information about the camera.

GCPs can be man-made targets or natural static features with known geographical positions. A minimum of four GCPs are needed to register images. Man-made GCPs are usually advantageous because they are designed to be easy to track. However, it can be difficult to acquire these in inaccessible places such as glacial environments, hence static features are more often used. The static features should be clearly visible features such as erratics, cliff edges or peaks (Addison, 2015).

Five man-made GCPs were positioned in the foreground of each of the North and South cameras at Store. However, they were positioned too close to the cameras and did not help with the image registration. Therefore, natural GCPs were defined from the background, using static features in the image plane. These steps were followed:

1. Download a DEM over the region, ArcticDEM was used (Porter et al., 2018), and use the hillshade function in QGIS to create a 3D visualization (Saephan, 2018)
2. Drape an overhead image (A Sentinel-2 image from 29 July 2018 was used, downloaded from https://earthexplorer.usgs.gov/) over the DEM using QGIS overlay blending mode
3. Open the 3D map view and position the map at the camera location. The exact same angle as the time-lapse camera was not possible, since it was situated on a tripod.
4. Spot out identifiable ground control points in the map view and a reference image (see figure 21 and figure 22). Write down the x and y from the reference image and the corresponding real-world coordinates (x,y,z) for the 3D map for each point. In figure 23 the camera locations and the manually defined GCPs are visible.

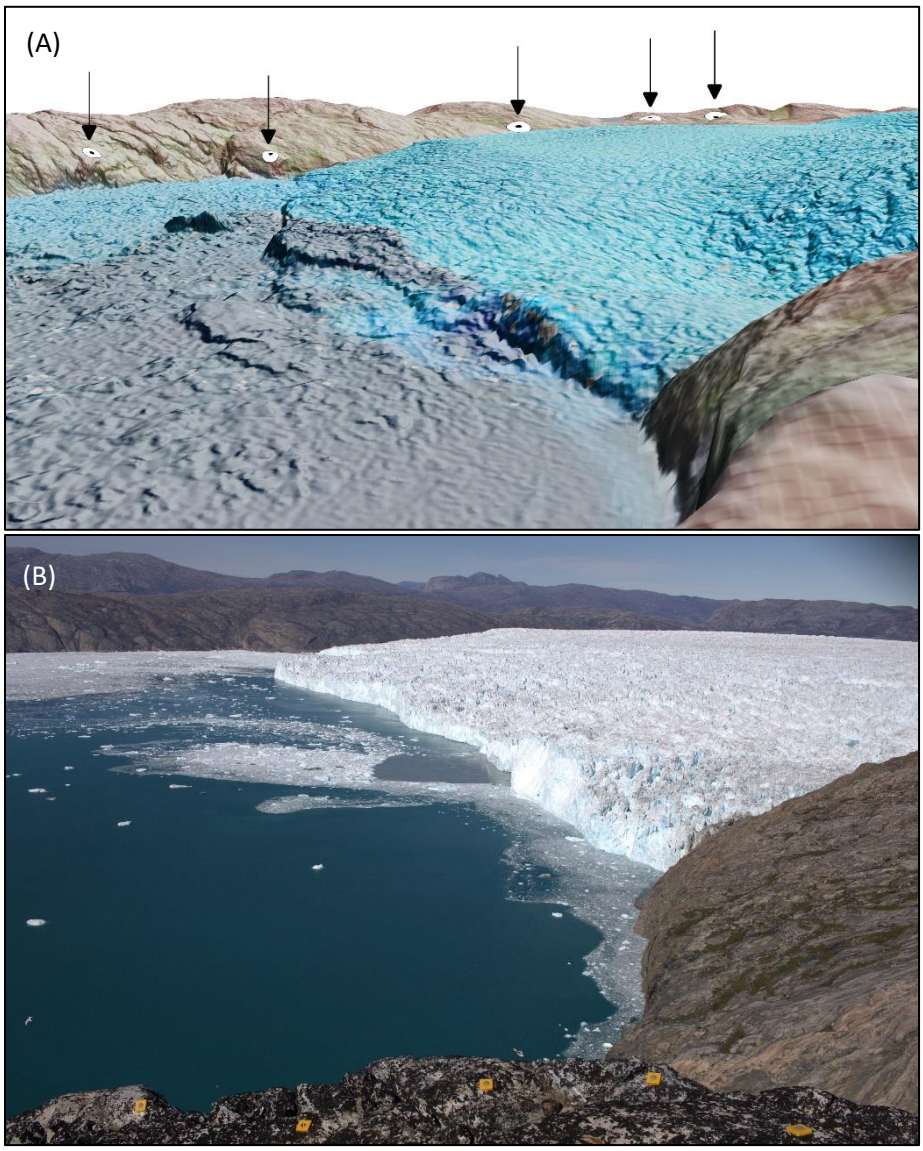

Figure 21. (A) Showing manually identified GCPs on a 3D visualisation of the South camera view using a DEM and a draped Sentinel-2 image from 29 July 2018. **(B)** The corresponding reference image taken with the South time-lapse camera 29 July 2018

Figure 22. (A) Showing the manually identified GCPs on a 3D visualisation of the North camera view using a DEM and a draped Sentinel-2 image from 29 July 2018. **(B)** The corresponding reference image taken with the North time-lapse camera 29 July 2018

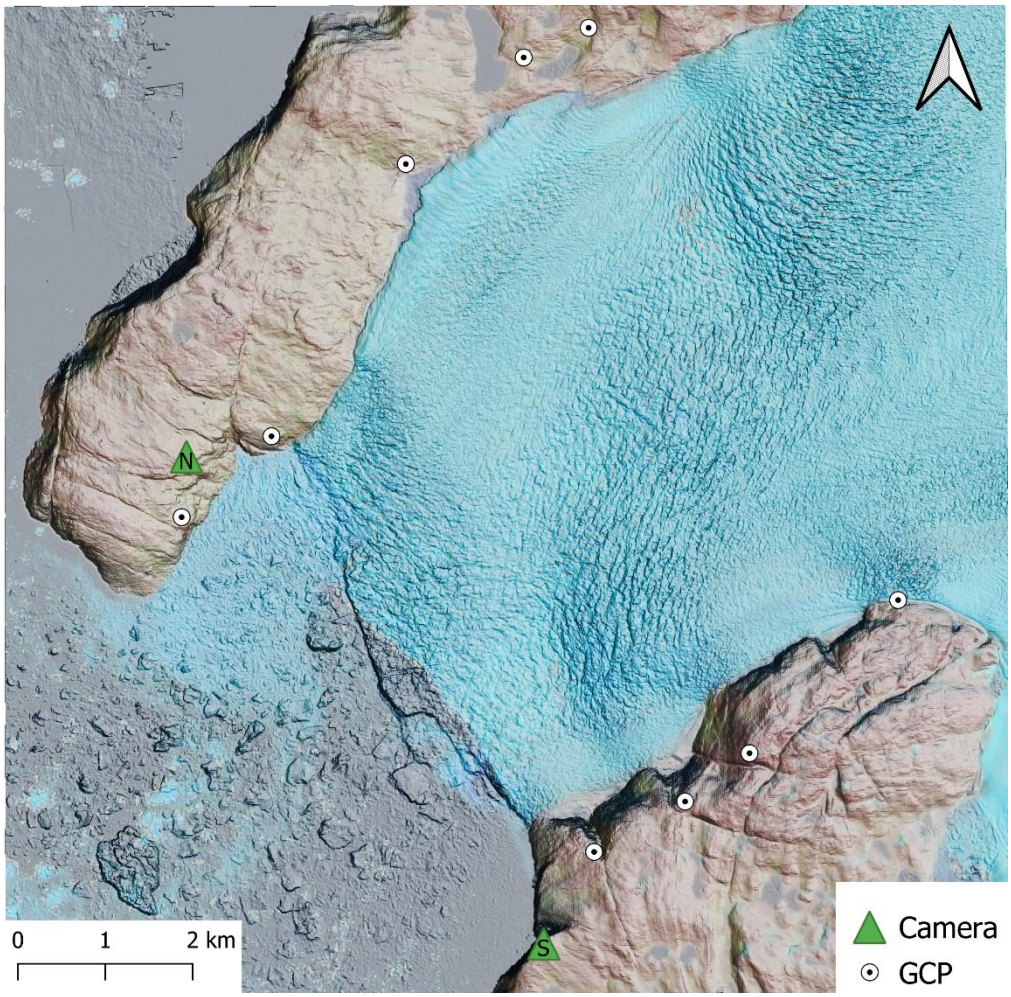

Figure 23. Map over Store glacier front showing positions of the North (N) and South (S) cameras and ground control points (GCPs). The base is a DEM from ArcticDEM (Porter et al., 2018), overlayed by a Sentinel-2 image taken 29 July 2018

Image registration was assessed using a reference image. An optimisation routine was performed in PyTrx, were the optimised pixel residual was an average difference between defined natural GCPs and the project GCPs. The optimised average pixel residual was 31 for the South images, and 45 for the Nouth images. A comparison between the residuals and real-world GCPs for the South camera can be seen in figure 24.

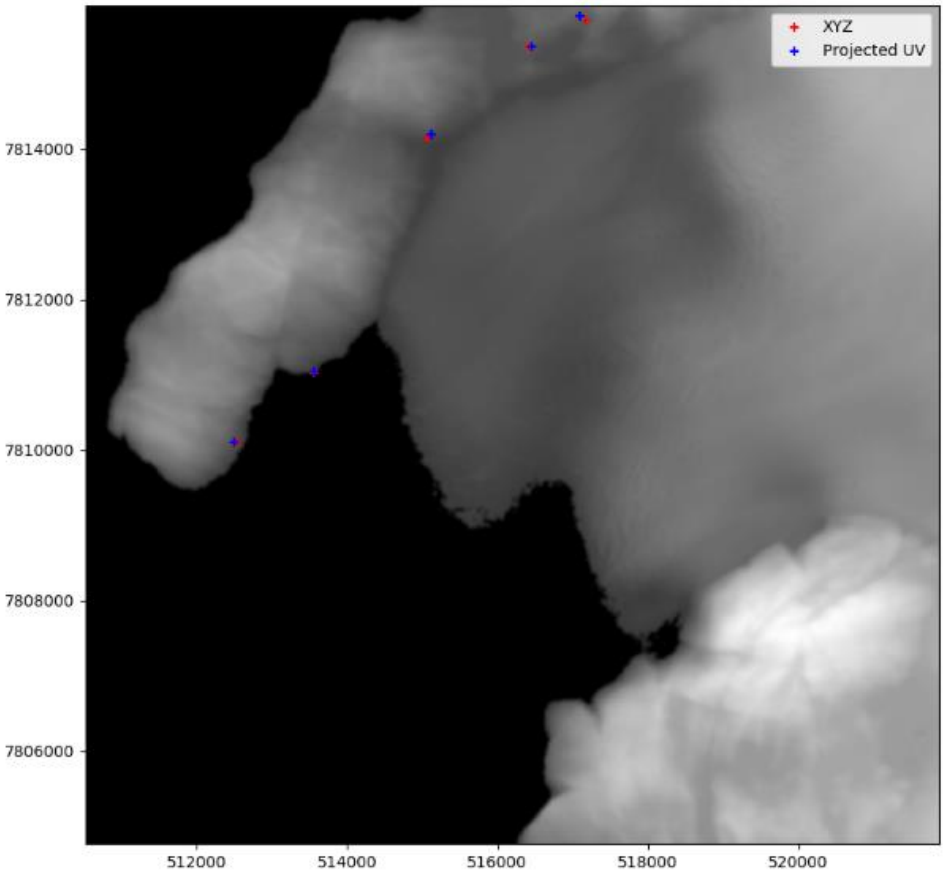

Figure 24. Pixel residuals (red cross) and real-world GCPs (blue cross) for the South camera. The base map is a modified DEM from ArcticDEM.

The translation to a three-dimensional space was achieved using a planar transformation model, which is typically used for time-lapse photogrammetry in glaciology (Busch, 2014). Planar projective transformations are used specifically for image registration and georectification. For image registration, the point pairs from the GCPs are used to map the destination image to the reference image. For georectification, the image is transformed from the image plane coordinate system to a real-world coordinate system in the homography model (Hartley and Zisserman, 2004). The homography (see figure 18) is calculated using GCPs, a digital elevation model (DEM) and Boolean image masks.

A DEM from ArcticDEM v.3 with 2m resolution was downloaded from the Polar Geospatial Centre (Porter et al., 2018). The ArcticDEM was clipped to the extent of Store Glacier front and fjord and reprojected to the coordinate system WGS 84/UTM zone 22N (EPSG:32622) in Google Earth Engine. It was then modified and manipulated in QGIS. First the DEM was flattened so that all low-lying elevations (below 150 m) were transformed to 0 m.a.s.l. This was to not project meltwater plumes onto the glacier front or ice melange. Second, the geoid

EGM2008 1' was downloaded from Agisoft (https://www.agisoft.com/downloads/geoids/), and subtracted from the DEM, to obtain the geoid elevation instead of the ellipsoid. Third, the DEM was smoothed using the Gaussian filter in QGIS, to avoid projecting image points on to a part of the DEM that had big steep changes. And finally, the DEM was downgraded to 20 meter resolution. The resulting DEM can be seen in figure 25.

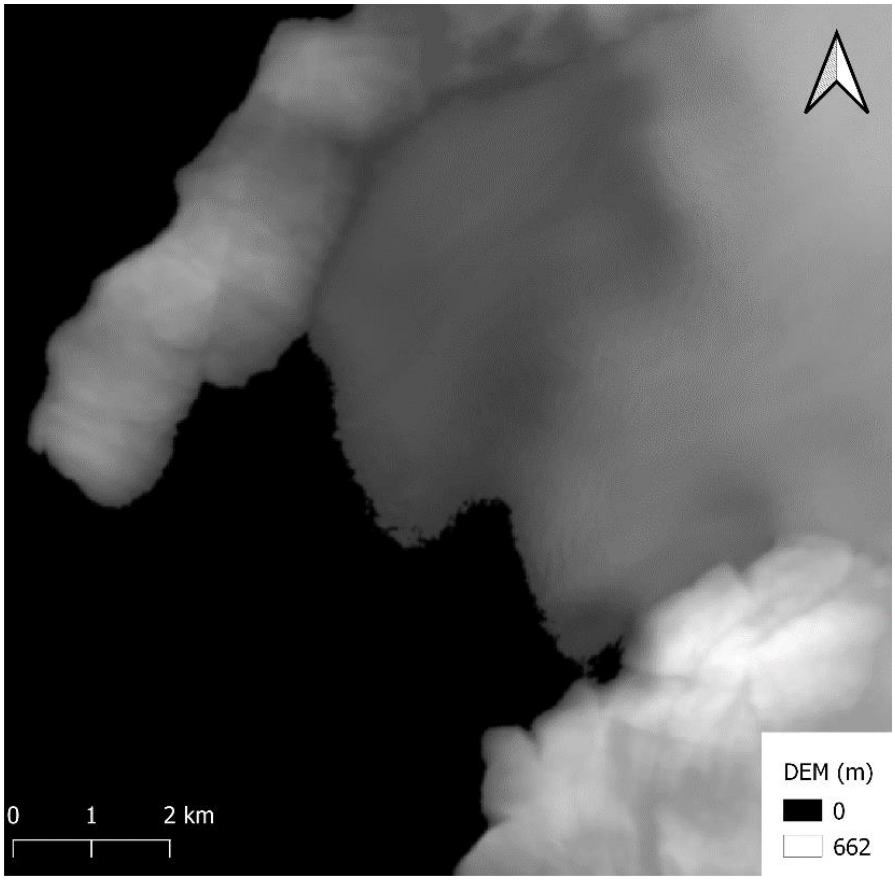

Figure 25. Digital Elevation Model of Store Glacier. Modified from ArcticDEM (Porter et al., 2018).

Boolean image masks were also needed for tracking static features and performing image registration. The Boolean image masks were drawn by marking roughly around the mountains in the background of the North and South images, see figure 26. They were used to co-register the images and eliminate artefacts in the measurements associated with motion in the camera platform, using offsets in the stable features to map the two image matrices and their relations to one another.

Figure 26. View of the creation of a Boolean image mask for the South camera by drawing around the stable features in the image scene.

3.2.4 Plotting plume surface extent

After setting up the homography, the plume surface extents were received through manually plotting around each plume, see figure 27. The surface appearance of a plume was usually easily identified by differences in water colour to a brown or red colour due to sediments, water roughness, and the area from which sea ice or icebergs had been cleared by divergent flow. Most of the plumes either had sediments in them or were ice plumes, i.e. semicircular shapes of open water originating from the front in the otherwise ice-covered fjord, and were easily identified. How to differentiate between a clear water plume and remnants from calving events when the fjord was ice free was a bit more tedious. After a calving event, changes in the glacier front could be seen together with visible icebergs and ripples in the water. The calving events were also most often over in less than 20 minutes. If no visible changes in the calving front or new icebergs appeared, and the shape stayed in several images one could therefore assume it was a clear water plume.

Later in the season the plumes became more difficult to identify. Most of the plume-like shapes in September were semicircular and moved away from the front, but disappeared in the next image (an hour later) and had no colour difference or presence of sediment in them. Therefore,

it is a possibility that some late-season plumes were mistaken for a calving event, and vice versa. It is also a small possibility that the last plume appearance appears later in the season than what was found in the results presented below.

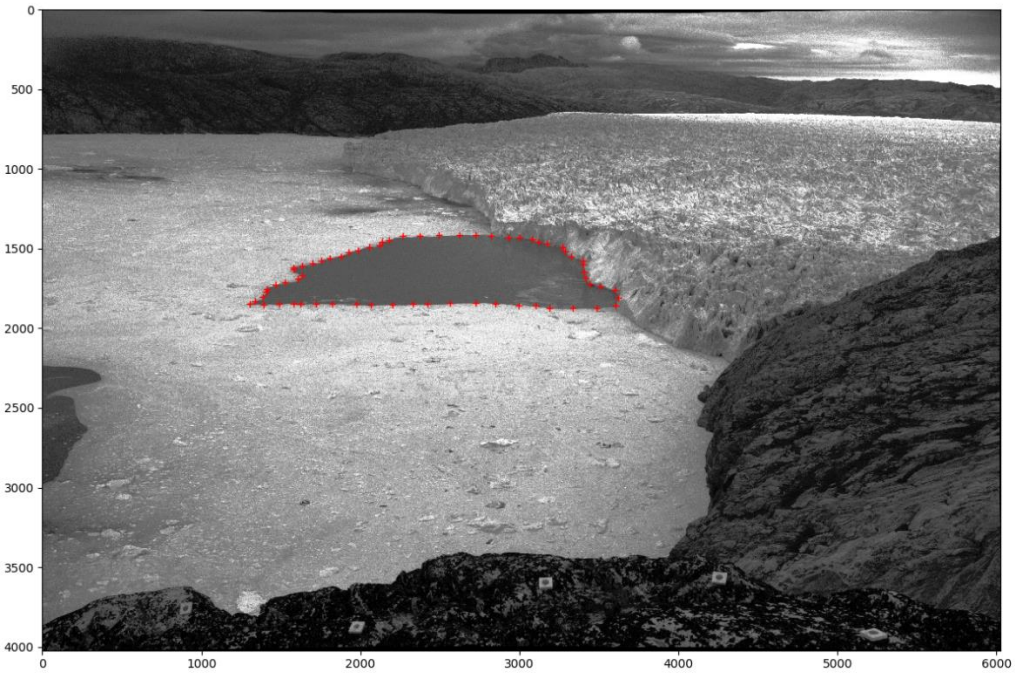

Figure 27. View of a manually plotted plume extent in PyTrx.

After marking around the plume surface extent, PyTrx calculated the real area of the plume and produced the plotted figure in RGB and B&W format, as well as a DEM and shapefile. Images that were too cloudy or dark to detect plume appearance were removed. The total plume area from both cameras was then calculated. Six different plume locations were identified, two from the North camera and four from the South camera. The shapefiles of the plotted plumes were added into QGIS to determine what plume location each plume belonged to.

3.3 Results

Surface meltwater was discharged sub-glacially from Store Glaciers outlet into the adjacent fjord, forming subsurface plumes that rose turbulently until they reached neutral buoyancy. Meltwater plumes can reach neutral buoyancy at any depth, depending on the rate of discharge, density gradient in the water, and the fjord geometry (Bartholomaus et al., 2016; Carroll et al., 2016; Schild et al., 2016; Stevens et al., 2016). However, only the plumes that reached the surface are included in this study, as the subsurface plumes were not possible to spot with the time-lapse imagery. Images obscured by cloud cover or darkness were not included.

The breakup of ice melange in the adjacent fjord to Store Glacier occurred in early to mid June, the melange was gone 7 June in the south section visible in the South camera, and 17 June in the north section visible in the North camera. Surface extents of meltwater plumes appeared from 20 June to 27 September. The Python Toolbox PyTrx (How et al., 2018) was used to manually define the surface extent and calculate the area of each plume.

The surface extent and area of 1706 plumes were defined and calculated, whereas 1536 plumes came from the South camera images and 170 plumes from the North camera images. The different locations of the plumes were distinguished, and six plume placements were identified throughout the season, four from the South camera and two from the North camera. Examples of the six plumes can be seen in figure 28, and the location of the six plumes can be seen in figure 29. The plumes moved slightly throughout the season, especially plume S4 and N2. The position of plume S4 was also where most of the large calving events were observed during the melting season of 2018.

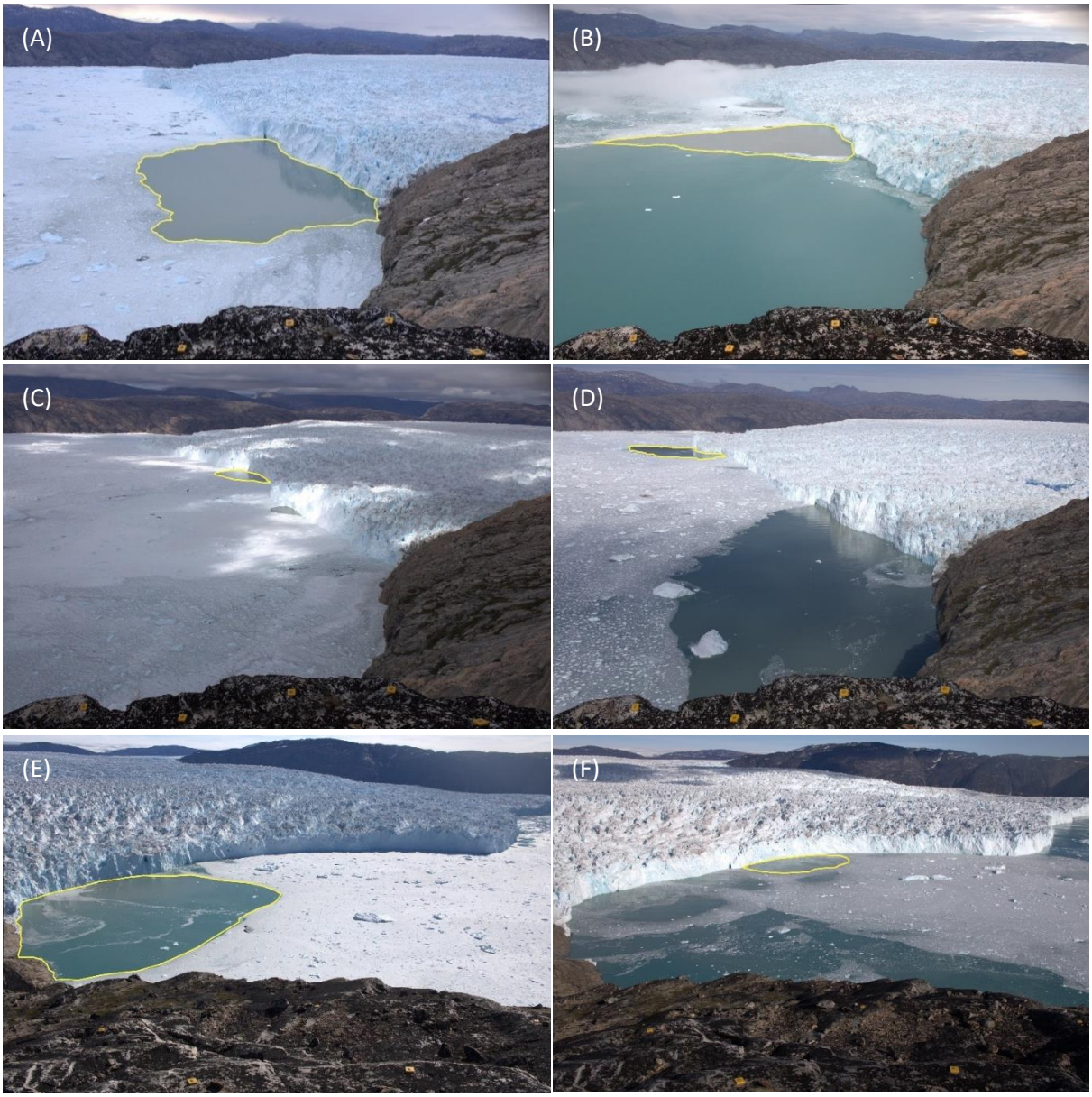

Figure 28. Photographs showing different plumes forming in front of Store Glacier in 2018. **(A)** South1 plume from 29 June 20:45, area 46,3884 m^2, **(B)** South2 plume from 27 July 22:45, area 389,533 m^2, **(C)** South3 plume from 20 July 13:45, area 73,495 m^2, **(D)** South4 plume from 30 June 11:45, area 233,688 m^2, **(E)** North1 plume from 31 July 11:05, area 310,179 m^2, and **(F)** North2 plume from 28 July 17:04, area 80,323 m^2.

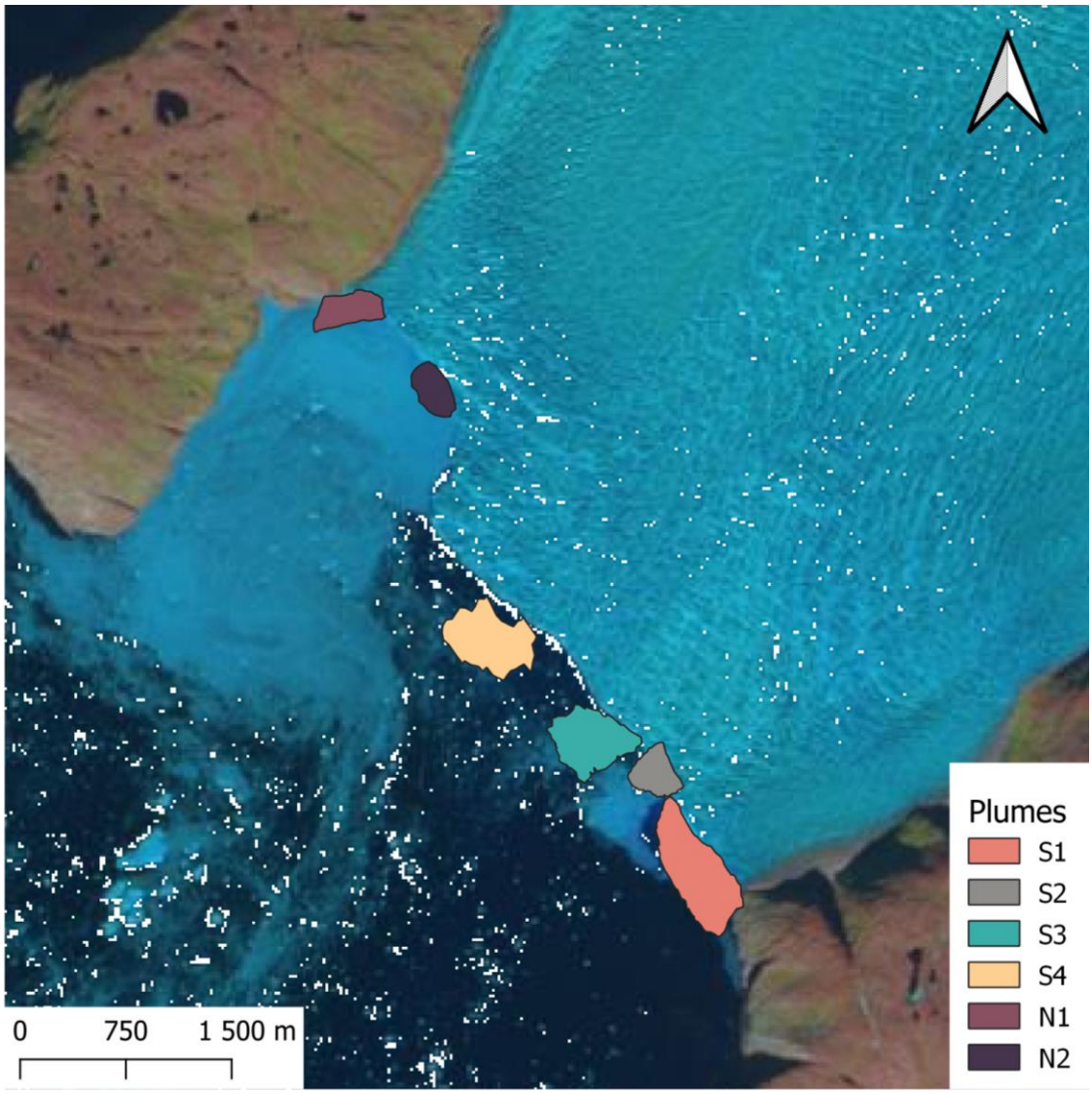

Figure 29. Map showing the location of plumes during 2018. The surface expressions for Plume S1 is taken from 29 June 2018 19:45, Plume S2 is taken from 16 July 12:45PM, Plume S3 is taken from 13 July 17:45, Plume S4 is taken from 30 June 11:45 a.m., Plume N1 is taken from 16 August 22:05 and Plume N2 is taken from 28 July 17:04. Notice that the plume sizes do not represent each plume's size during the entire season. The base map is a Sentinel-2 image from 29 July 2018 (from https://earthexplorer.usgs.gov/).

The total plume area during the melting season 2018 was calculated and visualised in figure 30. There were three major peaks in surface plume area. The first peak appeared in the end of June and reached the maximum area of 799,837 m^2. The second peak occurred 20-31 July and reached the maximum area of 1,003,068 m^2. The third and largest peak occurred in early to mid August and reached the maximum area of 2,279,157 m^2. After that short instances of plumes smaller than 500,000 m^2 appeared until the end of September.

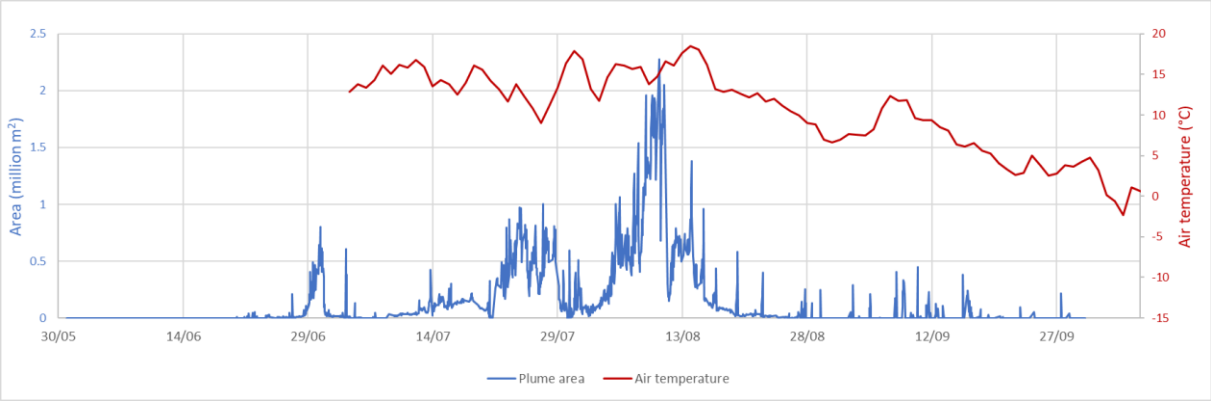

Figure 30. Time series graph of total surface plume area at the front of Store Glacier during the 2018 melting season (blue line) and air temperature (red line) from a meteorology station close to the glacier front.

Plume areas were sorted according to plume placement, and time series of the areas of the six plumes were created, see figure 31 (A). Plume N1 was active from 15 July 02:05 to 20 August 14:04, with maximum area of 819,482 m^2 (30 July). Plume N2 was active from 23 June 18:05 to 6 August 13:04, with maximum area of 480,082 m^2 (27 July). Plume S1 was active from 21 June 21:45 to 24 September 06:43, with maximum area of 942,111 m^2 (24 July). Plume S2 was active from 21 June 08:45 until 27 September 12:43 p.m., with maximum individual area of 1,003,068 m^2 (27 July). Plume S3 was active briefly from 26 June 19:45 to 30 June 07:45, and again from 13 July 14:45 until 14 August 03:44 a.m., with maximum individual area of 478,107 m^2 (7 August). Plume S4 was active from 20 June 11:45 a.m. until 13 September 07:43, with maximum individual area of 327,833 m^2 (10 September).

Plume S1 and S2 were the most prevalent plumes, and stayed active almost the entire melting season. In late July and early to mid-August, the plumes S2, S3 and S4 on occasion merged together, forming one giant plume. It was difficult to say which plume was active and which was not, and how much of the area was contributed by each plume. On these occasions, the plumes were therefore identified as plume S2+S3, plume S2+S3+S4, and plume S3+S4, depending on which plumes merged. See figure 31 (B) for a time-series graph of the merged areas. The largest merged plume area of 2,279,158 m^2 appeared 10 August.

Figure 31. (A) Time series graphs of the individual plume area (in million m^2) of North1, North2, South1, South2, South3, and South4 each day of the 2018 melting season. **(B)** Time series of the occasions when plumes merged together, showing merged plume area (in million m^2) of South2 and South3 (pink), South2, South3 and South4 (blue), and South3 and South4 (green). Note that the y-axis max value is different in this graph.

3.4 Discussion

Surface meltwater that is discharged sub-glacially from outlet glaciers form buoyant plumes that rise turbulently until they reach neutral buoyancy (Motyka et al., 2003). The surface expression of meltwater plumes is identified based on a combination of fjord water roughness, appearance of sediments giving the water a brown-red colour, and the area from which icebergs and melange have been cleared away by divergent flow (Darlington, 2015). The importance of analysing the surface plume extent is two-fold. Firstly, as plumes rise, they entrain ambient fjord water and enhance undercutting and submarine melting, leading to increased calving (Carroll et al., 2015; Fried et al., 2015; Jenkins, 2011; Jouvet et al., 2018; Slater et al., 2015; Xu et al., 2012). Hence, by analysing appearance and size of plumes more information surrounding submarine melting and calving rates can be established. Secondly, vital information about the glacier's rate of discharge and subglacial drainage system can be found by analysing the plume surface expressions (e.g. Bartholomaus et al., 2016; Fried et al., 2015; Schild et al., 2016).

Plumes have been observed from satellite imagery (e.g. Bartholomaus et al., 2016; Darlington, 2015) and time-lapse imagery (e.g. Schild et al., 2016; Slater et al., 2017). However, there are not many measurements of the size, number and locations of plume-related channels (Fried et al., 2015). Moreover, a lack in high temporal frequency of images have previously made it difficult to track the, often rapid, change in plume appearance. It is therefore possible that plumes are more rapidly changing than what was previously thought (How, 2018).

In order to obtain high-temporal frequency of images, time-lapse images captured hourly were used in this study. Photogrammetry methods were performed in the Python toolbox PyTrx (How et al., 2018) to receive area, number and location of plume surface extents throughout the melting season of 2018. 1706 surface plumes appeared throughout the season, at six different locations along the front.

Through analysing the combined surface area of the plumes (figure 30), three peaks were visible; the smallest peak during 28-30 June, the middle peak occurred during 20-31 July and the largest peak appeared during 2-19 August. The results indicate a large influx of discharge to the fjord during these dates. After the larger events small plumes appeared for short periods semi-regularly until the end of September.

Variability in subsurface discharge channels affect the location and size of meltwater plumes. If meltwater plumes are distributed along the front of the glacier, that indicates well-distributed discharge across the glacier front. If the meltwater plumes are instead spatially focused, it could be an indicator of a locally dominant subglacial meltwater channels (Slater et al., 2015; Moyer et al., 2017). However, the fjord circulation and fjord geometry should also be considered, as it can impact the distribution of surface meltwater (Cottier et al., 2010, Straneo and Cenedese, 2015).

Through analysis of each individual plume appearance during the season, the location and activity of different subglacial meltwater channels can be identified. Plume S1 and S2 were the two most prevalent plumes, both active for almost the entirety of the melting season, indicating two dominant subglacial meltwater channels. Plume S1 reached peak area of 942,111 m^2 the 24 July, while S2 appeared in its largest individual form of 1,003,068 m^2 the 27 July. The two plumes appeared at similar time periods throughout the season, indicating that the meltwater channels providing the two plumes with water were connected. As S2 merged with S3 and S4 in beginning and mid August, the largest combined area was more than twice as large, 2,279,158 m^2, as S2's individual maximum area.

Plume S3 appeared briefly on 26 June and then remained active 13 July to 14 August. The individual surface area of S3 did not reach the same size as plume S1 and S2, and the maximum area of 478,107 m^2 was reached the 7 August. The shorter active time period and smaller plume areas indicate that the subglacial channel providing S3 with meltwater was only active during the middle part of the melting season. Plume S4 appeared in small form early in the season, from 20 to 22 of June, and then sporadically between 29 June and 27 July. It reappeared briefly during 10 to 17 of September and reached its maximum individual area of 327,833 m^2 the 10 September. The sporadic appearance of S4 indicate that the subglacial channel providing the plume with discharge was not active for most parts of the season. The smaller sizes of plumes S3 and S4 relative to S1 and S2 indicate two rather inefficient subglacial drainage channels providing the plumes with meltwater.

Plume N1 was active from 15 July to 6 August, appeared again briefly the 14 and 20 of August, and had a maximum area of 819,482 m^2 reached 30 of July. N1 activated the latest in the season of all plumes, indicating that the channel providing the plume with discharge only reached efficiency in mid July. Plume N2 was active from 23 to 29 June and then again from 11 July to

6 August, and had a maximum value of 480,082 m^2 reached 27 July. The surface extents of S2, S3 and S4 merged in early to mid August, disabling any individual analysis of the plume appearances. However, the plumes together reached maximum surface area during this time period, of 2,279,158 m^2 10 August, indicating a large flux of discharge from the subglacial drainage system.

The plume placements in this study were slightly different than the two time periods in Cook et al. (2020)'s study, in which the authors observed plume and calving activity at Store Glacier in 2012 and 2017 by coupling a subglacial hydrology model with a plume model. The authors found that plume appearance differed distinctly between both seasons and years. In the summer 2012, surface plumes appeared along the entire calving front, except for the most southern part of the front. Conversely, in the summer 2017 the authors found that the plumes were more spatially restricted and appeared in two regions; one in the north part of the front and one around the deepest part of the calving front. The authors proposed that variability in plume activity was partly related to surface-meltwater production, and partly due to the structure of the subglacial drainage system and related water storage. The surface plumes observed in this study for 2018 were more closely related to the 2012 plumes, indicating a more similar meltwater production and subglacial hydrology to that year than to 2017.

Moreover, Cook et al. (2020) noted that the locations of summer plumes vary throughout the summer season, as point of discharge from the hydrological system evolves. This is consistent with the results in this study, as the plumes tended to move along the calving front of Store Glacier throughout the season. This was especially the case for plume S4 and N2.

3.5 Conclusions

Recent studies have successfully linked tidewater glaciers' rate of discharge and evolution of subglacial drainage system to plume surface expressions. The aim of this chapter was to quantify the surface areas of plumes forming from subglacial discharge at the terminus of Store Glacier during the 2018 melting season.

The surface area of 1706 plumes at six different locations along Store Glacier's termini was calculated using time-lapse photogrammetry. The plume locations were spread out, with four plumes along the southern part of the termini, and two plumes along the northern part. The plume locations were similar to the modelled plumes at Store Glacier during summer 2012 in a

study by Cook et al. (2020). The plumes differed in size, with peak plume areas ranging from 327,833 m^2 (S4 plume) to 1,003,068 m^2 (S2 plume). Three large peaks in plume area were visible throughout the season, indicating periods of large freshwater discharge, the smallest peak during 28-30 June, the middle peak occurred during 20-31 July and the largest plume appeared during 2-19 August. Total peak area of 2,279,157 m^2 occurred 10 August, and were the combined area of S2, S3 and S4. The plumes moved slightly throughout the season as the point of discharge from the hydrological system evolved, consistent with Cook et al. (2020)'s results.

4. Chapter 3: Discussion

4.1 Key Findings

Previous studies have found indications of a largely inefficient subglacial drainage system in the upper part of Store Glacier, and a channelized system developing closer to the front during summer melting season. Doyle et al. (2018) found high basal water pressure of >90% of the overburden ice pressure 30 km inland from the front, indicating an inefficient basal water system there. Young et al. (2019) found surface velocities 30 km inland of the glacier to gradually increase throughout the melting season, indicating a relatively stable inefficient drainage system there. The authors also found that the lower part of the glacier, with surface elevations <1000 m, experienced seasonal variations in ice flow, consistent with the development of an efficient basal drainage system in late summer, and a channelized subglacial drainage system closer to the front. A subglacial hydrology model by Cook et al. (2020) showed an active subglacial drainage system with significant channelization up to 55 km inland from the front in summer, with an active distributed sheet extending another 10 km inland.

High temporal and spatial dual-satellite analysis through the FASTER algorithm (Williamson et al., 2018a) provided 54 individual lake volume estimates on Store Glacier during the 2018 melting season. Total lake volume increased from the end of May, reaching peak volume of 18.8 million m^3 on 19 July, before draining or freezing over until mid September. Lakes below 500-meter elevation started draining earlier in the season, median date 16 June, while lakes between 500-1000 m elevation drained later in June, median date 27 June. Lakes >1000 m elevation drained later in the season, median date 30 July. Lakes at elevations <1000 m were located ~9-36 km from the glacier front, while lakes at elevations >1000 m were located ~30-51 km from the glacier front. The results imply that lakes at lower elevations provide the subglacial drainage system at <1000 m elevations with drainage through most of the melting season, while lakes at >1000 m elevations only drain later in the season, providing the subglacial drainage system there with infrequent influx of water. These results support recent studies in the theory of an inefficient drainage system further inland where ice is thicker, and the development of an efficient subglacial drainage system during the summer melting season closer to the front, at elevations of <1000 meters. No lakes were located further than 51 km from the glacier termini. The three lakes which froze over instead of drained were located at 51 km, 42 km and 27 km distance from the front, respectively. The lake furthest from the glacier termini that experienced drainage was located ~45 km from the glacier front. These results

indicate that the subglacial drainage system >45 km inland from the glacier termini did not experience any lake drainage events. This is partly in line with recent studies showing an active subglacial drainage system with significant channelization up to 55 km inland from the front in summer.

At which depth meltwater plumes reach neutral buoyancy depends on the rate of discharge, the density gradient, and the fjord geometry (Bartholomaus et al., 2016; Carroll et al., 2016; Schild et al., 2016; Stevens et al., 2016). Changes in plume surface expressions over time have been used to analyse both discharge rate and the subglacial drainage system providing the plume with freshwater (e.g. Bartholomaus et al., 2016; Fried et al., 2015; Schild et al., 2016). Appearance and size of plumes along different parts of the glacier front can also be used as an indicator of spatial variability in discharge. Where spatially distributed plumes are an indicator of well-distributed discharge across the glacier front, and on the contrary, spatially focused plumes indicate locally dominant subglacial channels (Moyer et al., 2017; Slater et al., 2015). Cook et al. (2020) modelled subglacial hydrology and plume formation at Store Glacier, and found that during summer 2012 plumes were strong and channel-led along the majority of the front, while in summer 2017, plumes were more spatially restricted, indicating locally dominant subglacial channels.

In this study, the surface extent and area of meltwater plumes at the termini of Store Glacier during the 2018 melting season were identified and calculated using time-lapse photogrammetry in the Python toolbox PyTrx (How et al., 2018). 1706 plumes were identified throughout the season, from 20 June to 27 September. Plumes appeared at six different locations along the front. The plumes moved slightly throughout the season, especially plume S4 and N2. The two most prevalent plumes S1 and S2 appeared active almost the entire melting season, with surface extents visible from 21 June to 27 September. Plume S3 appeared active in the middle of the melting season, approximately from mid July to mid August, while S4 appeared sporadically from 20 June to 10 August, and then again 10-17 September. Plume N1 was active in the middle of the melting season, from mid July to early August, and N2 was active from 23 to 29 June and then again from 11 July to 6 August. Fjord geometry could have an effect on where surface plumes appeared. However, the results indicate two locally dominant subglacial channels providing S1 and S2 with freshwater almost throughout the entire season, and spatially distributed and sporadic appearances of plumes along the rest of the termini are an indicator of well-distributed intermittent discharge across the rest of the glacier front.

4.2 Combined Analysis of Supraglacial lakes and Meltwater plumes

Chu et al. (2009) performed a satellite observation of a 66,000 m^2 area on the West Greenland ice-sheet, to study plume appearance. The authors confirmed that the origin of the plumes was meltwater from the ice sheet. Moreover, the authors determined that plumes appeared almost directly after the onset of surface melting, and concluded rapid coupling between the ice sheet and the subglacial discharge. The authors also looked at plume appearance following supraglacial lake events, with only 38% of lake drainage events triggering an increase in plume area. Schild et al. (2016) used time-lapse imagery and satellite imagery to identify and compare plume appearance with lake drainage events, but found no temporal correspondence between drainage and plume appearance. This led the authors to suggest that lake drainages were not the primary driver of plumes, likely due to an inefficient drainage system.

In this study, early in the melting season (31 May to 17 June) neither drainage nor meltwater plumes was observed. From 17-18 June there was an increase in total discharge of 0.46 million $m^3\ d^{-1}$. The 2 July a second peak in discharge of 1.1 million $m^3\ d^{-1}$ was visible. A slightly smaller peak in discharge occurred around the 8 July, of 0.71 million $m^3\ d^{-1}$, and then again of 0.86 $m^3\ d^{-1}$ on 20 July. The largest discharge of the season of 1.6 $m^3\ d^{-1}$ was observed on 31 July. After that there was another large peak in discharge on 23 August (1.1 million $m^3\ d^{-1}$). However, since the lakes that appeared to drain in mid-August in fact froze over, the last peak in discharge was overlooked.

The first peak in plume area occurred the 30 June, of 0.8 million m^2. Another peak in plume area of 0.6 million m^2 was observed 3 July. Plume appearance was constant from 8 July, with a large increase around the 20 July, reaching peak area of 1.0 million m^2 the 27 July. Around 2 August there was a major drop in plume appearance before a large increase around 4 August, reaching the largest plume area of the season; 2.2 million m^2 10 August. This is followed by a number of smaller (around 0.25 million m^2) plumes that appear until end of September.

By analysing the appearance and area of plumes together with the estimated total lake drainage (see figure 32), a few trends were clear. Early in the season, the first peak in drainage occurred 12 days before the first peak in plume area, on 18 and 30 June, respectively. In July, drainage events were observed the 2nd, 8th and 21st, while peaks in plume area occurred on 3 July and 13 July, followed by a larger peak in plume area the 27 July. The largest peak in drainage, on 31 July, occurred 10 days before the largest peak in plume area of the season, on 10 August.

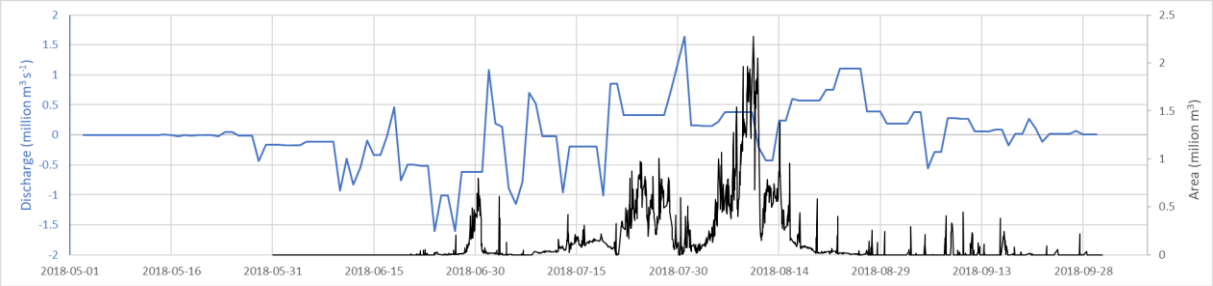

Figure 32. Time series graph showing discharge from lake drainage (blue line) and total area of surface plumes (black line) during the melting season 2018.

The trends of plume areas and discharge events could be related to the evolution of the subglacial drainage system. During the beginning of the melting season, one period of large plume appearances was observed from 28 June to 1 July. It could be linked to a drainage event occurring 17-18 June, resulting in a time lag of 11 days between drainage and plume appearance. The lakes providing most of the discharge during 17 July were lake 1 (23,256 m^3 d^{-1}), lake 2 (85,363 m^3 d^{-1}), lake 5 (29,803 m^3 d^{-1}), lake 10 (30,914 m^3 d^{-1}), lake 15 (26,952 m^3 d^{-1}), lake 20 (147,778 m^3 d^{-1}) and lake 22 (52,250 m^3 d^{-1}). Additionally, the lakes providing most of the discharge 18 July were lake 2 (26,291 m^3 d^{-1}), lake 17 (39,896 m^3 d^{-1}), lake 21 (618,788 m^3 d^{-1}) and lake 22 (46,390 m^3 d^{-1}). Lake 21, positioned at 630 m elevation and ~21 km from the glacier front, provided the most discharge of all lakes. The time lag between drainage and plume appearance could be due to the fact that early in the melting season, the subglacial drainage system had not reached efficiency yet and the drained water ended up in cavities and disconnected drainage channels, until sufficient amounts of water connected the channels and the drainage system reached efficiency.

Two discharge events that occurred the 2 and 8 July were followed by small and relatively short-lived increases in plume area in front of the glacier. For 2 July, the lakes providing most of the discharge were lake 13 (77,870 m^3 d^{-1}), lake 19 (632,138 m^3 d^{-1}), lake 31 (73,062 m^3 d^{-1}), lake 33 (73,124 m^3 d^{-1}), lake 38 (52,079 m^3 d^{-1}), and lake 50 (33,743 m^3 d^{-1}). I.e. most of the discharge came from lake 19, located at 440 m elevation and ~16 km from the glacier front. Considering the low elevation and relatively close proximity of lake 19 to the front, it is likely that the plume appearance the 3 July was largely due to discharge from this specific lake.

For the 8 July, the lakes providing most of the discharge were lake 5 (82,292 m^3 d^{-1}), lake 16 (28,264 m^3 d^{-1}) and lake 33 (243,422 m^3 d^{-1}). I.e. most of the discharge came from lake 33, at 1070 m elevation and ~34 km from the glacier front. A possible explanation for the inconsistent relationship between plume appearance and the drainage event on 8 July were that most of the discharge came from a high elevation lake positioned 34 km inland of the front, draining into a inefficient drainage system.

Two drainage events occurred the 20-21 and 31 of July. The lakes providing most of the discharge 20-21 July were lake 24 (41,014 m^3 d^{-1}), lake 27 (24,048 m^3 d^{-1}) and lake 43 (47,486 m^3 d^{-1}). Lake 24 was positioned at 870 m elevation, ~28 km from the glacier front, and lake 43 was positioned at 850 m elevation, ~27 km from the glacier front, meaning most of the drained water had to travel ~28 km before reaching the glacier front. The lakes providing most of the discharge 31 July were lake 21 (1,647,853 m^3 d^{-1}), lake 24 (291,656 m^3 d^{-1}), lake 32 (159,821 m^3 d^{-1}), lake 33 (284,992 m^3 d^{-1}), lake 36 (266,269 m^3 d^{-1}), and lake 44 (207,583 m^3 d^{-1}). Most of the discharge came from lake 21, at 630 m elevation and ~21 km from the glacier front, meaning the water had to travel 21 km before reaching the glacier front. The two drainage events could be linked with two long periods of large plume appearances between 21 and 31 of July, and 4 to 14 August, the second including the largest plume appearance of the season. If that was the case, the time lag of the drainage system was 1 and 4 days, respectively. This would imply that the subglacial drainage system at elevations <1000 m had reached high efficiency at that point, rapidly delivering meltwater from the lake drainages to the front of the glacier.

These results indicate that in early June during the melting season of 2018, the subglacial drainage system at Store Glacier was distributed and inefficient, and drainage of supraglacial lakes lead to increased subglacial storage in cavities and disconnected channels. By early July, the drainage system at <1000 m elevation had developed into an efficient system, with fast hydraulic transmissivity, while elevations >1000 m still experienced slow hydraulic transmissivity in a distributed drainage system.

4.3 Limitations and Future Research

Supraglacial lakes only contain a fraction of the total meltwater produced at the surface; therefore, one cannot rule out the possibility that surface meltwater not captured in lakes contribute to the plumes forming at the front. However, supraglacial lakes produce observable and rapid injections of water to the subglacial drainage system, which is the why they were focused on in this study. Moreover, the FASTER algorithm underestimated lake volumes by approximately half, evident from comparisons with field-based measurements from lake 42.

The time-lapse photogrammetry method for calculating plume areas had a few limitations, such as limited visibility due to cloud coverage and darkness. However, no significant time periods of data were lost during the melting season of 2018, due to few periods of darkness during summer season, together with limited cloud cover. Another limitation concerning the stationary time-lapse cameras were the fact that plume S3 and S4 were far away from the camera and therefore certain details in their plume extents might have been missed. The chessboard images used in order to compute camera calibrations were not taken from the same distance and did not show the entire chessboard in each image. This affected the output of the camera calibrations negatively. However, the camera calibrations were corrected in PyTrx's camera optimisation routine.

From this study we can obtain a basic understanding of the connection between supraglacial lakes and meltwater plumes in relation to the subglacial hydrology of tidewater glaciers. Only a few previous studies have observed this connection. This research shows the importance of high-detail observations for a deeper understanding of the unique subglacial drainage systems of tidewater glaciers. Future studies should focus on further developing our understanding of the evolution of and connection between supraglacial lake drainage and meltwater plumes, in order to understand the implications of climate change on tidewater glacier's subglacial hydrology, which in turn will have a large affect on the Greenland ice sheet mass balance.

5. Chapter 4: Conclusions

The subglacial hydrology of tidewater glaciers has previously been difficult to observe, due to difficulty in obtaining direct measurements. In this study I was able to obtain high detail data of supraglacial lakes and meltwater plumes, two key variables of the subglacial hydrology of tidewater glaciers. The surface area of the 1706 plumes observed in front of the Store Glacier termini during the 2018 melting season was calculated, and volume loss and drainage of 54 lakes were obtained for the same time period.

The plume surface extents appeared from 20 June to 27 September. Two prominent plumes in the southern extremity of the glacier terminus appeared through this entire period, while two plumes located further to the middle of the terminus appeared intermittently throughout the season, mostly in the beginning and middle of the melting season. Two plumes were also observed in the northern part of the terminus, and appeared sporadically during the middle of the melting season. Fjord geometry could have an effect on where surface plumes appeared, and has not been taken into consideration in this study. However, the results from this study indicate two locally dominant subglacial channels providing the two plumes in the southern part of the terminus with freshwater almost throughout the entire season, and the spatially distributed and intermittent plumes along the rest of the termini are an indicator of well-distributed discharge across the rest of the glacier front.

The 54 supraglacial lakes differed largely in size, with peak volumes ranging from 29,000 m^3 to 4,486,000 m^3. Total peak volume of 18.8 million m^3 occurred 19 July. Approximately 5% of the lakes experienced rapid lake drainage. Lakes at lower elevations (<1000 m) experienced draining earlier in the season than lakes at higher (>1000 m) elevations. These results imply that lakes provide the subglacial drainage system at <1000 m elevations with drainage through most of the melting season, while lakes at >1000 m elevations only drain later in the season, providing the subglacial drainage system there with an infrequent influx of water. No lakes were observed to drain further than 45 km inland of the glacier front, indicating that the subglacial drainage system further inland did not experience any influx of water from lake drainage.

Combined analysis of supraglacial lakes drainage events and large areas of meltwater plumes were performed. Supraglacial lakes only contain a fraction of the total meltwater produced at

the surface, and surface meltwater not captured in lakes could therefore also contribute to plume formations at the front. This should be taken into consideration. However, supraglacial lakes provide observable and rapid injections of water to the basal environment, hence why they were focused on in this study. The elevation and distance to the front of large lake drainages were analysed and compared with the appearance of large plumes. In late June, a time lag of 11 days was observed between supraglacial lake drainage and plume appearance. From early July, <1000 m elevation, subglacial drainage systems transported water efficiently, and plumes were observed shortly after drainage events at these elevations. However, drainage of lakes >1000 m was not clearly visible in plume observations. These results indicate that in June the entire subglacial drainage system at Store Glacier was distributed and inefficient, and drainage of supraglacial lakes lead to increased subglacial storage in cavities and disconnected channels. However, by early July the drainage system at <1000 m elevation had developed into an efficient system, with fast hydraulic transmissivity, while elevations >1000 m still experienced slow hydraulic transmissivity and a distributed drainage system.

References

Addison, L. (2015). PyTrx: feature tracking softward for automated production of glacier velocity. MSc thesis, University of Edinburgh

Ahn, Y., & Box, J. E. (2010). Glacier velocities from time-lapse photos: Technique development and first results from the Extreme Ice Survey (EIS) in Greenland. *Journal of Glaciology, 56*(198), 723-734. doi:10.3189/002214310793146313

Amos, J. (2019, June 17). 'Cryoegg' to explore under Greenland Ice Sheet. Retrieved July 20, 2020, from https://www.bbc.com/news/science-environment-48638958

Andrews, L. C., Catania, G. A., Hoffman, M. J., Gulley, J. D., Lüthi, M. P., Ryser, C., . . . Neumann, T. A. (2014). Direct observations of evolving subglacial drainage beneath the Greenland Ice Sheet. *Nature, 514*(7520), 80-83. doi:10.1038/nature13796

Andrews, L. C., Hoffman, M. J., Neumann, T. A., Catania, G. A., Lüthi, M. P., Hawley, R. L., . . . Morriss, B. F. (2018). Seasonal Evolution of the Subglacial Hydrologic System Modified by Supraglacial Lake Drainage in Western Greenland. *Journal of Geophysical Research: Earth Surface, 123*(6), 1479-1496. doi:10.1029/2017jf004585

Arnold, N. S., Banwell, A. F., & Willis, I. C. (2014). High-resolution modelling of the seasonal evolution of surface water storage on the Greenland Ice Sheet. *The Cryosphere, 8*(4), 1149-1160. doi:10.5194/tc-8-1149-2014

Banwell, A. F., Caballero, M., Arnold, N. S., Glasser, N. F., Cathles, L. M., & Macayeal, D. R. (2014). Supraglacial lakes on the Larsen B ice shelf, Antarctica, and at Paakitsoq, West Greenland: A comparative study. *Annals of Glaciology, 55*(66), 1-8. doi:10.3189/2014aog66a049

Banwell, A., Hewitt, I., Willis, I., & Arnold, N. (2016). Moulin density controls drainage development beneath the Greenland ice sheet. *Journal of Geophysical Research: Earth Surface, 121*(12), 2248-2269. doi:10.1002/2015jf003801

Bartholomaus, T. C., Anderson, R. S., & Anderson, S. P. (2007). Response of glacier basal motion to transient water storage. *Nature Geoscience, 1*(1), 33-37. doi:10.1038/ngeo.2007.52

Bartholomaus, T.C., Stearns, L.A., Sutherland, D.A., Shroyer, E.L., Nash, J.D., Walker, R.T., Catania, G., Felikson, D., Carroll, D., Fried, M.J., Nol, B.P.Y. and Broeke, M.R.V.D. (2016). Contrasts in the response of adjacent fjords and glaciers to ice-sheet surface melt in West Greenland. Annals of Glaciology, 57, 25–38.

Bartholomew, I., Nienow, P., Mair, D., Hubbard, A., King, M. A., & Sole, A. (2010). Seasonal evolution of subglacial drainage and acceleration in a Greenland outlet glacier. *Nature Geoscience, 3*(6), 408-411. doi:10.1038/ngeo863

Bartholomew, I., Nienow, P., Sole, A., Mair, D., Cowton, T., King, M., & Palmer, S. (2011). Seasonal variations in Greenland Ice Sheet motion: Inland extent and behaviour at higher elevations. *Earth and Planetary Science Letters, 307*(3-4), 271-278. doi:10.1016/j.epsl.2011.04.014

Bougamont, M. (2018). Modeled water routing data. Available at UK Polar Data Center, https://doi.org/10.5285/481D4120-1A72-468B-8CD4-84B4E14CDEAB. [Accessed: 2020-04-07]

Box, J. E., & Ski, K. (2007). Remote sounding of Greenland supraglacial melt lakes: Implications for subglacial hydraulics. *Journal of Glaciology, 53*(181), 257-265. doi:10.3189/172756507782202883

Busch, D.D. (2014). Digital SLR Cameras and Photography For Dummies, 5th edn. John Wiley & Sons, Hoboken, New Jersey, 352 pp.

Carrivick, J., Smith, M., & Quincey, D. (2016). *Structure from motion in the geosciences*. Chichester, West Sussex, UK: John Wiley & Sons, Inc.

Carroll, D., Sutherland, D.A., Hudson, B., Moon, T., Catania, G.A., Shroyer, E.L., Nash, J.D., Bartholomaus, T.C., Felikson, D., Stearns, L.A., No¨el, B.P.Y. and van den Broeke, M.R. (2016). The impact of glacier geometry on meltwater plume structure and submarine melt in Greenland fjords. Geophysical Research Letters, 43, 2016GL070170.

Carroll, D., Sutherland, D. A., Shroyer, E. L., Nash, J. D., Catania, G. A., & Stearns, L. A. (2015). Modeling Turbulent Subglacial Meltwater Plumes: Implications for Fjord-Scale Buoyancy-Driven Circulation. *Journal of Physical Oceanography, 45*(8), 2169-2185. doi:10.1175/jpo-d-15-0033.1

Catania, G. A., & Neumann, T. A. (2010). Persistent englacial drainage features in the Greenland Ice Sheet. *Geophysical Research Letters, 37*(2). doi:10.1029/2009gl041108

Catania, G. A., Neumann, T. A., & Price, S. F. (2008). Characterizing englacial drainage in the ablation zone of the Greenland ice sheet. *Journal of Glaciology, 54*(187), 567-578. doi:10.3189/002214308786570854

Catania, G. A., Stearns, L. A., Sutherland, D. A., Fried, M. J., Bartholomaus, T. C., Morlighem, M., … Nash, J. (2018). Geometric Controls on Tidewater Glacier Retreat in Central Western Greenland. *Journal of Geophysical Research: Earth Surface, 123*(8), 2024-2038. doi:10.1029/2017jf004499

Chandler, D. M., Wadham, J. L., Lis, G. P., Cowton, T., Sole, A., Bartholomew, I., . . . Hubbard, A. (2013). Evolution of the subglacial drainage system beneath the Greenland Ice Sheet revealed by tracers. *Nature Geoscience, 6*(3), 195-198. doi:10.1038/ngeo1737

Chen, C., Howat, I. M., & Peña, S. D. (2017). Formation and development of supraglacial lakes in the percolation zone of the Greenland ice sheet. *Journal of Glaciology, 63*(241), 847-853. doi:10.1017/jog.2017.50

Christoffersen, P., Bougamont, M., Hubbard, A., Doyle, S. H., Grigsby, S., & Pettersson, R. (2018). Cascading lake drainage on the Greenland Ice Sheet triggered by tensile shock and fracture. *Nature Communications, 9*(1). doi:10.1038/s41467-018-03420-8

Christoffersen, P., Oleary, M., Angelen, J. H. V., & Broeke, M. V. D. (2012). Partitioning effects from ocean and atmosphere on the calving stability of Kangerdlugssuaq Glacier, East Greenland. Annals of Glaciology, 53(60), 249–256. doi: 10.3189/2012aog60a087

Chu, V. W. (2013). Greenland ice sheet hydrology. Progress in Physical Geography: Earth and Environment, 38(1), 19–54. doi: 10.1177/0309133313507075

Chu, V. W., Smith, L. C., Rennermalm, A. K., Forster, R. R., Box, J. E., & Reeh, N. (2009). Sediment plume response to surface melting and supraglacial lake drainages on the Greenland ice sheet. *Journal of Glaciology, 55*(194), 1072-1082. doi:10.3189/002214309790794904

Chudley, T. R., Christoffersen, P., Doyle, S. H., Bougamont, M., Schoonman, C. M., Hubbard, B., & James, M. R. (2019). Supraglacial lake drainage at a fast-flowing Greenlandic outlet glacier. *Proceedings of the National Academy of Sciences, 116*(51), 25468-25477. doi:10.1073/pnas.1913685116

Ciciarelli, J. A. (1991). Some Fundamentals of Photogrammetry. *A Practical Guide to Aerial Photography with an Introduction to Surveying*, 54–76. doi: 10.1007/978-1-4684-6503-7_4

Clason, C. C., Mair, D. W., Nienow, P. W., Bartholomew, I. D., Sole, A., Palmer, S., & Schwanghart, W. (2015). Modelling the transfer of supraglacial meltwater to the bed of Leverett Glacier, Southwest Greenland. *The Cryosphere*, *9*(1), 123-138. doi:10.5194/tc-9-123-2015

Cook, S. J., Christoffersen, P., Todd, J., Slater, D., & Chauché, N. (2020). Coupled modelling of subglacial hydrology and calving-front melting at Store Glacier, West Greenland. *The Cryosphere, 14*(3), 905-924. doi:10.5194/tc-14-905-2020

Cooley, S. W., & Christoffersen, P. (2017). Observation Bias Correction Reveals More Rapidly Draining Lakes on the Greenland Ice Sheet. *Journal of Geophysical Research: Earth Surface, 122*(10), 1867-1881. doi:10.1002/2017jf004255

Cottier, F. R., Nilsen, F., Skogseth, R., Tverberg, V., Skarðhamar, J., & Svendsen, H. (2010). Arctic fjords: A review of the oceanographic environment and dominant physical processes. *Geological Society, London, Special Publications, 344*(1), 35-50. doi:10.1144/sp344.4

Cowton, T., Slater, D., Sole, A., Goldberg, D., & Nienow, P. (2015). Modeling the impact of glacial runoff on fjord circulation and submarine melt rate using a new subgrid-scale parameterization for glacial plumes. *Journal of Geophysical Research: Oceans, 120*(2), 796-812. doi:10.1002/2014jc010324

Cuffey, K. M., & Paterson, W. S. B. (2011). The physics of glaciers. Boston,: Elsevier.

Danielson, B., & Sharp, M. (2013). Development and application of a time-lapse photograph analysis method to investigate the link between tidewater glacier flow variations and supraglacial lake drainage events. *Journal of Glaciology*, *59*(214), 287–302. doi: 10.3189/2013jog12j108

Darlington, E.F. (2015). Meltwater delivery from the tidewater glacier Kronebreen to Kongsfjorden, Svalbard; insights from in-situ and remote-sensing analyses of sediment plumes. Thesis, Loughborough University.

Das, S. B., Joughin, I., Behn, M. D., Howat, I. M., King, M. A., Lizarralde, D., & Bhatia, M. P. (2008). Fracture Propagation to the Base of the Greenland Ice Sheet During Supraglacial Lake Drainage. *Science, 320*(5877), 778-781. doi:10.1126/science.1153360

de Fleurian, B., Morlighem, M., Seroussi, H., Rignot, E., Broeke, M. R., Munneke, P. K., . . . Tedstone, A. J. (2016). A modeling study of the effect of runoff variability on the effective pressure beneath Russell Glacier, West Greenland. *Journal of Geophysical Research: Earth Surface, 121*(10), 1834-1848. doi:10.1002/2016jf003842

Dietrich, R., Maas, H., Baessler, M., Rülke, A., Richter, A., Schwalbe, E., & Westfeld, P. (2007). Jakobshavn Isbræ, West Greenland: Flow velocities and tidal interaction of the front area from 2004 field observations. *Journal of Geophysical Research, 112*(F3). doi:10.1029/2006jf000601

Doyle, S. H., Hubbard, B., Christoffersen, P., Young, T. J., Hofstede, C., Bougamont, M. H., Box, J. E., and Hubbard, A. (2018). Physical conditions of fast glacier flow: measurements from boreholes drilled to the bed of Store Glacier in West Greenland, J. Geophys. Res.-Earth, 123, 324–348, https://doi.org/10.17863/CAM.17485.

Doyle, S. H., Hubbard, A. L., Dow, C. F., Jones, G. A., Fitzpatrick, A., Gusmeroli, A., . . . Box, J. E. (2013). Ice tectonic deformation during the rapid in situ drainage of a supraglacial lake on the Greenland Ice Sheet. *The Cryosphere, 7*(1), 129-140. doi:10.5194/tc-7-129-2013

Doyle, S. H., Hubbard, A., Fitzpatrick, A. A., As, D. V., Mikkelsen, A. B., Pettersson, R., & Hubbard, B. (2014). Persistent flow acceleration within the interior of the Greenland ice sheet. *Geophysical Research Letters, 41*(3), 899-905. doi:10.1002/2013gl058933

Dow, C. F., Kulessa, B., Rutt, I. C., Tsai, V. C., Pimentel, S., Doyle, S. H., . . . Hubbard, A. (2015). Modeling of subglacial hydrological development following rapid supraglacial lake drainage. *Journal of Geophysical Research: Earth Surface, 120*(6), 1127-1147. doi:10.1002/2014jf003333

Dowdeswell, J. A., & Benham, T. J. (2003). A surge of Perseibreen, Svalbard, examined using aerial photography and ASTER high resolution satellite imagery. *Polar Research*, *22*(2), 373–383. doi: 10.3402/polar.v22i2.6466

Easa, S. M. (2010). Space resection in photogrammetry using collinearity condition without linearisation. *Survey Review*, *42*(315), 40–49. doi: 10.1179/003962609x451681

Fettweis, X., Box, J. E., Agosta, C., Amory, C., Kittel, C., Lang, C., … Gallée, H. (2017). Reconstructions of the 1900–2015 Greenland ice sheet surface mass balance using the regional climate MAR model. The Cryosphere, 11(2), 1015–1033. doi: 10.5194/tc-11-1015-2017

Finsterwalder, R. (1954). Photogrammetry and Glacier Research with Special Reference to Glacier Retreat in the Eastern Alps. *Journal of Glaciology*, *2*(15), 306–315. doi: 10.1017/s0022143000025119

Fitzpatrick, A. A., Hubbard, A. L., Box, J. E., Quincey, D. J., As, D. V., Mikkelsen, A. P., . . . Jones, G. A. (2014). A decade (2002–2012) of supraglacial lake volume estimates across Russell Glacier, West Greenland. *The Cryosphere*, *8*(1), 107-121. doi:10.5194/tc-8-107-2014

Flowers, G. E. (2015). Modelling water flow under glaciers and ice sheets. *Proceedings of the Royal Society A: Mathematical, Physical and Engineering Sciences*, *471*(2176), 20140907. doi:10.1098/rspa.2014.0907

Fox, A. J., & Nuttall, A. M. (1997). Photogrammetry as A Research Tool for Glaciology. *The Photogrammetric Record*, *15*(89), 725–737. doi: 10.1111/0031-868x.00081

Fried, M.J., Catania, G.A., Bartholomaus, T.C., Duncan, D., Davis, M., Stearns, L.A., Nash, J., Shroyer, E. and Sutherland, D. (2015). Distributed subglacial discharge drives significant submarine melt at a Greenland tidewater glacier. Geophysical Research Letters, 42, 2015GL065806.

Gagliardini, O., Zwinger, T., Gillet-Chaulet, F., Durand, G., Favier, L., de Fleurian, B., Greve, R., Malinen, M., Martín, C., Råback, P., Ruokolainen, J., Sacchettini, M., Schäfer, M., Seddik, H., and Thies, J. (2013). Capabilities and performance of Elmer/Ice, a newgeneration ice sheet model, Geosci. Model Dev., 6, 1299–1318, https://doi.org/10.5194/gmd-6-1299-2013.

Georgiou, S., Shepherd, A., Mcmillan, M., & Nienow, P. (2009). Seasonal evolution of supraglacial lake volume from ASTER imagery. *Annals of Glaciology, 50*(52), 95-100. doi:10.3189/172756409789624328

Gledhill, L. A., & Williamson, A. G. (2017). Inland advance of supraglacial lakes in north-west Greenland under recent climatic warming. *Annals of Glaciology, 59*(76pt1), 66-82. doi:10.1017/aog.2017.31

Granshaw, S. I. (2019). Laussedat bicentenary: origins of photogrammetry. *The Photogrammetric Record, 34*(166), 128–147. doi: 10.1111/phor.12277

Hartley, R. I. and Zisserman, A. (2004). Multiple View Geometry in Computer Vision, 2nd edn. Cambridge University Press, UK, 655 pp.

Hinks, A. R. (1922). Stereographic Survey: The Stereoautograph. *The Geographical Journal, 59*(4), 273. doi: 10.2307/1781512

Hoffman, M. J., Catania, G. A., Neumann, T. A., Andrews, L. C., & Rumrill, J. A. (2011). Links between acceleration, melting, and supraglacial lake drainage of the western Greenland Ice Sheet. *Journal of Geophysical Research, 116*(F4). doi:10.1029/2010jf001934

Hoffman, M. J., Perego, M., Andrews, L. C., Price, S. F., Neumann, T. A., Johnson, J. V., . . . Lüthi, M. P. (2018). Widespread Moulin Formation During Supraglacial Lake Drainages in Greenland. *Geophysical Research Letters, 45*(2), 778-788. doi:10.1002/2017gl075659

Hofstede, C., Christoffersen, P., Hubbard, B., Doyle, S. H., Young, T. J., Diez, A., … Hubbard, A. (2018). Physical Conditions of Fast Glacier Flow: 2. Variable Extent of Anisotropic Ice and Soft Basal Sediment From Seismic Reflection Data Acquired on Store Glacier, West Greenland. *Journal of Geophysical Research: Earth Surface*, *123*(2), 349–362. doi: 10.1002/2017jf004297

How, P. (2018). Dynamical change at tidewater glaciers examined using time-lapse photogrammetry, PhD thesis, University of Edinburgh, Edinburgh, UK.

How, P., Hulton, N. R. J., & Buie, L. (2018). PyTrx: A Python toolbox for deriving velocities, surface areas and line measurements from oblique imagery in glacial environments. *Geoscientific Instrumentation, Methods and Data Systems Discussions*, 1–26. doi: 10.5194/gi-2018-28

Howat, I. M., Box, J. E., Ahn, Y., Herrington, A., & Mcfadden, E. M. (2010). Seasonal variability in the dynamics of marine-terminating outlet glaciers in Greenland. *Journal of Glaciology, 56*(198), 601-613. doi:10.3189/002214310793146232

Ignéczi, Á, Sole, A. J., Livingstone, S. J., Leeson, A. A., Fettweis, X., Selmes, N., . . . Briggs, K. (2016). Northeast sector of the Greenland Ice Sheet to undergo the greatest inland expansion of supraglacial lakes during the 21st century. *Geophysical Research Letters, 43*(18), 9729-9738. doi:10.1002/2016gl070338

James, M. R., How, P., & Wynn, P. M. (2016). Pointcatcher software: analysis of glacial time-lapse photography and integration with multitemporal digital elevation models. *Journal of Glaciology, 62*(231), 159–169. doi: 10.1017/jog.2016.27

James, T. D., Murray, T., Selmes, N., Scharrer, K., & O'Leary, M. (2014). Buoyant flexure and basal crevassing in dynamic mass loss at Helheim Glacier. *Nature Geoscience, 7*(8), 593–596. doi: 10.1038/ngeo2204

Jenkins, A. (2011). Convection-Driven Melting near the Grounding Lines of Ice Shelves and Tidewater Glaciers. Journal of Physical Oceanography, 41(12), 2279–2294. doi: 10.1175/jpo-d-11-03.1

Jennings, S. J. A., Hambrey, M. J., Glasser, N. F., James, T. D., & Hubbard, B. (2015). Structural glaciology of Austre Brøggerbreen, northwest Svalbard. *Journal of Maps, 12*(5), 790–796. doi: 10.1080/17445647.2015.1076744

Joughin, I., Das, S. B., Flowers, G. E., Behn, M. D., Alley, R. B., King, M. A., . . . Angelen, J. H. (2013). Influence of ice-sheet geometry and supraglacial lakes on seasonal ice-flow variability. *The Cryosphere, 7*(4), 1185-1192. doi:10.5194/tc-7-1185-2013

Joughin, I., Das, S. B., King, M. A., Smith, B. E., Howat, I. M., & Moon, T. (2008). Seasonal Speedup Along the Western Flank of the Greenland Ice Sheet. *Science, 320*(5877), 781-783. doi:10.1126/science.1153288

Joughin, I., Smith, B. E., & Howat, I. M. (2017). A complete map of Greenland ice velocity derived from satellite data collected over 20 years. *Journal of Glaciology, 64*(243), 1-11. doi:10.1017/jog.2017.73

Jouvet, G., Weidmann, Y., Kneib, M., Detert, M., Seguinot, J., Sakakibara, D., & Sugiyama, S. (2018). Short-lived ice speed-up and plume water flow captured by a VTOL UAV give insights into subglacial hydrological system of Bowdoin Glacier, Remote Sens. Environ., 217, 389–399, https://doi.org/10.1016/j.rse.2018.08.027.

Khan, S. A., Aschwanden, A., Bjørk, A. A., Wahr, J., Kjeldsen, K. K., & Kjær, K. H. (2015). Greenland ice sheet mass balance: a review. Reports on Progress in Physics, 78(4), 046801. doi: 10.1088/0034-4885/78/4/046801

Koziol, C. P., & Arnold, N. (2018). Modelling seasonal meltwater forcing of the velocity of land-terminating margins of the Greenland Ice Sheet. *The Cryosphere, 12*(3), 971-991. doi:10.5194/tc-12-971-2018

Koziol, C., Arnold, N., Pope, A., & Colgan, W. (2017). Quantifying supraglacial meltwater pathways in the Paakitsoq region, West Greenland. *Journal of Glaciology, 63*(239), 464-476. doi:10.1017/jog.2017.5

Krawczynski, M. J., Behn, M. D., Das, S. B., & Joughin, I. (2009). Constraints on the lake volume required for hydro-fracture through ice sheets. *Geophysical Research Letters, 36*(10). doi:10.1029/2008gl036765

Kristensen, L., & Benn, D. (2012). A surge of the glaciers Skobreen–Paulabreen, Svalbard, observed by time-lapse photographs and remote sensing data. *Polar Research, 31*(1), 11106. doi:10.3402/polar.v31i0.11106

Kääb, A. (2010). Aerial photogrammetry in glacier studies. In Pellikka, P., and Rees, W. G. eds. Remote sensing of glaciers: techniques for topographic, spatial and thematic mapping of glaciers. CRC Press/Balkema, Leiden, 115–136

Lea, J. M. (2018). Google Earth Engine Digitisation Tool (GEEDiT), and Margin change Quantification Tool (MaQiT) – simple tools for the rapid mapping and quantification of changing Earth surface margins., Earth Surface Dynamics

Leeson, A. A., Shepherd, A., Briggs, K., Howat, I., Fettweis, X., Morlighem, M., & Rignot, E. (2015). Supraglacial lakes on the Greenland ice sheet advance inland under warming climate. *Nature Climate Change, 5*(1), 51-55. doi:10.1038/nclimate2463

Legleiter, C. J., Tedesco, M., Smith, L. C., Behar, A. E., & Overstreet, B. T. (2014). Mapping the bathymetry of supraglacial lakes and streams on the Greenland ice sheet using field measurements and high-resolution satellite images. *The Cryosphere, 8*(1), 215-228. doi:10.5194/tc-8-215-2014

Liang, Y., Colgan, W., Lv, Q., Steffen, K., Abdalati, W., Stroeve, J., . . . Bayou, N. (2012). A decadal investigation of supraglacial lakes in West Greenland using a fully automatic detection and tracking algorithm. *Remote Sensing of Environment, 123*, 127-138. doi:10.1016/j.rse.2012.03.020

Luckman, A., Benn, D. I., Cottier, F., Bevan, S., Nilsen, F., & Inall, M. (2015). Calving rates at tidewater glaciers vary strongly with ocean temperature. *Nat Commun, 6*(8566). doi:10.1038/ncomms9566

Lüthi, M. P., Ryser, C., Andrews, L. C., Catania, G. A., Funk, M., Hawley, R. L., . . . Neumann, T. A. (2015). Heat sources within the Greenland Ice Sheet: Dissipation, temperate paleo-firn and cryo-hydrologic warming. *The Cryosphere, 9*(1), 245-253. doi:10.5194/tc-9-245-2015

Macdonald, G. J., Banwell, A. F., & Macayeal, D. R. (2018). Seasonal evolution of supraglacial lakes on a floating ice tongue, Petermann Glacier, Greenland. *Annals of Glaciology, 59*(76pt1), 56-65. doi:10.1017/aog.2018.9

Mallalieu, J., Carrivick, J. L., Quincey, D. J., Smith, M. W., & James, W. H. (2017). An integrated Structure-from-Motion and time-lapse technique for quantifying ice-margin dynamics. *Journal of Glaciology, 63*(242), 937–949. doi: 10.1017/jog.2017.48

Matlab. (2017). Computer Vision System Toolbox: User's Guide.

Matthews, J. B., & A. V. Quinlan. (1975). Seasonal characteristics of water masses in Muir Inlet, a fjord with tidewater glaciers. J. Fish. Res. Board Can., 32, 1693–1703, doi:https://doi.org/10.1139/f75-203.

McFeeters, S. K. (1996). The use of the Normalized Difference Water Index (NDWI) in the delineation of open water features, International Journal of Remote Sensing, 17:7, 1425-1432, doi: 10.1080/01431169608948714

McMillan, M., Nienow, P., Shepherd, A., Benham, T., & Sole, A. (2007). Seasonal evolution of supra-glacial lakes on the Greenland Ice Sheet. *Earth and Planetary Science Letters, 262*(3-4), 484-492. doi:10.1016/j.epsl.2007.08.002

Meierbachtol, T., Harper, J., & Humphrey, N. (2013). Basal Drainage System Response to Increasing Surface Melt on the Greenland Ice Sheet. *Science, 341*(6147), 777-779. doi:10.1126/science.1235905

Messerli, A. & Grinsted, A. (2015). Image GeoRectification And Feature Tracking toolbox: ImGRAFT. Geoscientific Instrumentation Methods and Data Systems 4(1), 23–34, doi:10.5194/gi-4-232015.

Miles, K. E., Willis, I. C., Benedek, C. L., Williamson, A. G., & Tedesco, M. (2017). Toward Monitoring Surface and Subsurface Lakes on the Greenland Ice Sheet Using Sentinel-1 SAR and Landsat-8 OLI Imagery. *Frontiers in Earth Science, 5*. doi:10.3389/feart.2017.00058

Moon, T., Joughin, I., Smith, B., Broeke, M. R., Berg, W. J., Noël, B., & Usher, M. (2014). Distinct patterns of seasonal Greenland glacier velocity. *Geophysical Research Letters, 41*(20), 7209-7216. doi:10.1002/2014gl061836

Mordvintsev, A. & Abid, K. (2017). OpenCV-Python Tutorials Documentation

Morriss, B. F., Hawley, R. L., Chipman, J. W., Andrews, L. C., Catania, G. A., Hoffman, M. J., . . . Neumann, T. A. (2013). A ten-year record of supraglacial lake evolution and rapid drainage in West Greenland using an automated processing algorithm for multispectral imagery. *The Cryosphere, 7*(6), 1869-1877. doi:10.5194/tc-7-1869-2013

Motyka, R. J., Hunter, L., Echelmeyer, K. A., & Connor, C. (2003). Submarine melting at the terminus of a temperate tidewater glacier, LeConte Glacier, Alaska, U.S.A. Annals of Glaciology, 36, 57–65. doi: 10.3189/172756403781816374

Mouginot, J., Rignot, E., Bjørk, A. A., Broeke, M. V. D., Millan, R., Morlighem, M., … Wood, M. (2019). Forty-six years of Greenland Ice Sheet mass balance from 1972 to 2018. Proceedings of the National Academy of Sciences, 201904242. doi: 10.1073/pnas.1904242116

Moussavi, M. S., Abdalati, W., Pope, A., Scambos, T., Tedesco, M., Macferrin, M., & Grigsby, S. (2016). Derivation and validation of supraglacial lake volumes on the Greenland Ice Sheet from high-resolution satellite imagery. *Remote Sensing of Environment, 183*, 294-303. doi:10.1016/j.rse.2016.05.024

Moyer, A. N., Nienow, P. W., Gourmelen, N., Sole, A. J., & Slater, D. A. (2017). Estimating Spring Terminus Submarine Melt Rates at a Greenlandic Tidewater Glacier Using Satellite Imagery. *Frontiers in Earth Science, 5*. doi:10.3389/feart.2017.00107

Nienow, P. W., Sole, A. J., Slater, D. A., & Cowton, T. R. (2017). Recent Advances in Our Understanding of the Role of Meltwater in the Greenland Ice Sheet System. *Current Climate Change Reports, 3*(4), 330-344. doi:10.1007/s40641-017-0083-9

Pętlicki, M., Ciepły, M., Jania, J. A., Promińska, A., & Kinnard, C. (2015). Calving of a tidewater glacier driven by melting at the waterline. *Journal of Glaciology, 61*(229), 851–863. doi: 10.3189/2015jog15j062

Phillips, T., Rajaram, H., & Steffen, K. (2010). Cryo-hydrologic warming: A potential mechanism for rapid thermal response of ice sheets. *Geophysical Research Letters, 37*(20). doi:10.1029/2010gl044397

Poinar, K., Joughin, I., Lenaerts, J. T., & Broeke, M. R. (2017). Englacial latent-heat transfer has limited influence on seaward ice flux in western Greenland. *Journal of Glaciology, 63*(237), 1-16. doi:10.1017/jog.2016.103

Pope, A., Scambos, T. A., Moussavi, M., Tedesco, M., Willis, M., Shean, D., & Grigsby, S. (2016). Estimating supraglacial lake depth in West Greenland using Landsat 8 and comparison with other multispectral methods. *The Cryosphere, 10*(1), 15-27. doi:10.5194/tc-10-15-2016

Porter, Claire; Morin, Paul; Howat, Ian; Noh, Myoung-Jon; Bates, Brian; Peterman, Kenneth; Keesey, Scott; Schlenk, Matthew; Gardiner, Judith; Tomko, Karen; Willis, Michael; Kelleher, Cole; Cloutier, Michael; Husby, Eric; Foga, Steven; Nakamura, Hitomi; Platson, Melisa; Wethington, Michael, Jr.; Williamson, Cathleen; Bauer, Gregory; Enos, Jeremy; Arnold, Galen; Kramer, William; Becker, Peter; Doshi, Abhijit; D'Souza, Cristelle; Cummens, Pat; Laurier, Fabien; Bojesen, Mikkel. (2018). "ArcticDEM", https://doi.org/10.7910/DVN/OHHUKH, Harvard Dataverse, V1, [Accessed 2020-01-13].

Reinhardt, W., & Rentsch, H. (1986). Determination of Changes in Volume and Elevation of Glaciers using Digital Elevation Models for the Vernagtferner, Ôtztal Alps, Austria. *Annals of Glaciology, 8,* 151–155. doi: 10.1017/s0260305500001348

Rignot, E., Fenty, I., Xu, Y., Cai, C., & Kemp, C. (2015). Undercutting of marine-terminating glaciers in West Greenland. *Geophysical Research Letters, 42*(14), 5909-5917. doi:10.1002/2015gl064236

Rignot, E., & Kanagaratnam, P. (2006). Changes in the Velocity Structure of the Greenland Ice Sheet. Science, 311(5763), 986–990. doi: 10.1126/science.1121381

Rignot, E., Velicogna, I., Broeke, M. R. V. D., Monaghan, A., & Lenaerts, J. T. M. (2011). Acceleration of the contribution of the Greenland and Antarctic ice sheets to sea level rise. Geophysical Research Letters, 38(5). doi: 10.1029/2011gl046583

Rosenau, R., Schwalbe, E., Maas, H., Baessler, M., & Dietrich, R. (2013). Grounding line migration and high-resolution calving dynamics of Jakobshavn Isbrae, West Greenland. *Journal of Geophysical Research: Earth Surface, 118*(2), 382-395. doi:10.1029/2012jf002515

Saephan, S. (2018). 3d DEM Visualization in QGIS 3.0. https://opengislab.com/blog/2018/3/20/3d-dem-visualization-in-qgis-30.

Schenk., T. (2005). Introduction to Photogrammetry. *Department of Civil and Environmental Engineering and Geodetic Science,* The Ohio State University, Columbus (OH).

Schild, K.M., Hawley, R.L. and Morriss, B.F. (2016). Subglacial hydrology at Rink Isbræ, West Greenland inferred from sediment plume appearance. Annals of Glaciology, 57, 118–127.

Selmes, N., Murray, T., & James, T. D. (2011). Fast draining lakes on the Greenland Ice Sheet. *Geophysical Research Letters, 38*(15). doi:10.1029/2011gl047872

Shepherd, A., Hubbard, A., Nienow, P., King, M., Mcmillan, M., & Joughin, I. (2009). Greenland ice sheet motion coupled with daily melting in late summer. *Geophysical Research Letters, 36*(1). doi:10.1029/2008gl035758

Slater, D. A., Nienow, P. W., Cowton, T. R., Goldberg, D. N., & Sole, A. J. (2015). Effect of near-terminus subglacial hydrology on tidewater glacier submarine melt rates. Geophysical Research Letters, 42(8), 2861–2868. doi: 10.1002/2014gl062494

Slater, D., Nienow, P., Sole, A., Cowton, T., Mottram, R., Langen, P., & Mair, D. (2017). Spatially distributed runoff at the grounding line of a large Greenlandic tidewater glacier inferred from plume modelling. *Journal of Glaciology, 63*(238), 309-323. doi:10.1017/jog.2016.139

Slater, D. A., Straneo, F., Das, S. B., Richards, C. G., Wagner, T. J., & Nienow, P. W. (2018). Localized Plumes Drive Front-Wide Ocean Melting of A Greenlandic Tidewater Glacier. *Geophysical Research Letters, 45*(22). doi:10.1029/2018gl080763

Sneed, W. A., & Hamilton, G. S. (2007). Evolution of melt pond volume on the surface of the Greenland Ice Sheet. *Geophysical Research Letters, 34*(3). doi:10.1029/2006gl028697

Sole, A., Nienow, P., Bartholomew, I., Mair, D., Cowton, T., Tedstone, A., & King, M. A. (2013). Winter motion mediates dynamic response of the Greenland Ice Sheet to warmer summers. *Geophysical Research Letters, 40*(15), 3940-3944. doi:10.1002/grl.50764

Solem, J. E. (2012). *Programming Computer Vision with Python: Tools and Algorithms for Analyzing Images*. O'Reilly Media, Sebastopol, CA, 1st edn.

Stevens, L. A., Behn, M. D., Mcguire, J. J., Das, S. B., Joughin, I., Herring, T., . . . King, M. A. (2015). Erratum: Corrigendum: Greenland supraglacial lake drainages triggered by hydrologically induced basal slip. *Nature, 525*(7567), 144-144. doi:10.1038/nature14608

Stevens, L.A., Straneo, F., Das, S.B., Plueddemann, A.J., Kukulya, A.L. and Morlighem, M. (2016). Linking glacially modified waters to catchment-scale subglacial discharge using autonomous underwater vehicle observations. The Cryosphere, 10, 417–432.

Straneo, F., & Cenedese, C. (2015). The Dynamics of Greenland's Glacial Fjords and Their Role in Climate. *Annual Review of Marine Science, 7*(1), 89-112. doi:10.1146/annurev-marine-010213-135133

Sugiyama, S., Bauder, A., Huss, M., Riesen, P., & Funk, M. (2009). Correction to “Triggering and drainage mechanisms of the 2004 glacier-dammed lake outburst in Gornergletscher, Switzerland”. *Journal of Geophysical Research, 114*(F1). doi:10.1029/2009jf001275

Sundal, A., Shepherd, A., Nienow, P., Hanna, E., Palmer, S., & Huybrechts, P. (2009). Evolution of supra-glacial lakes across the Greenland Ice Sheet. *Remote Sensing of Environment, 113*(10), 2164-2171. doi:10.1016/j.rse.2009.05.018

Sundal, A. V., Shepherd, A., Nienow, P., Hanna, E., Palmer, S., & Huybrechts, P. (2011). Melt-induced speed-up of Greenland ice sheet offset by efficient subglacial drainage. *Nature, 469*(7331), 521-524. doi:10.1038/nature09740

Svendsen, H., Beszczynska-Møller, A., Hagen, J. O., Lefauconnier, B., Tverberg, V., Gerland, S., . . Wiencke, C. (2002). The physical environment of Kongsfjorden–Krossfjorden, an Arctic fjord system in Svalbard. *Polar Research, 21*(1), 133-166. doi:10.3402/polar.v21i1.6479

Tedesco, M., Willis, I. C., Hoffman, M. J., Banwell, A. F., Alexander, P., & Arnold, N. S. (2013). Ice dynamic response to two modes of surface lake drainage on the Greenland ice sheet. *Environmental Research Letters, 8*(3), 034007. doi:10.1088/1748-9326/8/3/034007

Tedstone, A. J., Nienow, P. W., Gourmelen, N., Dehecq, A., Goldberg, D., & Hanna, E. (2015). Decadal slowdown of a land-terminating sector of the Greenland Ice Sheet despite warming. *Nature, 526*(7575), 692-695. doi:10.1038/nature15722

Todd, J., Christoffersen, P., Zwinger, T., Råback, P., Chauché, N., Benn, D., . . . Hubbard, A. (2018). A Full-Stokes 3-D Calving Model Applied to a Large Greenlandic Glacier. *Journal of Geophysical Research: Earth Surface, 123*(3), 410-432. doi:10.1002/2017jf004349

van den Broeke, M. R. V. D., Enderlin, E. M., Howat, I. M., Munneke, P. K., Noël, B. P. Y., Berg, W. J. V. D., … Wouters, B. (2016). On the recent contribution of the Greenland ice sheet to sea level change. The Cryosphere, 10(5), 1933–1946. doi: 10.5194/tc-10-1933-2016

Vargo, L. J., Anderson, B. M., Horgan, H. J., Mackintosh, A. N., Lorrey, A. M., & Thornton, M. (2017). Using structure from motion photogrammetry to measure past glacier changes from historic aerial photographs. *Journal of Glaciology*, *63*(242), 1105–1118. doi: 10.1017/jog.2017.79

Verhoeven, G., Wieser, M., Briese, C., & Doneus, M. (2013). Positioning in time and space – cost-effective exterior orientation for airborne archaeological photographs. *ISPRS Annals of Photogrammetry, Remote Sensing and Spatial Information Sciences, II-5/W1,* 313-318. doi:10.5194/isprsannals-ii-5-w1-313-2013

Walford, A. (2017). What is photogrammetry? Retrieved from: http://www.photogrammetry.com/index.htm (Accessed: 2020-01-04)

Whitehead, K., Moorman, B., & Wainstein, P. (2014). Measuring daily surface elevation and velocity variations across a polythermal arctic glacier using ground-based photogrammetry. *Journal of Glaciology*, *60*(224), 1208–1220. doi: 10.3189/2014jog14j080

Williamson, A. G., Arnold, N. S., Banwell, A. F., & Willis, I. C. (2017). A Fully Automated Supraglacial lake area and volume Tracking ("FAST") algorithm: Development and application using MODIS imagery of West Greenland. *Remote Sensing of Environment, 196*, 113-133. doi:10.1016/j.rse.2017.04.032

Williamson, A. G., Banwell, A. F., Willis, I. C., & Arnold, N. S. (2018a). Dual-satellite (Sentinel-2 and Landsat 8) remote sensing of supraglacial lakes in Greenland. *The Cryosphere, 12*(9), 3045-3065. doi:10.5194/tc-12-3045-2018

Williamson, A. G., Willis, I., Arnold, N., & Banwell, A. (2018b). Controls on rapid supraglacial lake drainage in West Greenland: An Exploratory Data Analysis approach. *Journal of Glaciology*, *64*(244), 208-226. doi:10.1017/jog.2018.8

Xu, Y., Rignot, E., Menemenlis, D., & Koppes, M. (2012). Numerical experiments on subaqueous melting of Greenland tidewater glaciers in response to ocean warming and enhanced subglacial discharge. Annals of Glaciology, 53(60), 229–234. doi: 10.3189/2012aog60a139

Young, T. J., Christoffersen, P., Doyle, S. H., Nicholls, K. W., Stewart, C. L., Hubbard, B., . . . Bougamont, M. (2019). Physical Conditions of Fast Glacier Flow: 3. Seasonally-Evolving Ice Deformation on Store Glacier, West Greenland. *Journal of Geophysical Research: Earth Surface*, *124*(1), 245-267. doi:10.1029/2018jf004821

Zwally, H. J., Abdalati, W., Herring, T., Larson, K., Saba, J., & Steffen, K. (2002). Surface melt-induced acceleration of Greenland ice-sheet flow, Science, 297(5579), 218–222, doi:10.1126/science.1072708

Appendix A

Time series of the individual estimated lake volume for all 54 lakes. Y-axis show volume in $10^5\,m^3$.

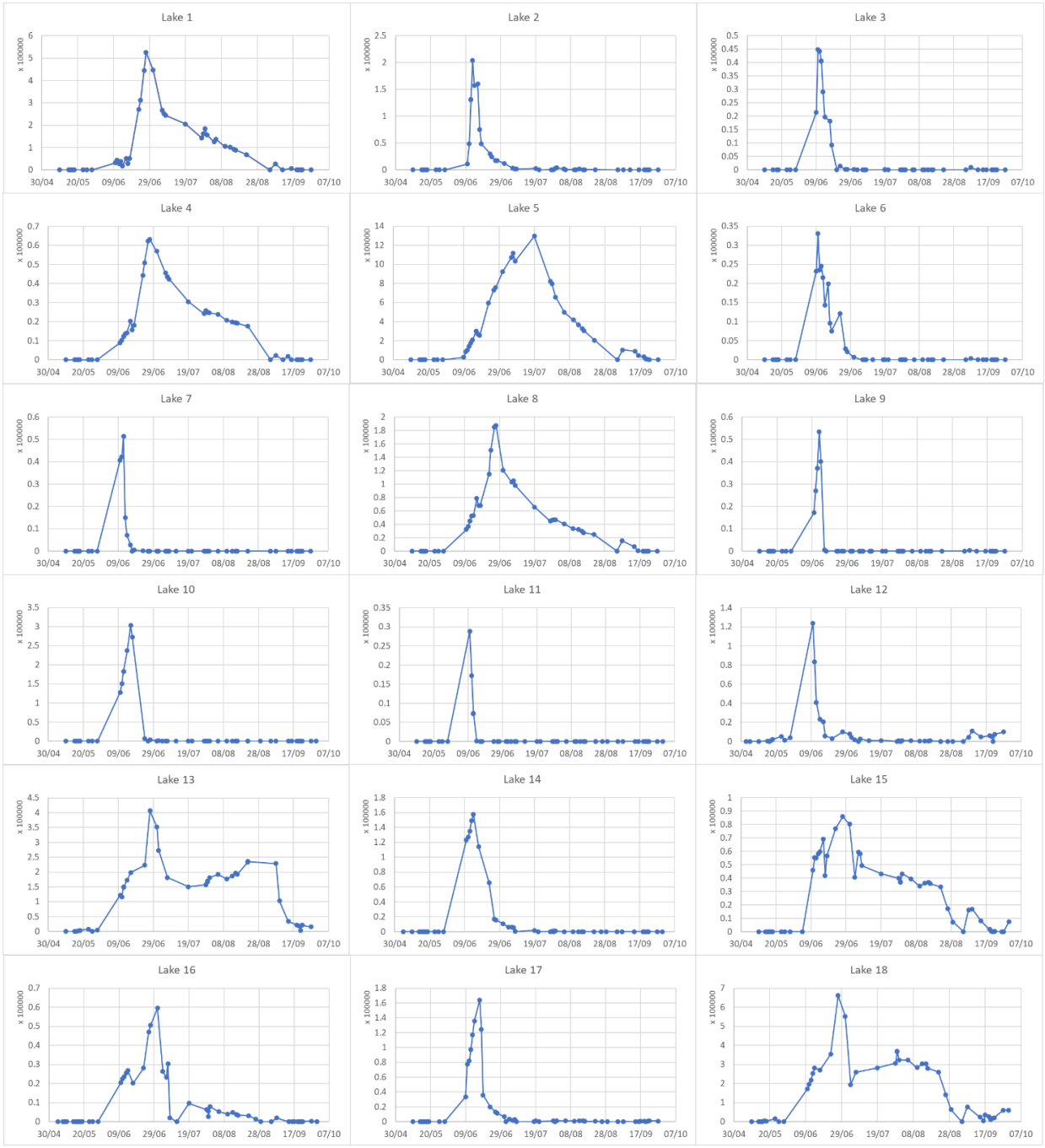

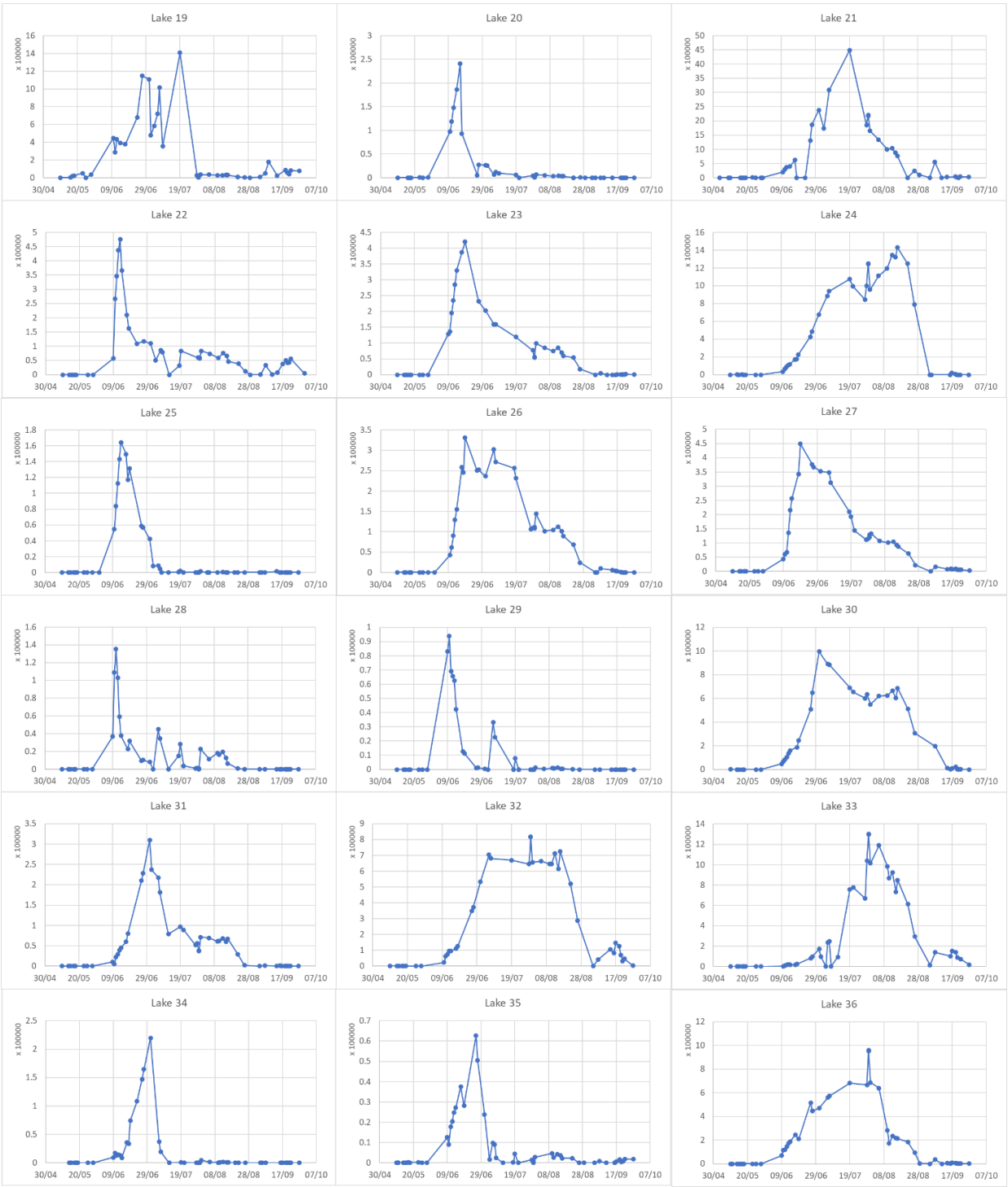
Lake 19
Lake 20
Lake 21
Lake 22
Lake 23
Lake 24
Lake 25
Lake 26
Lake 27
Lake 28
Lake 29
Lake 30
Lake 31
Lake 32
Lake 33
Lake 34
Lake 35
Lake 36
x 100000
30/04 20/05 09/06 29/06 19/07 08/08 28/08 17/09 07/10

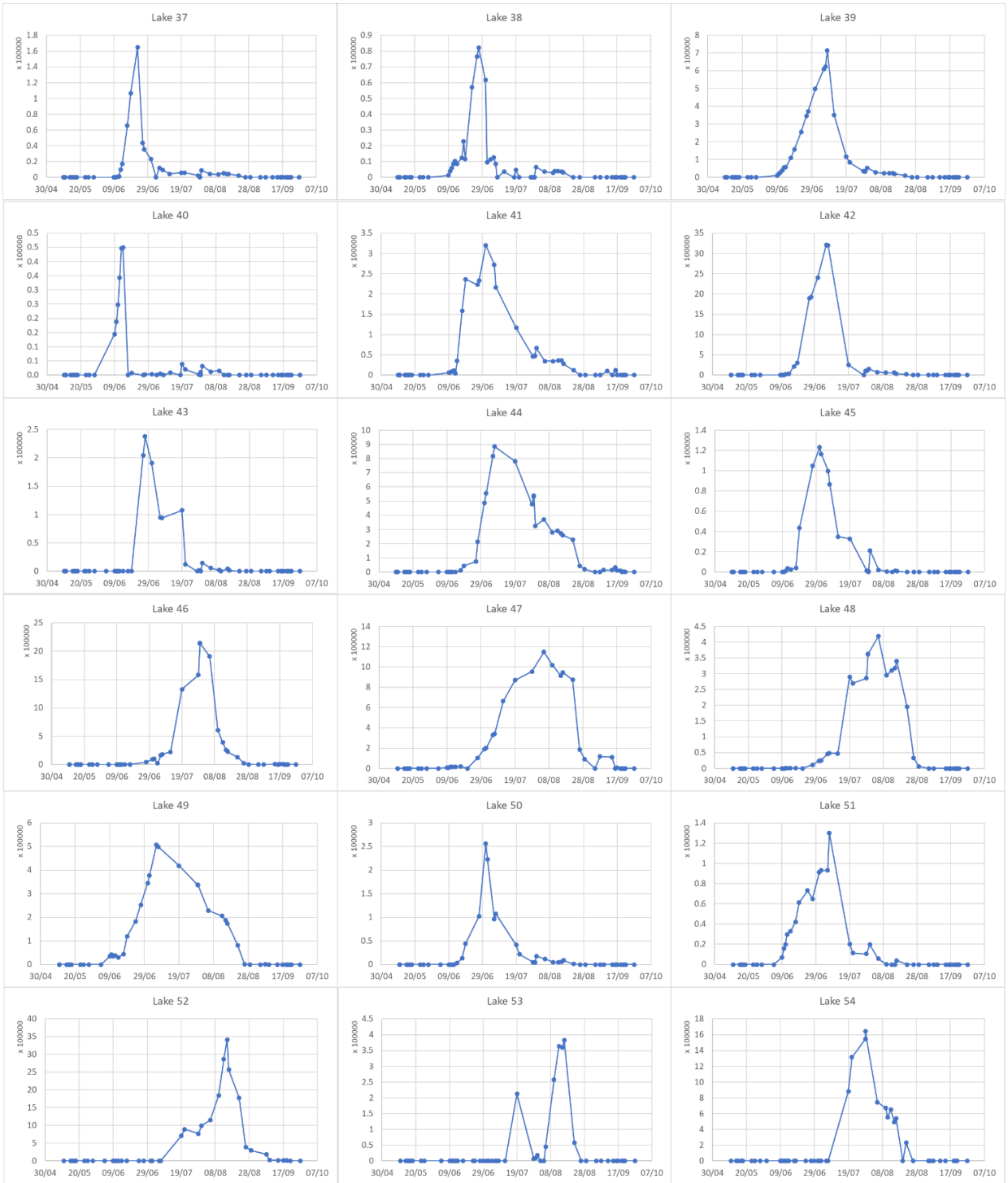
Lake 37
Lake 38
Lake 39
Lake 40
Lake 41
Lake 42
Lake 43
Lake 44
Lake 45
Lake 46
Lake 47
Lake 48
Lake 49
Lake 50
Lake 51
Lake 52
Lake 53
Lake 54
x 100000
30/04 20/05 09/06 29/06 19/07 08/08 28/08 17/09 07/10

Appendix B

Python script for interpolating lake volumes:

```
import pandas as pd
df = pd.read_excel('Lakes.xlsx')
#Print the dataframe
df
cdf = df.interpolate(method ='linear', limit_direction ='forward')
dcdf = cdf.interpolate(method ='linear', limit_direction ='backward')
dcdf.to_excel(r'C:\Users\isabe\My_Scripts\Examples\interpolLakes.xlsx')
```